DIELECTRIC WAVEGUIDES

FOR

MILLIMETER WAVES

Thesis by

Edgard Schweig

In Partial Fulfillment of the Requirements

for the Degree of

Doctor of Philosophy

California Institute of Technology

Pasadena, California

1982

(Submitted May 25, 1982)

ACKNOWLEDGEMENTS

ABSTRACT

In this thesis, we analyze high-permittivity dielectric waveguides for use as guiding structures of millimeter waves. Two basic geometries are considered: the circular and rectangular guides.

In Part I, we describe the theory of round fibers surrounded by an infinite cladding. Millimeter wavelengths are comparable to the physical dimensions of the guide. Therefore, a large difference in permittivity between the core and the cladding is required in order to provide for a tight confinement of the fields. We present the results of computations of the propagation characteristics and losses of fibers of very high permittivity. We note that the distribution of the electromagnetic power between the core and the cladding can be deduced from the dispersion curves. Finally, we consider the feasibility of a dielectric fiber made of thallium bromide-iodide (KRS-5) for the long distance transmission of W-band signals (94 GHz). Using our measurements of the dielectric parameters of KRS-5, we find that the losses are several orders of magnitude higher than the losses of conventional metallic waveguides.

In Part II, we analyze rectangular dielectric guides made of high-permittivity materials such as GaAs that would permit the fabrication of active devices directly into the transmission line. We present a new numerical technique base on finite-differences for computing the modes of dielectric guiding structures. This method is simple and efficient

in computer storage and computational time. We use it to compute the modes of a rectangular dielectric waveguide and compare the numerical results to those obtained from Marcatili's closed-form solution. We find that this latter one is a good approximation for the dominant mode of a rectangular guide even when the permittivity of the guide is large compared to the outer medium. For higher order modes, Marcatili's solution predicts incorrect propagation curves. We have also observed the presence in our numerical solution of "spurious modes" that are thought to be due to the mathematical indefinitiveness of the problem.

In Part III, we present a waveguide technique for the measurement of complex dielectric constants at millimiter wave frequencies: the shorted-waveguide method. Waveguide methods have been extensively used at lower frequencies but this is the first application at 94 GHZ. We use a novel sample preparation technique that allows for an accurate and gap-free positionment of a ductile dielectric material inside a metallic waveguide. We note that the correct choice of sample lengths is critical to the accuracy of the measurement of the loss tangent. Finally, we summarize the results of our measurement of the dielectric constant and loss tangent of thallium bromide-iodide (KRS-5) and thallium bromide-chloride (KRS-6).

Parts of this thesis have been or will be published under the following titles:

Part II: "Computer Analysis of Dielectric Waveguides for Millimeter Waves", Edgard Schweig and William B. Bridges, (to be submitted: IEEE Trans. MTT).

"Computer Analysis of Rectangular Dielectric Waveguides for Millimeter Waves", Edgard Schweig and William B. Bridges, IEEE International Conference on Infrared and Millimeter Waves, Miami, December 1982.

Part III: "Measurement of the Dielectric Constant and Loss Tangent of Thallium Mixed Halide Crystals KRS-5 and KRS-6 at 95 GHz", William B. Bridges, Marvin B. Klein and Edgard Schweig, IEEE Trans. Microwave Th. Tech., Vol. MTT-30, March 1982, pp. 286-292.

CONTENTS

Part I.   Round Dielectric Fibers

1.   Introduction

Hondros and Debye [1] and, more recently, Elsasser [2] and Chandler [3] have studied a dielectric rod as a structure capable of supporting a "surface wave" that is, an electromagnetic wave which is bound to the surface of the structure: The fields are characterized by an exponential decay away from the surface and a propagation function exp $(-j\beta z)$. These studies have shown some of the peculiar features of the "surface wave" modes that differ from the modes existing in conventional metallic waveguides:

   a)   the existence of a guided mode with no low-frequency

        cutoff;

   b)   a finite spectrum of discrete guided modes together

        with a continuous spectrum of radiation modes;

   c)   the possibility of modes that propagate with a phase

        velocity less than that of light.

Since the late 1960's, optical waveguides, mostly in the form of glass fibers, have been studied extensively for their applications in optical communication systems (see, for example, the review paper by Gloge, Ref. 4). Such optical waveguides consist of a core surrounded by a cladding with an index of refraction that is somewhat lower than the index of the core (see Fig. 1). The difference in index is, in practice, of the order of only a few parts in a thousand [*], which leads

---

[*] Hence, the adjective "weakly-guiding" commonly used to describe such optical fibers.

to important simplifications in the equations determining the modes that can propagate. The results can be summarized in the form of curves that are independent of the actual difference in refractive index as long as it is a small quantity. Typical fiber core diameters are about 10 μm which is much larger than the wavelength of the light that propagates on the fiber ($\lambda_o \lesssim 1$ μm).

In contrast, millimeter-wavelengths are comparable to the physical dimensions of the guiding structures, and it is thus necessary to provide for a tighter confinement of the fields within the guide ("strongly-guiding fiber"). This is achieved by using materials that present a large difference of refractive index between the core and the cladding. In such a guide, it is necessary to compute the exact solutions to Maxwell's equations for each configuration. Relatively little work has appeared in the recent literature on such strongly-guiding structures, compared to the vast literature on weakly-guiding optical fibers.

We will describe in the next sections the theory of circular fibers and the results of some computations of the propagation characteristics and losses of fibers of very high refractive index. [*]
We will also compare these results with the approximations employed for the study of weakly-guiding fibers.

---

[*] We will often quote results from the excellent book by H.-G. Unger on "Planar Optical Waveguides and Fibers" that presents a detailed and complete analysis of dielectric guides.
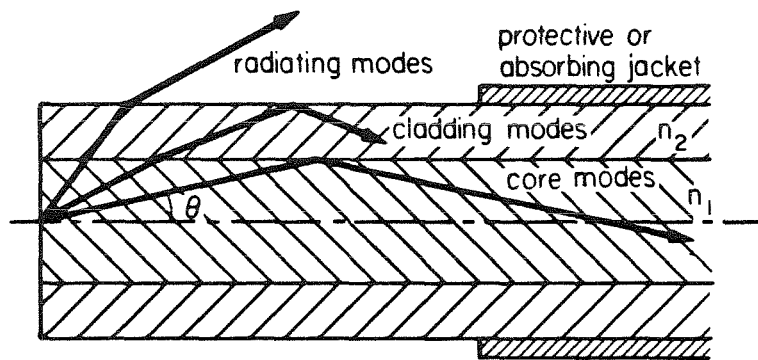
Figure 1. Cladded-core fiber. A ray-optics picture permits to visualize the various types of modes.

2. Guided Modes for Unlimited Cladding

2.1. Assumptions

The fibers which we would use for signal transmission are designed in such a way that the fiber modes are guided by the core: the fields and their energy are well confined inside or near the core. The evanescent fields near the outer cladding boundary should be so small that the external jacket will not affect the core modes. Therefore, we need, in practice, to extend the cladding to a large enough diameter for the intensity of the evanescent fields to decay to a very low value (compatible with the losses that can be tolerated in the fiber).

In our theoretical model, we will let the cladding region extend to infinity. This will not change any of the dominant mode characteristics, except for the very small attenuation due to jacket absorption. Also, we will assume that all media are isotropic, homogeneous and lossless. The losses will be introduced afterwards as a perturbation.

2.2. Field Solutions

The fiber has a core of index n_1 and radius a and is surrounded by an infinite cladding of index n_2 (Fig. 2). We will consider a time-harmonic solution of frequency ω and a cylindrical system of coordinates (r, ϕ, z) with the z-axis along the fiber axis. We adopt the longitudinal components, E_z and H_z, as the generating components of the electromagnetic fields (see Appendix A).
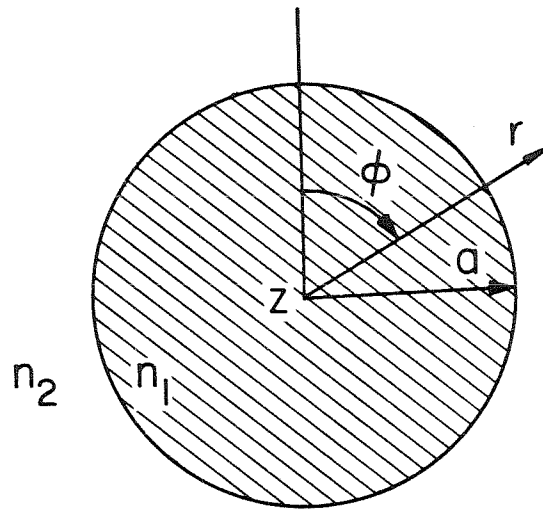
Figure 2. Cross section of a round fiber with infinite cladding.
A cylindrical system of coordinates is used in the field analysis.

For a wave propagating in the z-direction, the common z-dependence must be:

$$\exp\ (-j\beta z) \qquad .$$

The longitudinal fields must therefore satisfy the following transverse wave equation:

$$(\nabla_t^2 + k_{r_q}^2) \begin{Bmatrix} E_z \\ H_z \end{Bmatrix} = 0 \qquad , \qquad (1)$$

where ∇_t^2 is the transverse Laplacian operator

$$\nabla_t^2 = \frac{1}{r} \frac{\partial}{\partial r} (r\ \frac{\partial}{\partial r}) + \frac{1}{r^2} \frac{\partial^2}{\partial \phi^2} \qquad . \qquad (2)$$

The separation constant k_{r_q} depends on the region considered, i.e.,

$$k_{r_q}^2 = n_q^2\ k_o^2 - \beta^2 \qquad \text{for } q = 1,2 \qquad , \qquad (3)$$

where k_o is the free-space wavenumber. The transversal field distribution can be written as *

in region 1:

$$E_{z_1} = A_E\ J_m(k_{r_1} r)\ \cos m\phi \qquad\qquad (5.a)$$

$$H_{z_1} = A_H\ J_m(k_{r_1} r)\ \sin m\phi \qquad \text{for } r \leq a, \qquad (5.b)$$

---

* The factor $\exp\ [j(\omega t - \beta z)]$ is omitted in all the field components.

and in region 2:

$$E_{z_2} = B_E K_m(jk_{r_2} r) \sin m\phi \qquad (6.a)$$

$$H_{z_2} = B_H K_m(jk_{r_2} r) \cos m\phi \text{ for } r > a. \qquad (6.b)$$

The choice of radial functional dependence given in Eqs. 5 and 6 assures, for a core mode, the proper behavior of the fields.

The tangential components of the fields $\vec{E}$ and $\vec{H}$ must be matched at the interface r=a. The matching conditions specify a system of four linear homogeneous equations for the four undetermined quantities A_E- B_H. The compatibility condition of the system is the characteristic equation that yields the values of β corresponding to modes of propagation.

The various modes are designated E_{on}, H_{on}, HE_{mn}, EH_{mn}. The first capital letter shows the dominant field component; the second letter (if any) indicates that the mode is hybrid, i.e., that it has both longitudinal electric and magnetic fields. The subscripts correspond to the order of the mode: m for the angular variation and n for the radial variation.

To describe the solutions, we will use the following abbreviations that are common in the description of optical fibers (see, for example, Ref. 5). We define a radial phase parameter in the core, u, and a radial attenuation parameter in the cladding, v:

$$u = k_{r1}a = a\sqrt{k_o^2 n_1^2 - \beta^2} \quad , \tag{7}$$

$$v = jk_{r2}a = a\sqrt{\beta^2 - k_o^2 n_2^2} \quad . \tag{8}$$

These quantities are real and positive for propagating modes. We also define a normalized frequency, V, (also called fiber parameter):

$$V = k_o a \sqrt{n_1^2 - n_2^2} \quad , \tag{9}$$

and a normalized phase parameter, B:

$$B = \frac{(\beta/k_o)^2 - n_2^2}{n_1^2 - n_2^2} \quad . \tag{10}$$

This last parameter is very useful in the description of dispersion characteristics as it is normalized to the range [0,1].

The effective index [*] for the mode in consideration is given by

$$N = \beta/k_o \quad . \tag{11}$$

Finally, we will use the following combinations of Bessel functions:

$$Y_m = \frac{J_m'(u)}{u\, J_m(u)} \tag{12}$$

and

$$X_m = \frac{K_m'(v)}{v\, K_m(v)} \quad . \tag{13}$$

---

[*]   This is the refractive index of an infinite medium in which a plane wave would propagate with the same phase velocity.

The characteristic equation then reduces to [1,5]

$$(Y_m + X_m)(n_1^2 Y_m + n_2^2 X_m) = \frac{m^2 N^2}{(u^2 B)^2} \qquad (14)$$

The mathematical properties of Eq. 14 allow us to deduce some of the properties of the modes without actually solving it.

Let us consider first the case of the axially symmetric modes: $m = 0$. These modes are either transverse magnetic or transverse electric. The characteristic equation splits into:

$$Y_o + X_o = 0 \qquad \text{for the H-modes} \quad ,$$

$$n_1^2 Y_o + n_2^2 X_o = 0 \qquad \text{for the E-modes} \quad .$$

When $m \neq 0$ the fields have an angular dependence; the characteristic equation can be thought of as a quadratic equation in terms of Y_m and rewritten as,

$$Y_m = -\frac{1+(n_2/n_1)^2}{2} X_m \mp \left(\left(\frac{1-(n_2/n_1)^2}{2} X_m\right)^2 + \frac{m^2 N^2}{n_1^2 (u^2 B)^2}\right)^{1/2} \qquad (17)$$

The upper sign corresponds to the HE-modes while the lower corresponds to the EH-modes. The HE_{11} and EH_{11} modes are the lowest hybrid ones. The HE_{11}-modes resembles, inside the core, the H_{11}-mode of a round metallic guide in the field distribution. Unlike the HE_{11}-metallic pipe mode, this particular solution to Eq. 17 has a zero cutoff[*] and

_____

* This result can be obtained from the asymptotic behavior of Eq. 17 for small values of u and v.

therefore constitutes the fundamental fiber mode. The next modes to go above cutoff, as V is increased, are the axially-symmetric H_{01} and E_{01} modes: They have a cutoff at $V = 2.405$. At very low frequency $(V \lesssim 2.405)$, the behavior of the HE_{11}-mode can be approximated by[5]

$$B = \frac{1.26}{V^2} \exp \left\{ -[1+n_1^2/n_2^2)]/V^2 \right\} \quad . \qquad (18)$$

The limiting forms of the characteristic equations are summarized in Table I. We note that for all modes with m=0 and m=1, the HE_{11} excepted, the cutoff frequency is a particular root of the Bessel function $J_m(u)$, where m corresponds to the circumferential order. The cutoff frequency is then independent of the index ratio n_1/n_2.

Far from cutoff, i.e., for large values of V, all modes have a behavior of the form [5]

$$u \simeq u_\infty [1 - \frac{1+(n_2/n_1)^2}{2V}] \quad , \qquad (19)$$

where u_∞ is a Bessel root, as indicated in Table I.

2.3 Power Distribution

An important consideration in the design of a clad dielectric fiber is the distribution of power between the core and the cladding. The fraction of power that flows in the core will determine, to first approximation (see Section 5), the attenuation due to dielectric losses.

TABLE 1

Limiting forms of the characteristic equation for the radial phase parameter u (from Ref. 5).

Circumferential order	HE_{mp}-modes at cut-off	$(E_{0p}$ for $m = 0)$ far above	EH_{mp}-modes at cut-off	$(H_{0p}$ for $m = 0)$ far above
$m = 0$	$J_0(u) = 0$	$J_1(u) = 0$	$J_0(u) = 0$	$J_1(u) = 0$
1	$J_1(u) = 0$	$J_0(u) = 0$	$J_1(u) = 0$ (excluding $u=0$)	$J_2(u) = 0$
≥ 2	$\dfrac{J_{m-2}(u)}{J_{m-1}(u)} = -\dfrac{n_1^2-n_2^2}{n_1^2+n_2^2}$	$J_{m-1}(u) = 0$	$J_m(u) = 0$	$J_{m+1}(u) = 0$

"Cut-off" and "far above cut-off" correspond to the following limits of the radial attenuation parameter v:

cut-off: v = 0

far above: v → ∞

The radial phase parameter, u, and the radial attenuation parameter, v, are related to the normalized frequency V by: $V^2 = u^2 + v^2$.

If S_z is the axial component of the time-averaged Poynting vector, then the total power traveling along the guide is given by:[*]

$$P_t = \int_\infty S_z \, dx \, dy \quad . \tag{20}$$

The fractions of the total power propagating respectively in the core and in the cladding (assumed to be of infinite extent) are obtained from

$$P_{core} = \int_{core} S_z \, dx \, dy \tag{21a}$$

$$P_{clad} = \int_{clad} S_z \, dx \, dy \quad . \tag{21b}$$

The fractions that we will consider are:

$$\rho_{core} = P_{core}/P_t \tag{22a}$$

and

$$\rho_{clad} = P_{clad}/P_t \tag{22b}$$

with

$$\rho_{core} + \rho_{clad} = 1 \quad .$$

If the waveguide incorporates only isotropic and non-dispersive $(\frac{\partial n}{\partial \lambda} = 0)$ media which may be inhomogeneous in the transverse direction, we can use the following identity [6],

---

[*] $\int_\infty dx \, dy$ indicates an integral over the whole plane (x,y).

$$\frac{c^2}{v_g v_p} = c^2 \frac{d\beta^2}{d\omega^2} = \frac{\int_\infty n^2 S_z \, dx \, dy}{\int_\infty S_z \, dx \, dy} \qquad (23)$$

where v_g and v_p are respectively the group and phase velocities.
Eq. (23) is rigorous and can be derived either by expressing
the Poynting vector $\vec{S}$ in terms of the fields $\vec{E}$ and $\vec{H}$ and integrating
over the cross section [7] or by applying a perturbation $\Delta\omega$ to the wave
equations for $\vec{E}$ and $\vec{H}$.[8] By introducing the normalized parameters
V and B (see Eqs. 9 and 10) in the left-hand side of Eq. (23) we
obtain:

$$c^2 \frac{d\beta}{d\omega} \frac{\beta}{\omega} = \frac{1}{2}(n_1^2 - n_2^2) \left[\frac{d(V\,B)}{d\,V} + B\right] + n_2^2 \quad .$$

For a step-index fiber, the right-hand side simplifies into

$$\frac{\int_\infty n^2 S_z \, dx \, dy}{\int_\infty S_z \, dx \, dy} = n_1^2 \, \rho_{core} + n_2^2 \, \rho_{clad}$$

$$= (n_1^2 - n_2^2) \, \rho_{core} + n_2^2 \quad .$$

Hence, the fraction of power in the core can be obtained very simply
from the propagation characteristic, i.e., the curve B(V),
by using the following relation:

$$\rho_{core} = B + \frac{V}{2} \frac{dB}{dV} \quad . \qquad (24)$$

It is important to note that neither the derivation of this equation nor the use of Eq. (23) require the assumption of a weakly guiding fiber.

3. Numerical Results

A program was written to solve numerically the characteristic equation for a round fiber with an infinite cladding. The results are presented in Figs. 3-5 in terms of the normalized parameters V and B. Fig. 3 corresponds to a Teflon core surrounded by air [*] and Figs. 4 and 5 correspond to a core of KRS-5 surrounded by air and Teflon, respectively.

The sequence of the various modes, that is, the order in which they turn on as the normalized frequency is increased, remains the same in all three cases. But as the index of the core is increased, the phase parameter of the HE_{pq}- and E_{0q}-modes remains very small until a higher value of V is reached. This tendency is lessened when the index of the cladding is increased, i.e., the important factor is the ratio of refractive indices between the core and the cladding. The H_{0q}-modes are independent of the index ratio while the behavior of the EH_{pq}-modes depends less on the index ratio than the HE_{pq}-modes.

For most millimeter-wave applications, the waveguide would be used in a single-mode configuration. It is therefore important to

---

[*] By "air" we refer to a lossless medium of refractive index equal to unity, which is, in practice, a very good approximation to the dielectric parameters of air.
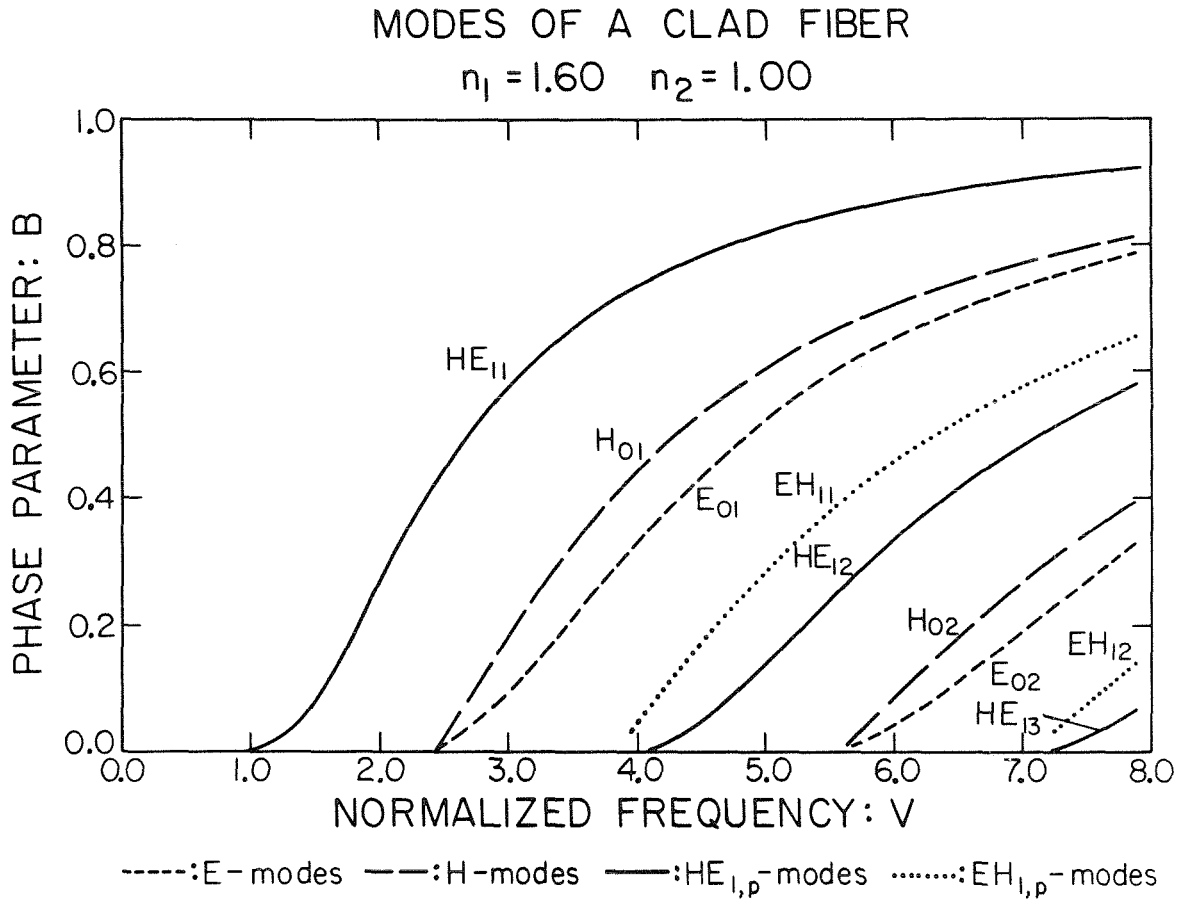
Figure 3. Dispersion curves for the modes of a round fiber with infinite cladding:

core   : n_1 = 1.60   (Teflon)
cladding: n_2 = 1.00   (air).
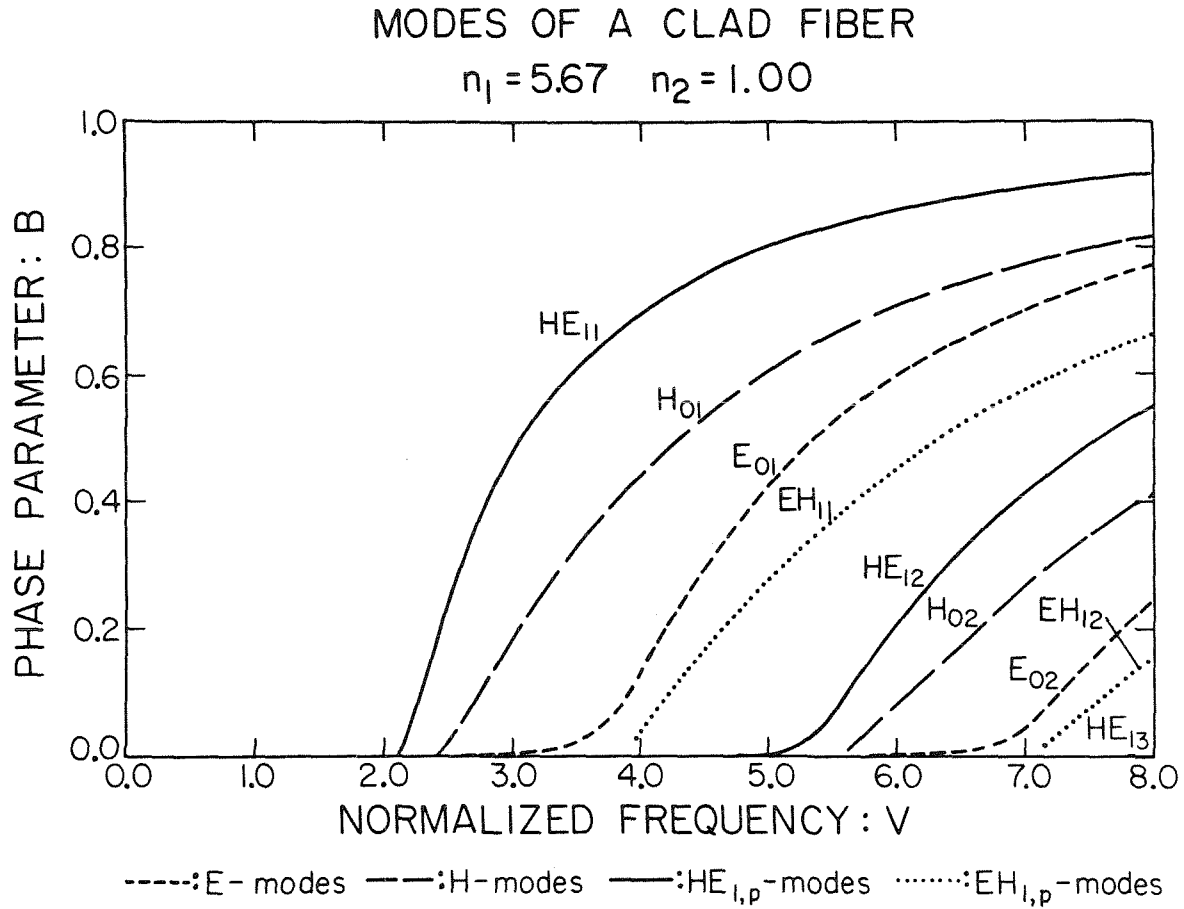
Figure 4. Dispersion curves for the modes of a round fiber with infinite cladding. The higher index core modifies the way the modes go to cutoff. The cutoff frequencies are independent of the index ratio n_1/n_2.

core   : n_1 = 5.67 (KRS-5)

cladding: n_2 = 1.00 (air).

MODES OF A CLAD FIBER
$n_1 = 5.67$ $n_2 = 1.60$
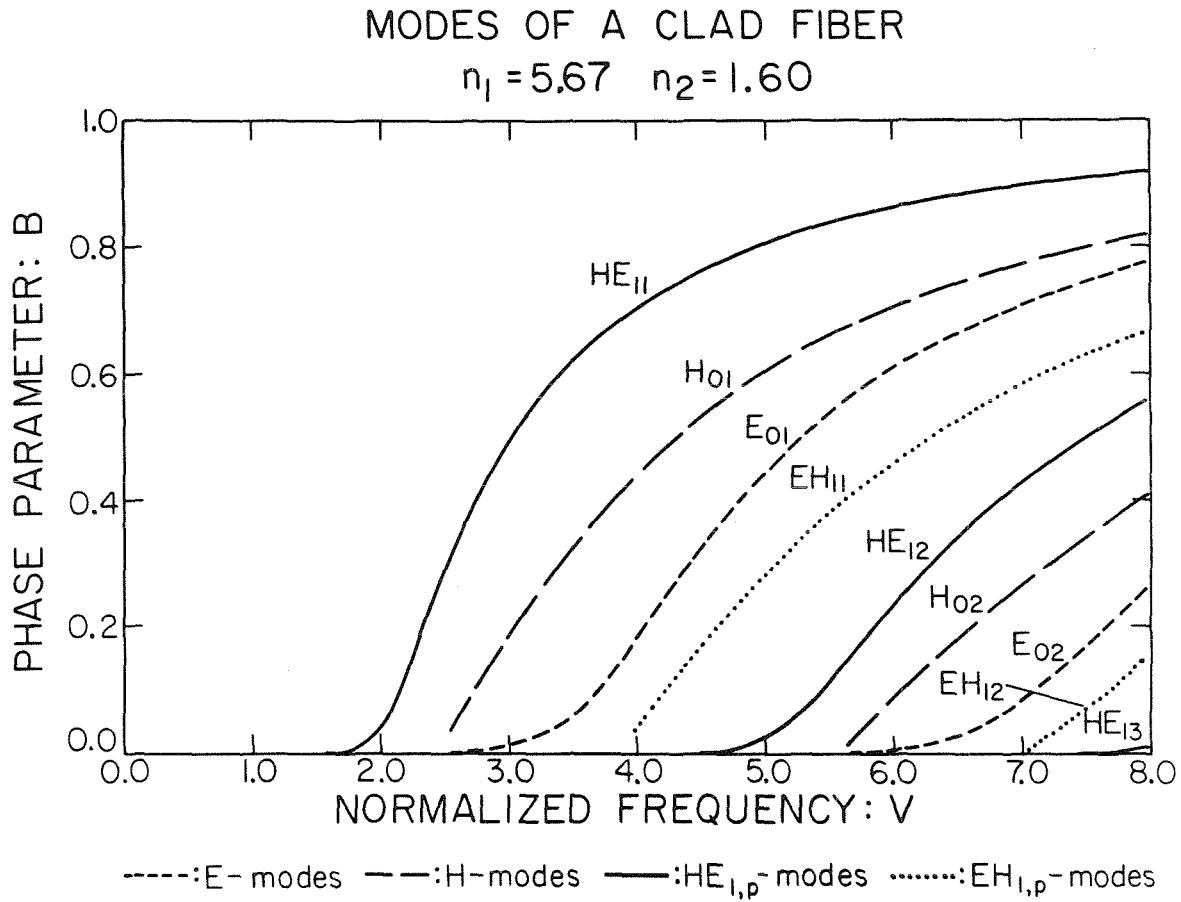
Figure 5. Dispersion curves for the modes of a round fiber with infinite cladding. The presence of a Teflon cladding lowers the index ratio compared to the case illustrated in Fig. 4:

$$core \quad : n_1 = 5.67 \quad (KRS-5)$$
$$cladding: n_2 = 1.60 \quad (Teflon).$$

determine the frequency range over which only the lowest-order HE_{11}-mode can exist. This is similar to the useful frequency range of ordinary metallic "dominant-mode waveguide". However, unlike the dominant mode in a metallic guide, the HE_{11}-mode has no low-frequency cutoff. As the normalized frequency is decreased, more and more of the power will flow outside of the core, resulting in weak guiding or "loose confinement". We will consider the HE_{11}-mode to be strongly guided, or "closely confined", when at least 90% of the power is propagating within the core. This constitutes, of course, an arbitrary definition of the lower frequency limit of the single-mode range of operation. The high-frequency limit will occur when the next mode is turned on, which corresponds to a fixed value of V=2.405, independent of the ratio of refractive indices. Fig. 6-9 show the dispersion characteristic and power distribution in the different core/cladding combinations considered above. If the core has a high refractive index, the HE_{11}-mode will turn on very rapidly, as seen by comparing Figs. 6 and 7. Figs. 8 and 9 show the turn on of this mode on an expanded scale in the case of a high-index core surrounded by claddings of different indices. It can be noted that a reduction of index step between the core and the cladding will slow the rise in the fraction of power carried by the core to the point that for a KRS-5/Teflon fiber, the next mode appears before strong guidance of the HE_{11}-mode is attained (following our definition of strong guidance as ρ_{core} = 90%). Therefore, in practice, it is

POWER DISTRIBUTION IN A CLAD FIBER:

$n_1 = 1.60 \quad n_2 = 1.00$

NORMALIZED FREQUENCY : ka
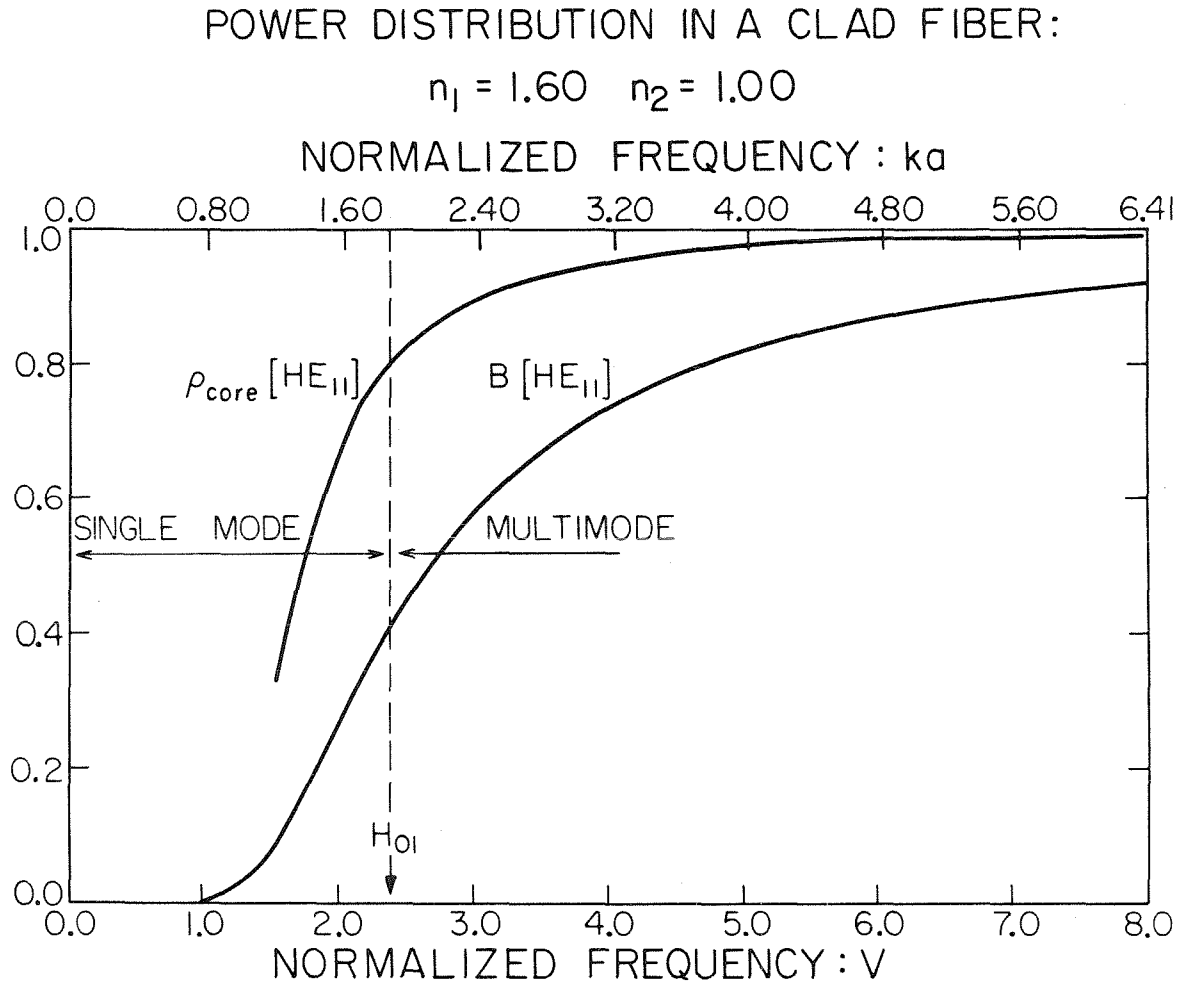
Figure 6. Dispersion characteristic and power distribution of a round
fiber with infinite cladding. A single mode operation is desirable in
most applications.

POWER DISTRIBUTION IN A CLAD FIBER:
$n_1 = 5.67$ $n_2 = 1.00$
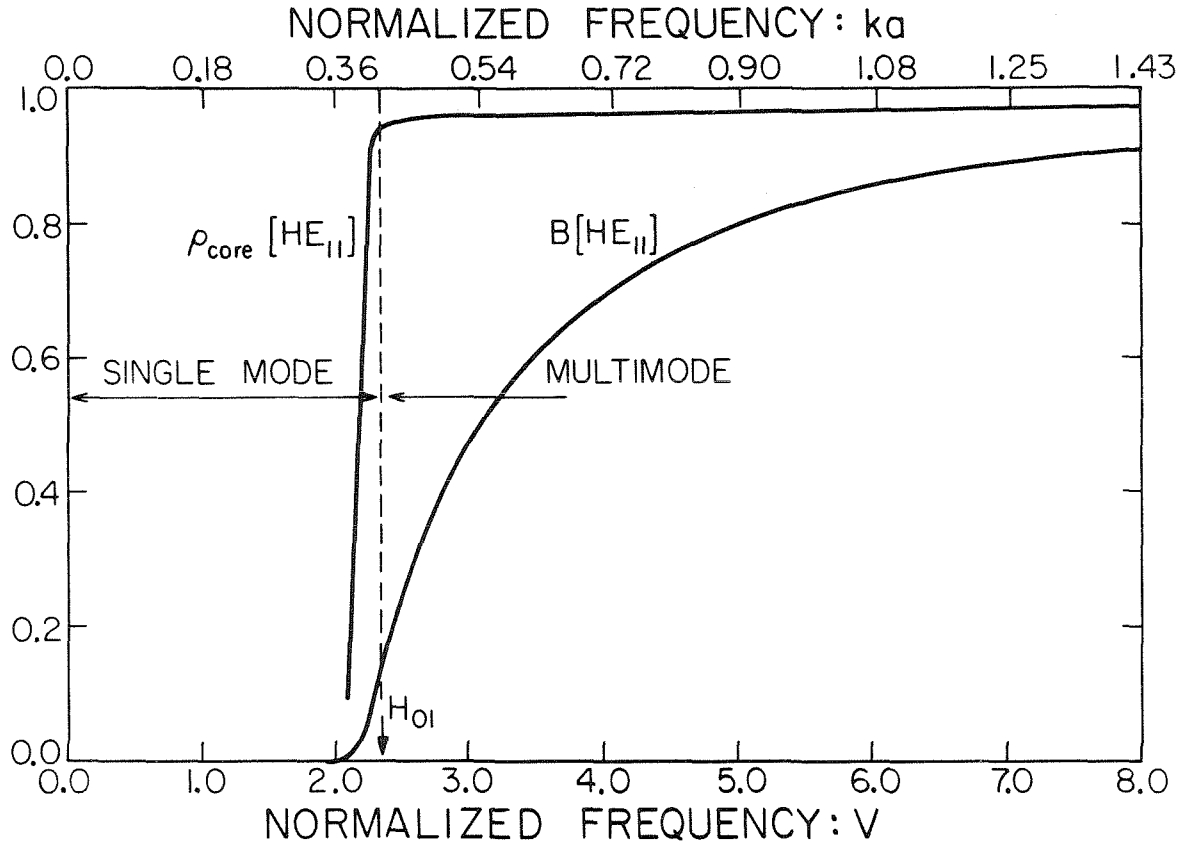
Figure 7. Dispersion characteristics and power distribution of a round fiber with infinite cladding. The high-index core introduces a very sharp rise in the power distribution as the mode is turned on.

POWER DISTRIBUTION IN A CLAD FIBER:
$n_1 = 5.67$ $n_2 = 1.00$
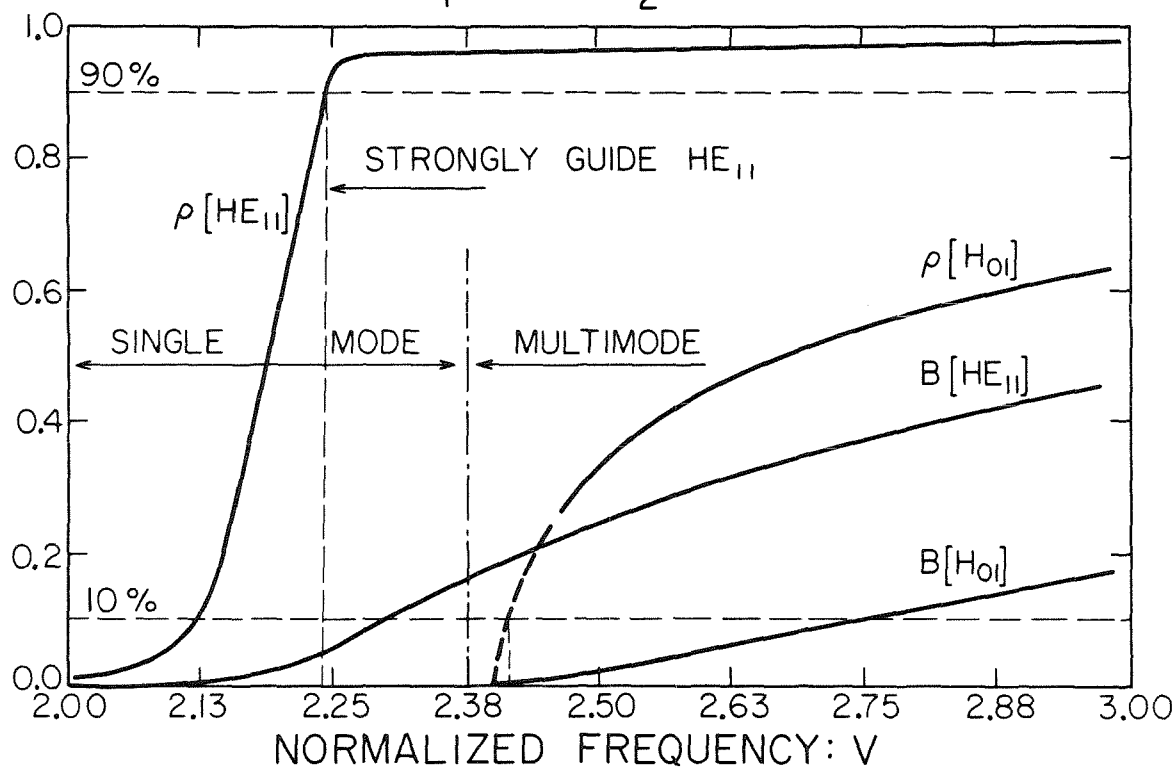
Figure 8. Enlarged view of the turn on of the HE_{11}-mode represented in Figure 7. We have defined the useful operation range as the interval of frequency where the HE_{11}-mode is strongly confined inside the core and the H_{01}-mode is weakly guided or even cut-off.

POWER DISTRIBUTION IN A CLAD FIBER:
$n_1 = 5.67$ $n_2 = 1.60$
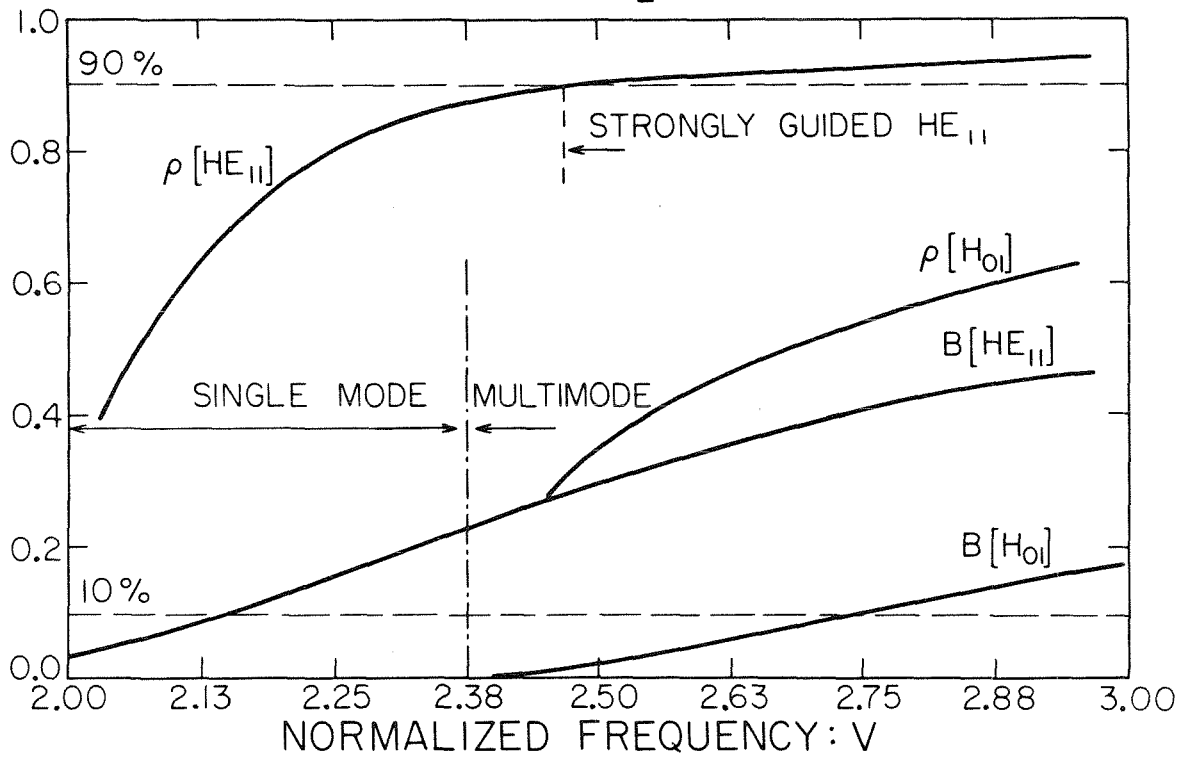
Figure 9. The useful range of operation vanishes when the index ratio is reduced by the introduction of a cladding of larger index.

desirable to clad the fiber with a material of refractive index as close as possible to unity.

The very steep slope of the dominant HE_{11}-dispersion curve in a high-index fiber can be explained by considering Eq. 18, which describes the behavior of this mode for $V \lesssim 1$:

$$B \simeq \frac{1.26}{V^2} \exp\left\{-[1+(n_1/n_2)^2]/V^2\right\} \ . \tag{18}$$

Using Eq. 24, we find that the power distribution is approximately given by

$$\rho_{core} \simeq \frac{1.26}{V^4}[1+(n_1/n_2)^2] \exp\left\{-[1+(n_1/n_2)^2]/V^2\right\} \tag{25a}$$

for the HE_{11}-mode and $V \lesssim 1$; this relation can also be written as:

$$\rho_{core}/B \simeq (1/V^2) \ [1+(n_1/n_2)^2] \ . \tag{25b}$$

Equations (25) indicate that for a large ratio n_1/n_2, ρ_{core} will rise much faster than B, as the mode is turned on. This phenomenon is actually an artifact due to the particular normalization that we chose for the propagation constant.

4. Linearly-Polarized Modes

Consider the cylindrical fiber consisting of a core of index n_1 surrounded by a cladding of index n_2 and infinite extent (Fig. 2). In the case of a weakly-guiding fiber, the refractive indices satisfy

$$\Delta = \frac{(n_1 - n_2)}{n_2} \ll 1 \quad . \tag{26}$$

In this case, we can construct modes whose transverse fields are mostly polarized in one direction: the "linearly-polarized modes"[4,5]. We postulate the following transverse field distribution in the core

$$E_y = H_x \; \frac{\varepsilon_o}{\mu_o} \; \frac{1}{n_1} = E_\ell' \; J_\ell \; (ur/a) \; \cos \ell\phi \tag{27a}$$

and, in the cladding

$$E_y = H_x \; \frac{\varepsilon_o}{\mu_o} \; \frac{1}{n_2} = E_\ell'' \; K_\ell (vr/a) \; \cos \ell\phi \quad , \tag{27b}$$

where u and v are the transverse parameters that were defined previously (Eqs. 7 and 8). The longitudinal components are obtained by using the Maxwell curl equations. One finds that

$$E_z = j \; \frac{Z_o}{k_o} \; (1/n_q)^2 \; \frac{\partial H_x}{\partial y}$$

$$\text{for } q = 1,2 \tag{28}$$

$$H_z = \frac{j}{k_o Z_o} \; \frac{\partial E_y}{\partial x}$$

For small Δ, the longitudinal components become negligible compared to the transverse ones; the factors involved are u/(ka) and v/(ka) which because of the definition of u and v are of order $\Delta^{\frac{1}{2}}$. We will therefore neglect these components when matching the tangential fields at the interface r=a. To first order in Δ, we then obtain the following characteristic equation

$$u \frac{J_{\ell-1}(u)}{J_\ell(u)} = -v \frac{K_{\ell-1}(v)}{K_\ell(v)} \tag{29}$$

for the linearly polarized (LP) modes. These modes can be shown [5] to be particular superpositions of the HE- and EH- fiber modes. For a small index difference, $\Delta \ll 1$, the $HE_{\ell+1,p}$-mode is nearly degenerate with the $EH_{\ell-1,p}$-mode and together, they form the $LP_{\ell p}$-mode. The LP_{0p}-modes represent a special case because they correspond to the HE_{1p}-modes that are already linearly polarized (only when $\Delta \ll 1$).

For the dominant LP_{01}-mode, we can obtain the characteristic equation in closed form, to the same degree of approximation;

$$u(V) = \frac{u_{01}V}{1 + [(u_{01} - 1)^4 + V^4]^{\frac{1}{4}}} \tag{28}$$

where $u_{01} = 2.405$ represents the first zero of the Bessel function $J_0(u)$. To obtain the characteristic equation in the form B(V), we have to use the definition of u, v and V and write

$$B = 1 - (u/V)^2 \quad .$$

The power distribution of this mode is given by

$$\rho_{core} = 1 - (u/V)^2 \left[1 - \frac{K_0(v)}{K_1(v)} \right] \quad . \qquad (29)$$

We have compared, in Fig. 10, the dispersion characteristic for the dominant mode of a round fiber, as obtained by using respectively:

- the LP_{01}-mode closed-form characteristic equation;

- the exact HE_{11}-mode for $n_1 = 1.500$ and $n_2 = 1.000$

- the exact HE_{11}-mode for $n_1 = 5.667$ and $n_2 = 1.000$.

We observe that, as the index of the core is increased to several times the index of the outer medium, the LP_{01}-approximation diverges more and more from the exact solution. The same conclusion is illustrated, in an even more drastic manner, by Fig. 11 that compares the power distributions, ρ_{core}, as computed from the same set of modes.

5. Guided Mode Attenuation

Core and cladding materials were assumed, in what preceded, to be lossless. In reality, guided modes lose power due to material absorption and scattering at inhomogeneities. [*] We will assume that

---

* We will not consider here the problem of geometrical inhomogeneities.
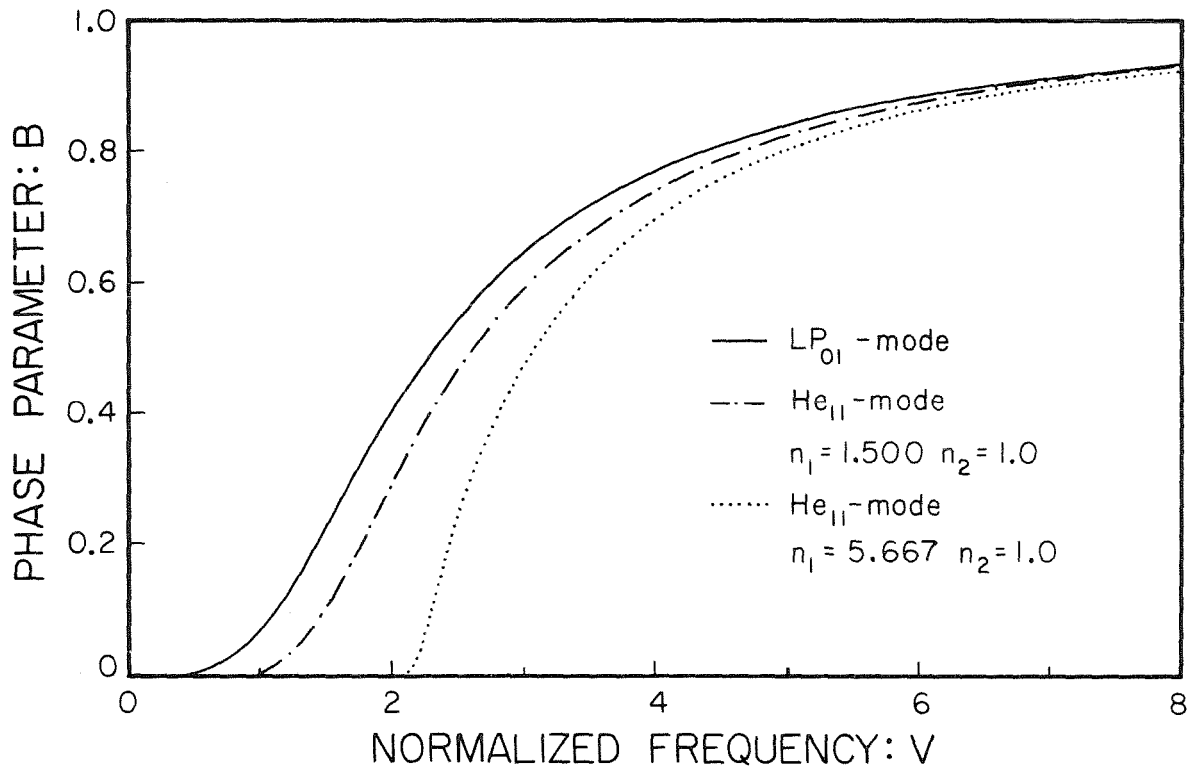
Figure 10. Comparison between the dispersion characteristics of the
dominant fiber mode as computed by using the linearly-polarized mode
approximation and the exact solution for a medium-index core (n_1=1,500)
and a high-index core (n_1=5.667). The LP-approximation diverges at low
frequencies.
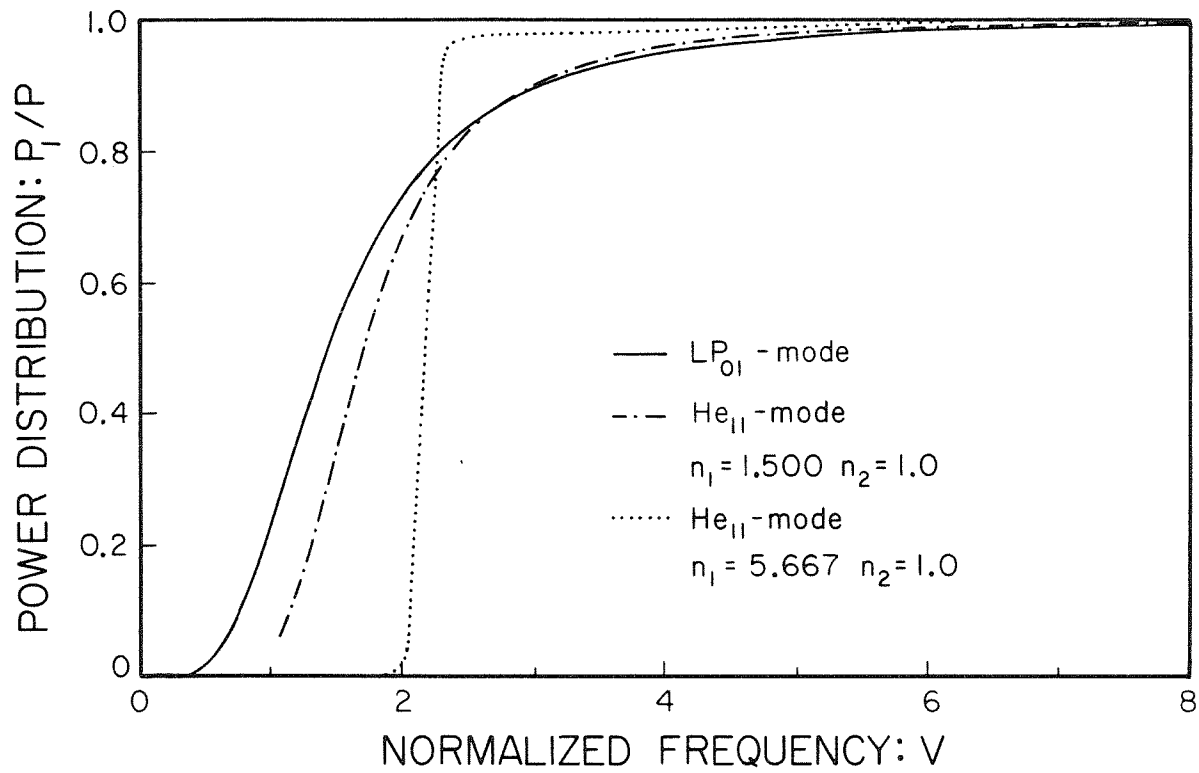
Figure 11. Comparison between the power distribution for the dominant fiber and mode as computed by using the linearly-polarized mode approximation and the exact solution for a medium index core (n_1=1.500) and a high index core (n_1=5.667). The LP-approximation is especially poor for a high index core.

material inhomogeneities occur over a correlation length that is
very much shorter than a wavelength. Under these conditions, Rayleigh's
scattering law applies and the scattering loss can be accounted for
by an imaginary component of the complex refractive index:

$$n_q = n_q' - j \, n_q'' \qquad \text{for } q=1,2 \quad .$$ (20)

The absorption coefficient n_q'' also includes the material absorption.
The guided mode will propagate with a complex propagation constant

$$\gamma = \alpha + j\beta \quad ,$$ (21)

where, for practical low-loss materials,

$$\alpha \ll n_q' \, k_o \quad .$$ (22)

Due to the low absorption and scattering losses, the field distributions
of the guided modes are only slightly perturbed from the lossless case.
The attenuation α can therefore be computed by a perturbation method.
If only the core is lossy[*], we find that, disregarding signs, the
attenuation is given by[2]:

---

[*] Without this assumption the righthand side of Eq. 23 will contain,
in the numerator, an additional term, of the form

$$\int_a^b |E|^2 \, r \, dr$$

where b is the radius of the cladding region,

$$\alpha = \left| \frac{1}{P_t} \frac{dP_t}{dz} \right| = \frac{\sigma \int_0^a |E|^2 \, r \, dr}{\left| \int_0^\infty S_z \, r \, dr \right|} \tag{23}$$

where S_z is the longitudinal component of the time-averaged Poynting vector and σ is the conductivity of the material. This parameter is related to the loss tangent, $\tan \delta$, and to the real part of the permittivity, ε', by:

$$\sigma = \omega \varepsilon' \tan \delta \quad . \tag{24}$$

Elsasser[2] introduces the dimensionless quantity R

$$\alpha = \sigma \sqrt{\frac{\mu_0}{\varepsilon_0}} \, R \quad . \tag{25}$$

For a plane wave propagating in an infinite medium of conductivity and dielectric constant ε, R has the value $1/\sqrt{\varepsilon'}$. Elasser computed the value of R for the three lowest order modes:

for the m=1, HE_{11}-mode:

$$R = \left| \frac{\frac{D-1}{v^2} \frac{Y_1^2 + \frac{1}{u^2} - \frac{1}{u^4}}{\frac{1}{u^2} + \frac{1}{v^2}} + (N^2 + Z^2) X + \frac{4\,NZ}{u^4}}{NX(D + Z^2) + NY(1 + Z^2) + \frac{2Z}{u^4}(D+N^2) - \frac{2Z}{v^4}(1+N^2)} \right| \quad , \tag{26}$$

where $\quad D = (n_1/n_2)^2$

$$X = Y_1^2 + \frac{2Y_1+1}{u^2} - \frac{1}{u^4} \quad ,$$

$$Y = -X_1^2 - \frac{2X_1-1}{v^2} - \frac{1}{v^4}$$

$$Z = \frac{D\,Y_1 + X_1}{Y_1 + X_1}$$

(The other quantities have been defined in Section 2.2.)

for $m = 0$, the H_{01}-mode

$$R = \left| \frac{Y_o^2 + \dfrac{2Y_o + 1}{u^2}}{Y_o^2 + \dfrac{2Y_o + 1}{u^2} - X_o^2 - \dfrac{2X_o-1}{v^2}} \right| \frac{1}{N} \qquad (27)$$

for $m = 0$, the E_{01}-mode

$$R = \left| \frac{\dfrac{D-1}{v^2} \dfrac{Y_o^2 + \dfrac{1}{u^2}}{\dfrac{1}{u^2} + \dfrac{1}{v^2}} + N^2 \left(Y_o^2 + \dfrac{2Y_o-1}{u^2}\right)}{D\,N\left(Y_o^2 + \dfrac{2Y_o+1}{u^2}\right) - N\left(X_o^2 + \dfrac{2X_o-1}{v^2}\right)} \right| . \qquad (28)$$

We have plotted in Figs. 12 and 13 the quantity $n_1 R$, for the three

lowest order modes and two different core indices, respectively,

1.500 and 5,667. As the frequency increases, all the curves exhibit

a maximum that is more pronounced for a higher core index. At high

frequency, the quantity R approaches the "plane-wave limit" $1/n_1$.

We also plotted for reference the fraction of the total power that

propagates in the core, assuming that only the mode in consideration

is present. We see that the maximum in the curves corresponds to the

rise of the power fraction. The maximum indicates that at intermediate

frequencies, the attenuation can be several times the high-frequency

limit, which is equal to the attenuation that a plane wave propagating

in an infinite expanse of core material would encounter. This result may

be understood in simple physical terms. At very low frequencies most of

the fields are outside of the core and therefore are subject to little

attenuation. As the frequency is increased, the fields become more con-

centrated within the core. In a ray-optics picture, this situation cor-

responds to rays that bounce back and forth between the boundaries of the

guide. The path followed by a ray is thus actually longer than if it

were propagating along the guide axis and therefore the attenuation per

physical length of guide is higher. At high frequencies, the

guide radius becomes very large compared to a wavelength and the

mode can be thought of as a plane wave propagating parallel to

the axis.
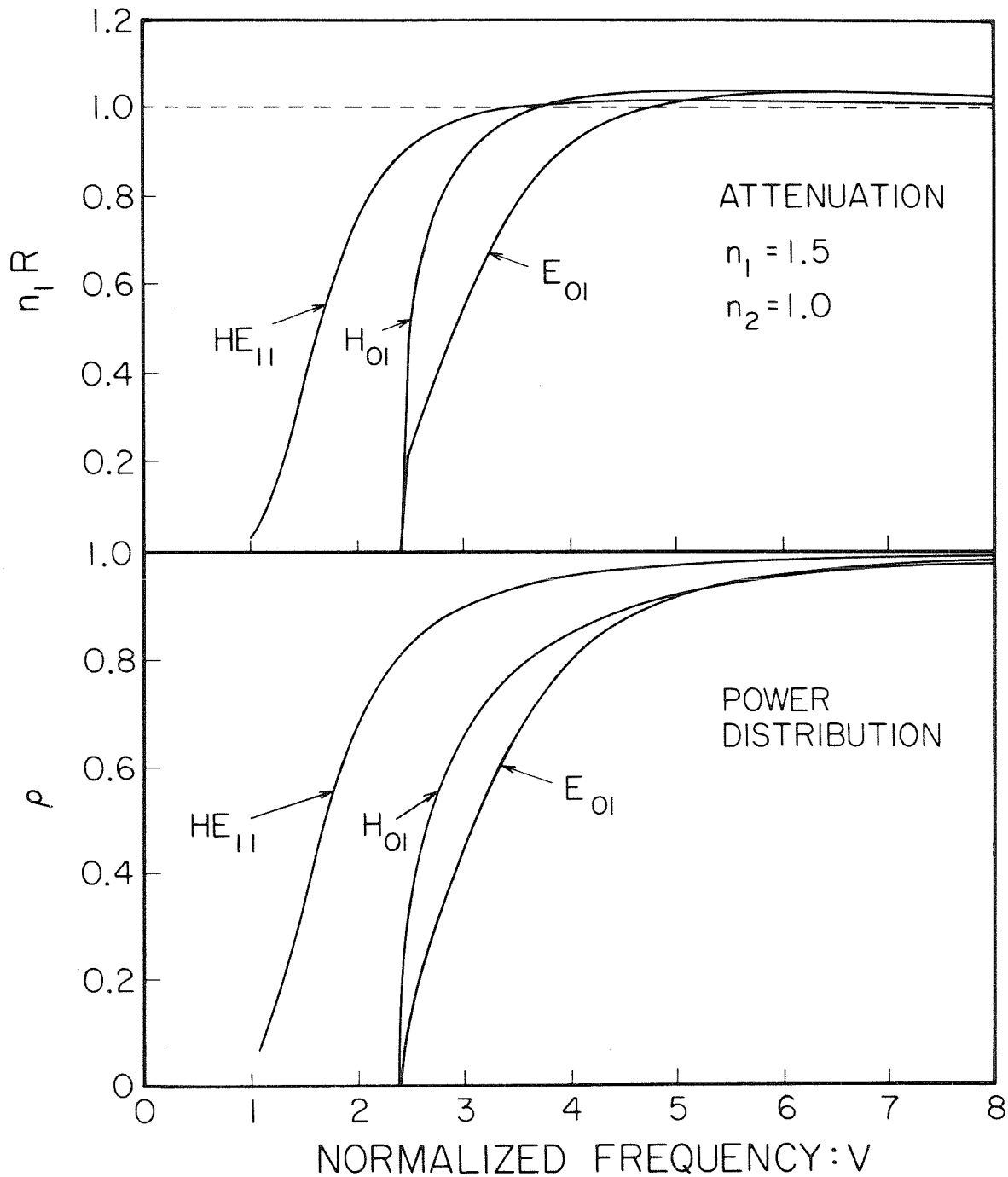
Figure 12. The attenuation of the three lowest-order modes of a round
fiber is plotted versus normalized frequency. The attenuation is normalized
by its high-frequency limit. The fraction of the power propagating inside
the core is shown in comparison.
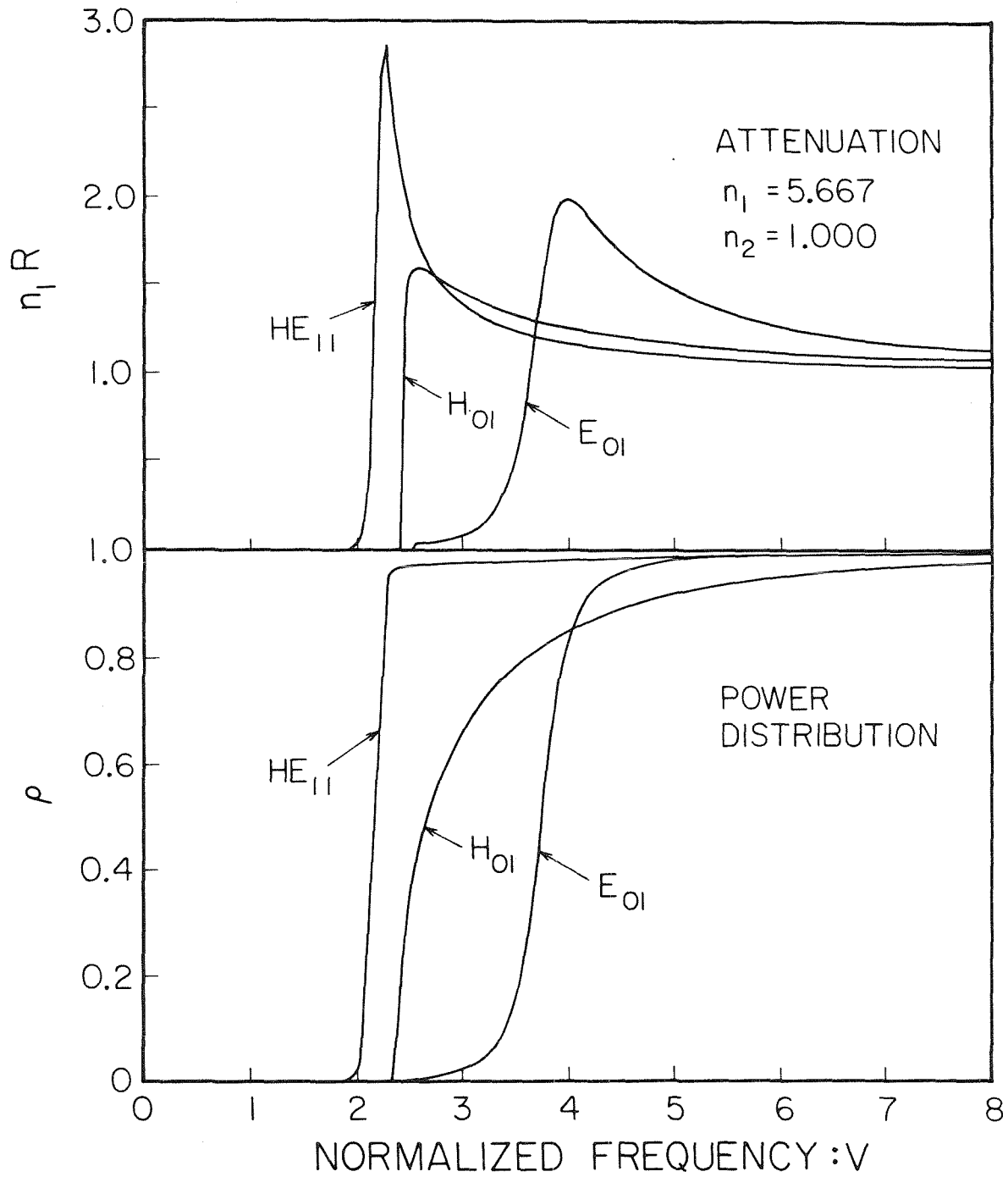
Figure 13. The attenuation of the three lowest-order modes of a round fiber is plotted versus normalized frequency. The attenuation is normalized by its high-frequency limit. The fraction of the power propagating inside the core is shown in comparison.

6. Attempt at a Practical Design

We will now consider from an engineering standpoint the feasibility of a dielectric fiber made of KRS-5 for long distance transmission of millimeter wave power.

The most important parameter of such a transmission system is the total loss per unit of length. The total propagation losses result from the dielectric losses in the core and cladding and from bending losses.

$$\alpha = \alpha_{core} + \alpha_{cladding} + \alpha_{bending} \qquad . \qquad (29)$$

In this analysis, we are interested in orders of magnitude rather than exact numbers. We will therefore consider that the dielectric losses are obtained by multiplying the material losses α_M

$$\alpha_{M_q} \simeq \frac{\pi}{\lambda_o} \, \varepsilon'_r \, \tan\delta \quad \text{for small } \tan\delta \text{ and } q=1,2 \qquad (30)$$

by the fraction of the power propagating in region q:

$$\alpha_{core} = \alpha_{M_1} \, \rho_{core} \qquad\qquad (31a)$$

$$\alpha_{cladding} = \alpha_{M_2} \, \rho_{cladding} \qquad . \qquad (31b)$$

The exact study of bending losses requires the analysis of the modes that propagate on a curved waveguide, and the reflection and radiation phenomena that occur at the transition between the straight and curved portions of guide. Several authors have proposed formulas for computing the bending losses. Neuman, et al [9] have shown that these formulas can be reduced to a common expression:

$$\alpha_R \simeq \frac{1}{R} \exp \left[- \frac{1}{6\pi^2} \frac{(R/\lambda_o)}{(r_o/\lambda_o)^3} \right] , \tag{32}$$

where R is the radius of curvature, λ_o is the wavelength in the outer medium, and r_o is the extension of the field in this region. (The fields outside the core behave like $K_1(r/r_o)$, which can be approximated by an exponential decay $\exp(-r/r_o)$.)

We may now compute the fiber losses for three cases of practical interest, namely, those fiber designs that have an attenuation comparable to metallic waveguides. We will assume that only the dominant HE_{11}-mode propagates in these fibers with infinite cladding.

a. KRS-5/Air Waveguide. As a benchmark value, we determine the radius a of the core that makes the dielectric losses correspond to the losses of conventional metallic waveguides at 94 GHz:

$$\alpha_{core} = 3 \text{ dB/m} = 3.45 \text{x} 10^{-4} \text{ mm}^{-1}$$

For very small V, we can approximate the dispersion relation of the HE_{11}-mode by [5]

$$B \simeq \frac{1.26}{V^2} \exp [-D/V^2] \tag{33}$$

where $D = 1 + (n_1/n_2)^2$. Also, we have seen earlier that the power distribution is given by

$$\rho_{core} = B + \frac{V}{2} \frac{dB}{dV} \tag{24}$$

and therefore,

$$\rho_{core} \simeq \frac{1.26}{V^4} D \exp(-D/V^2) \quad . \tag{34}$$

Because $\alpha_{core} = \rho_{core} \alpha_M$ this value of α_{core} corresponds to $\rho_{core} = 3.1 \text{x} 10^{-3}$ for KRS-5 (see Table 1), a very small amount of power flowing in the core. Knowing the value of ρ_{core}, we can now solve Eq. (34) by successive iterations and find that $V = 1.9$. From (33) and the definition of B we obtain for the propagation constant: $\beta/k = 1.0006$, with $k = 1.97 \text{ mm}^{-1}$ at 94 GHz. In order to compute the radiation losses, we must know r_o, the extension of the fields outside of the core, in the air. From the definition of the parameters, we have

$$1/r_o = (\beta^2 - k_o^2)^{\frac{1}{2}} \tag{35}$$

and therefore, r_o = 21.1 mm. The bending losses, for a bending

radius R = 200 mm, become α_R = 5.0x10^{-3}, and for R = 600 mm,

α_R = 2.2x10^{-4}, about 3 dB/meter or the same as the dissipative losses

in a WR-10 metallic waveguide.

   b. <u>Teflon/Air Waveguide</u>. Using the same steps as in case

a, we obtain successively

$$\rho_{core} = 0.12$$

$$V = 1.25$$

$$a = 0.51 \text{ mm}$$

$$\beta/k = 1.06$$

$$r_o = 1.44 \text{ mm}$$

$$\alpha_R = 5.1\text{x}10^{-8} \text{mm}^{-1} \text{ for } R = 200 \text{ mm}$$

$$\alpha_R = 1.7\text{x}10^{-18} \text{ mm}^{-1} \text{ for } R = 600 \text{ mm}$$

The claimed advantage of a high-index core is that it would be to

provide a better confinement of the fields inside the core. These

two cases demonstrate that this advantage is practical only if the core

material is low loss. KRS-5 is too lossy, and in order to achieve a

small dielectric loss, most of the power would actually travel outside of

the core; such a fiber suffers then from high bending losses because the mode

is loosely confined. Teflon has a lower dielectric loss than KRS-5.

To obtain losses comparable to metallic waveguides, we can guide 12%
of the power inside the core. This confinement is already sufficient
to lower the bending losses by several orders of magnitude.

      c. <u>KRS-5/Teflon/Air Waveguide</u>. The losses in this case are
worse than the losses in cases a and b. We must now add to the di-
electric losses in the KRS-5 core the losses in the Teflon cladding.
The cladding in all practical cases will be very large so that the
fields at the interface Teflon/air are negligible. Thus the losses
in the Teflon will be essentially the bulk losses and it will not be
possible to achieve a dielectric loss of 3 dB/m, no matter how small
we choose the core. Also, the guiding properties of the KRS-5 core
are degraded because the difference in index of refraction between
the core and the outer medium is now decreased (see the earlier dis-
cussion of propagation characteristics).

      We must remark that in case a and b the outer medium is indicated
as "air", but a practical realization will involve the use of a foamed
material that will approximate the dielectric properties of air:
$\varepsilon_r' \simeq 1$ and very small losses. This is required in order to supply
mechanical support and prevent the fields from coupling with external
objects.

      Finally, we must conclude that KRS-5 is not a suitable material
for a closely confined HE_{11} dielectric waveguide because of its high
losses. Teflon can be used (and is actually used in various applica-
tions) but only for short lengths.

TABLE 2

Dielectric properties used in the calculation of waveguide losses.[*]

(f = 94 GHz)

Material	ϵ_r'	Tan δ	$\alpha_M (mm^{-1})$
KRS-5	32	2×10^{-2}	1.11×10^{-1}
Teflon	2.1	2×10^{-3}	2.86×10^{-3}

* See Ref. III-2

7. Conclusions

We have presented the theory of dielectric fibers as applied to our case of interest, namely, a fiber of high refractive index and dimensions comparable to a wavelength. We observed that it is necessary to solve the exact characteristic equation rather than use the approximate formulas introduced for the study of optical waveguides. We pointed to the fact that information about the power distribution can be deduced from the dispersion characteristic. Finally, we noted that the attenuation on a high-index fiber can be several times the attenuation that would be expected from a bulk material loss figure.

We have applied these calculations to a guide made of KRS-5, because this material was originally thought to be low-loss. It also had the desirable mechanical properties that are necessary for making a flexible fiber: extrudibility, ductility. We compared our numerical results to Teflon fibers because they are used in practical applications such as couplers. A practical fiber must present *total* losses comparable to the losses of metallic waveguides. From our measurement of dielectric properties at 94 GHz (see Part III), it appears that KRS-5 is not at all a suitable material: Its losses are two order of magnitude too high. Even Teflon presents material losses that are about an order of magnitude larger than our target.

BIBLIOGRAPHY

1. E. Hondros and P. Debye, "Elektromagnetischen Wellen an
    Dielektrischen Drähten", Ann. Phys., Vol. 32, 1910, pp. 465-476.

2. W. Elsasser, "Attenuation in a Dielectric Circular Rod", J. Appl.
    Phys., Vol. 20, Dec. 1949, pp. 1193-1196.

3. C. Chandler, "Investigation of Dielectric Rod as Waveguide", J.
    Appl. Phys., Vol 20, Dec. 1949, pp. 1188-1192.

4. E. Gloge, "Weakly Guiding Fibers", Appl.Opt., Vol. 10, Oct. 1971,
    pp. 2252-2258, and references therein contained.

5. H.-G. Unger, Planar Optical Waveguides and Fibers , Clarendon
    Press, Oxford, 1977.

6. D. Krumbholz, E. Brinkmeyer and E.-G. Neumann, "Core/Cladding
    Power Distribution, Propagation Constant and Group Delay: Simple
    Relations for Power-law Graded-index Fibers", J. Opt. Soc. Am.,
    Vol. 70, Feb. 1980, pp. 179-183.

7. S. Nemoto and T. Makimoto, "A Relationship between Phase and Group
    Indices of Guided Modes in Dielectric Waveguides", Int. J. Elec.,
    Vol. 40, 1976, pp. 187-190.

8. S. Kawakami, "Relations between Dispersion and Power Flow Distri-
    bution in a Dielectric Waveguide", J. Opt. Soc. Am., Vol. 65,
    Jan. 1975, pp. 41-45.

9. E.-G. Neumann and H.-D. Rudolph, "Radiation from Bends in Dielectric
    Rod Transmission Lines", IEEE Trans. Microwave Th. Tech., Vol.
    MTT-23, Jan. 1975, pp. 142-145.

Part II.   Rectangular Dielectric Waveguides

1.   Introduction

Rectangular dielectric waveguides of high permittivity ($\varepsilon_r' \gtrsim 10$)

have been proposed as practical waveguiding structure for use in

millimeter-wave integrated circuits (MMIC) [1,2]. The use of high-

resistivity material is particularly indicated as active devices can

be fabricated directly into the transmission line.

Rectangular guides for integrated optics have been investigated

by Marcatili [3] and Goell [4]. These guides have, for ease of fabrication,

transverse dimensions of the order of 10 wavelengths. Single-mode

operation is obtained by choosing refractive indices of the guide and

the surrounding medium that differ by 1% or less. Table I compares

the typical figures for optical and millimeter-wave dielectric guides.

Higher dielectric ratios (K_1/K_2) become practical at millimeter

wavelengths. Also, they provide a better confinement of the fields

and therefore tighter radii of curvature can be tolerated. Such a

waveguide may have an attenuation somewhat higher than a conventional

metallic waveguide, but the typical lengths are also quite shorter:

For a high-resistivity GaAs-guide ($\rho = 10^8$ Ω-cm) the attenuation at

94 GHz is 0.10 dB/cm compared to 0.03 dB/cm for a silver WR-10

guide.

Various practical devices for millimeter-wave applications that

utilize a rectangular dielectric waveguide have been proposed or are

actually being used: directional couplers [5], balanced mixers [5],

phase shifters [6,7], scanning antenna [8], channel-dropping filters [9]. The theoretical analysis of these devices has been based, in all cases, on the analytical solution proposed by Marcatili [3], which can be easily expressed in simple closed forms. We have investigated rectangular dielectric waveguides and found that the approximations introduced by Marcatili are not valid when the permittivity of the guide is high compared to the outer medium.

Several authors have proposed methods for the study of rectangular guides: Knox et al [1] (modification of Marcatili's analysis), Schlosser [10] and Solbach [11] (mode matching), Goell [4] (expansion in circular harmonics), and Yeh [12,13] (finite-elements), among others. They limited their analysis to relatively small values of the permittivity ($\varepsilon_r' \simeq 2.5$) and, with the exception of Solbach [11], their results give only the propagation characteristics, i.e., the guide wavelength as a function of the free-space wavelength for the various modes but not the field distributions.

Because none of these methods seemed to suit our purpose we have developed a numerical technique based on finite-differences (FD) for computing accurate characteristics and field distributions. This FD method is efficient and flexible and can be applied to a wide variety of dielectric waveguide problems: The waveguide can have a complex shape, a non-uniform permittivity profile or even include metal electrodes.

We will first review Maractili's approach and point out the restrictive assumptions upon which his study is based. We will then

TABLE I

Comparison between millimeter-wave and optical waveguides (typical values)

	MM-wave	Optical
Dielectric material (guide)	alumina;semiconductors	glass;semiconductors
Dielectric material (surrounding medium)	air;plastic	glass;semiconductors
K_1	10-15 or higher	2-4;12
K_2	1;2.5	2-4;12
index ratio $(\sqrt{K_1/K_2})$	2	1.1-1.01
waveguide width (in λ_g)	0.5	2-10
radius of curvature (in λ_g)	2-5	30-1000

describe briefly the methods proposed by Knox et al [1], Solbach [11] and Yeh [12,13]. Finite-differences can be applied to a wave propagation problem by discretizing either the wave equation or a variational expression. We have analyzed both approaches and found that only the latter one can be used. Finally we will present our results for the dispersion characteristics and field distributions of the rectangular guide and compare them to Marcatili's solution.

2. Marcatili's Solution

Marcatili [3] analyzed the mode properties of a guide consisting of a rectangular core surrounded by several dielectrics of different permittivity. We will present this analysis in a simplified form, by considering the outer medium to be infinite and homogeneous (see Fig. 1).

2.1. Assumptions

A closed form is only possible if one introduces a drastic simplification of the problem. For a well-guided mode, as is expected by analogy with a round fiber, the fields decay exponentially in regions 2,3,4,5, away from the core (see Fig. 1). Therefore, most of the power propagates in region 1, only a small fraction in regions 2-5 and an even smaller part in the four corner areas. Consequently, only a small error is introduced if the fields are matched along the
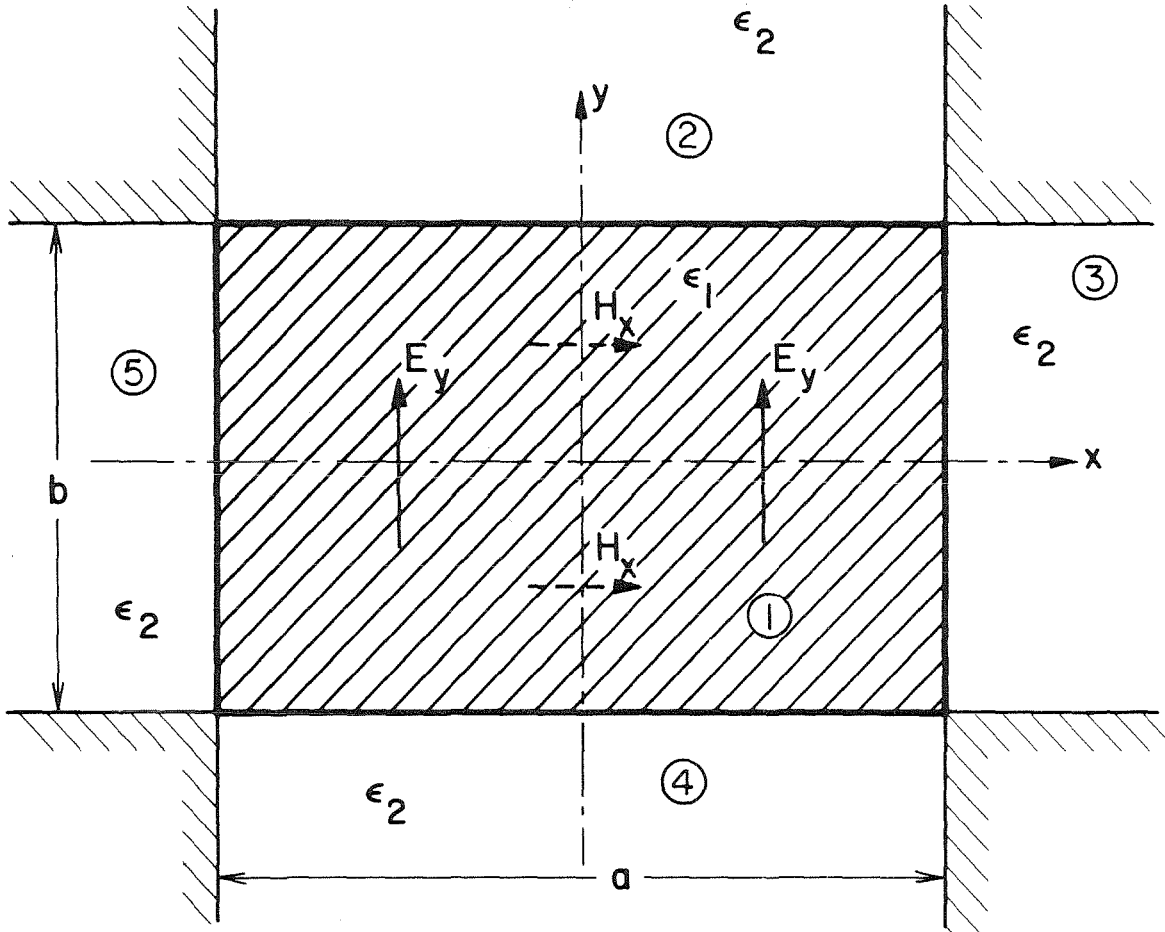
Figure 1. Rectangular dielectric waveguide: Marcatili's analysis simplifies the problem by neglecting the corner areas. The arrows indicate the direction of the dominant transverse field components for the E_{11}^y-mode.

edges of regions 1-2,1-3,1-4 and 1-5 and the corner areas are neglected.
This matching can be achieved by assuming simple field distributions.
The field components are assumed to vary[*]:

    - sinusoidally along x and y, in region 1;

    - sinusoidally along x and exponentially along y in region 2;

    - sinusoidally along y and exponentially along x in region 3.

The separation constant along x must be the same in region 1 and 2
and independent of y. Similarly, the separation constant along y
are identical in regions 1 and 3 and independent of x. We expect
that these modes will be hybrid because of the field variations
along the dielectric interfaces. In a ray picture, guidance occurs
because of total internal reflection. If the index ratio $\sqrt{K_1/K_2}$ is
close to unity, then total internal reflection occurs when the wavelets
that make a mode are incident on the interfaces at grazing angles.
As we will see, this implies that the largest fields components
are the ones perpendicular to the direction of propagation: The
modes are of the quasi-plane wave kind and can be grouped into two
families, according to their polarization: E_{pq}^y and E_{pq}^x [**]. The field
configurations for the lowest E_{pq}^y- and E_{pq}^x-modes are sketched in Fig. 2.

    To summarize, the analysis rests on the following three assumptions:

    (i) the index ratio is small, i.e., $\sqrt{K_1/K_2} - 1 \ll 1$;

---

[*] By using symmetry we need only to consider the upper right quadrant
of Fig. 1: The fields must be either symmetric or antisymmetric
with respect to the x- and y-axis.

[**] The superscript indicates the direction of polarization of the main $\vec{E}$-
field component while the subscripts denote the number of maxima
respectively in the x- and y-directions.

49

E_y OR H_x

$\cos k_x x$

CONSTANT $e^{-x/\xi}$

x

E_y OR H_x

x

y

CONSTANT $e^{-y/\eta}$

$\cos k_y y$

E_y
OR H_x

E_{11}^y

E_{21}^y

b

a

E_{12}^y

E_{22}^y

E_y
OR H_x

(a)

E_x OR H_y

$\cos k_x x$

CONSTANT $e^{-x/\xi}$

x

E_x OR H_y

x

y

CONSTANT $e^{-y/\eta}$

$\cos k_y y$

E_x
OR H_y

E_{11}^x

E_{21}^x

E_{12}^x

E_{22}^x

E_x
OR H_y

(b)

ELECTRIC FIELD   MAGNETIC FIELD
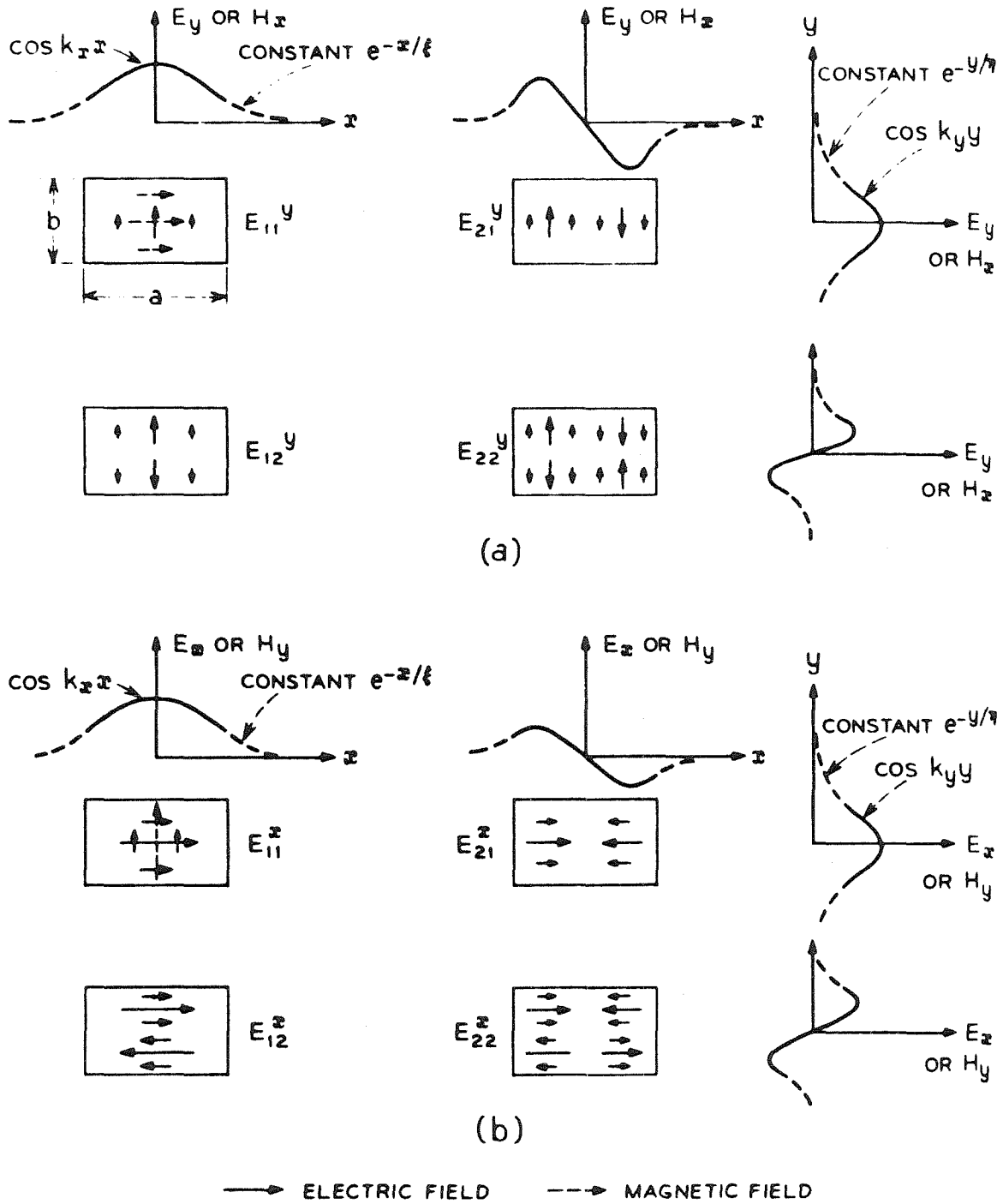
Figure 2. Sketch of the field components for the four dominant E_{pq}^y - and E_{pq}^x -modes (from Marcatili, Ref. 3).

(ii) the power propagating in the corner areas can be neglected;

(iii) the boundary conditions should be satisfied only for the dominant components of the $\vec{E}$- and $\vec{H}$-fields.

2.2. Derivation and Properties of the E_{pq}^x-Modes

The field components in the nth area of Fig. 1 are: [*]

$$H_x^n = \begin{cases} A_1 \cos(k_x x + \alpha) \cos(k_y y + \beta) & \text{for } n = 1 \\[2em] A_2 \cos(k_x x + \alpha) \, e^{-jk_{y_2} y} & \text{for } n = 2 \\[2em] A_3 \cos(k_y y + \beta) \, e_3^{-jk_{x_3} x} & \text{for } n = 3 \end{cases}$$

$$H_y^n = 0 \tag{1}$$

$$H_z^n = \frac{j}{k_z} \frac{\partial H_x^n}{\partial x}$$

$$E_x^n = - \frac{1}{\omega \varepsilon_o K_n k_z} \frac{\partial^2 H_x^n}{\partial x \, \partial y}$$

$$E_y^n = \frac{k_o^2 K_n - k_{yn}^2}{\omega \varepsilon_o K_n k_z} H_x^n$$

---

[*] The common factor $\exp j(\omega t - k_z z)$ has been omitted.

$$E_z^n = \frac{1}{\omega \varepsilon_o K_n} \frac{\partial H_x^n}{\partial y}$$

in which α and β determine the symmetry (or antisymmetry), respectively with the x- and y-axis by taking the values 0° or 90°. In the nth medium the separation constants are related to the free-space wave-number, k_o, and the permittivity K_n * by:

$$k_{x_n}^2 + k_{y_n}^2 + k_{z_n}^2 = \omega^2 \varepsilon_o \mu K_n = k_n^2 \tag{2}$$

To be able to match the fields at the interface between regions 1 and 2 we have assumed in Eqs. (1)

$$k_{x_1} = k_{x_2} = k_x \tag{3}$$

and, similarly, to match the fields between media 1 and 3

$$k_{y_1} = k_{y_3} = k_y \quad .$$

If we assume that the index ratio is close to unity, that is

---

* We are interested in the case where $K_2 = K_3 < K_1$ but the analysis is similar if $K_2 \neq K_3$.

$$\sqrt{K_1/K_2} - 1 \ll 1 \qquad , \tag{5}$$

We obtain, by using Eq. 2 that

$$k_x, \; k_y \ll k_z \qquad . \tag{6}$$

Together, Eqs. (1) and (6) imply that the relative amplitudes of the field components are different:

$$H_x \sim 1$$

$$H_z \sim \frac{k_x}{k_z} \simeq \frac{k_x}{k}$$

$$E_x \sim \frac{k_x k_y}{k \, k_z} Z_o \simeq \left(\frac{k_x}{k_z}\right)^2 Z_o \tag{7}$$

$$E_y \sim \frac{k_x^2 + k_y^2}{k \, k_z} Z_o \simeq \frac{k^2}{k_z^2} Z_o \simeq Z_o$$

$$E_z \sim \frac{k_y}{k} Z_o$$

where Z_o is the vacuum impedance. In order to satisfy the boundary conditions, we must assure, at the interface between regions 1 and 2 the continuity of the tangential fields, H_z, H_x, E_z and E_x. However, using Eq. (7), we see that

$$H_z \ll H_x \qquad \text{and} \qquad E_x \ll E_z.$$

Therefore, by matching, at $y = b/2$, the dominant components H_x and E_z, we obtain

$$A_1 \cos(k_y \frac{b}{2} + \beta) = A_2 e^{jk_{y_2} \frac{b}{2}} \tag{8}$$

$$\frac{k_y}{\omega\varepsilon_o K_1} A_1 \sin(k_y \frac{b}{2} + \beta) = \frac{j}{\omega\varepsilon_o K_2} k_{y_2} A_2 e^{jk_{y_2} \frac{b}{2}} \tag{9}$$

Similarly, at the boundary between media 1 and 3, we must match the tangential fields H_z, E_y and E_z. Considering their relative amplitudes, we see that

$$E_z \ll E_y$$

and consequently, we will match only H_z and E_y at $x = a/2$:

$$\frac{k_x}{k_z} A_1 \sin(k_x \frac{a}{2} + \alpha) = \frac{j}{k_z} k_{x_3} A_3 e^{-jk_{x_3} a/2} \tag{10}$$

$$\frac{k_1^2 - k_y^2}{\omega\varepsilon_o K_1} \frac{1}{k_z} A_1 \cos(k_x \frac{a}{2} + \alpha) = \frac{k_3^2 - k_y^2}{\omega\varepsilon_o K_3} \frac{1}{k_z} A_3 e^{-jk_{x_3} a/2} \tag{11}$$

These equations serve to determine the amplitude coefficients A_2 and A_3 in terms of an arbitrary constant, A_1. Moreover, by taking the rations, respectively of Eq. 9 to Eq. 8 and Eq. 11 to Eq. 10, we obtain the characteristic equations

$$\tan(k_y \frac{b}{2} + \beta) = \frac{K_1}{K_2} \frac{jk_{y_2}}{k_z} \tag{12}$$

and

$$\tan(k_x \frac{a}{2} + \alpha) = j \frac{k_{x_3}}{k_x} \frac{K_1}{K_3} \frac{k_3^2 - k_y^2}{k_1^2 - k_y^2} \quad .$$

In the latter expression, we can rewrite the right-hand side

$$\frac{K_1}{K_3} \frac{k_3^2 - k_y^2}{k_1^2 - k_y^2} \simeq \frac{K_1}{K_3} \frac{k_3^2}{k_1^2} = 1$$

and the relation becomes

$$\tan(k_x \frac{a}{2} + \alpha) = \frac{j\, k_{x_3}}{k_x} \quad . \tag{13}$$

Eqs. (12) and (13) have a physical interpretation: They are the characteristic equations of two independent slab problems. The first relation represents a slab of permittivity K_1 parallel to the x-axis and of thickness b/2 while the second equation corresponds to a slab of permittivity K_1 that is parallel to the y-axis and of thickness a/2.

Finally, we can define a parameter ρ that will indicate the dominance of E_z over H_z or vice-versa:

$$\rho = \frac{\left|E_z\right|_{max}}{\left|H_z\right|_{max}} \; \frac{1}{\dfrac{Z_o}{k_z/k_o}} \quad , \tag{14}$$

The quantity $Z_o/(k_z/k_o)$ is the impedance of a plane wave propagating in a medium of apparent index equal to the normalized wavenumber (k_z/k_o). For the E_{pq}^y - mode, we obtain:

$$\rho[E_{pq}^y] = \left(\frac{k_z}{k_o}\right)^2 \frac{1}{K_1} \frac{k_y}{k_x} \quad . \tag{15}$$

This quantity will be useful for comparing our numerical solution to the approximate theory.

2.3. Derivation and Properties of the E_{pq}^x -Modes

These modes are qualitatively the same as the E_{pq}^y -modes: They correspond to the orthogonal polarization. To obtain these modes, we proceed by duality[3] and change E to H, μ to $-\varepsilon$ and vice-versa. The field components are then:

$$E_x^n = \begin{cases} B_1 \cos(k_x x + \alpha) \cos(k_y y + \beta) & \text{for } n=1 \\[2em] B_2 \cos(k_x x + \alpha) \, e^{-jk_{y_2} y} & \text{for } n=2 \\[2em] B_3 \cos(k_y y + \beta) \, e^{-jk_{x_3} x} & \text{for } n=3 \end{cases}$$

$$E_y^n = 0$$

$$E_z^n = -\frac{j}{k_z}\frac{\partial E_x^n}{\partial x}$$

$$H_x^n = \frac{1}{\omega\mu_o K_n k_z}\frac{\partial^2 E_x^n}{\partial x\,\partial y} \tag{16}$$

$$H_y^n = \frac{k_o^2 K_n - k_{yn}^2}{\omega\mu_o K_n k_z} E_z^n$$

$$H_z^n = -\frac{1}{\omega\mu_o K_n}\frac{\partial E_x^n}{\partial y} \qquad .$$

Using the same approximations as in Section 2.2, from the boundary conditions, we obtain that the coefficients are related by:

$$B_2 = B_1 \cos(k_y \frac{b}{2} + \beta)\, e^{jk_{y_2}\frac{b}{2}} \tag{17}$$

$$B_3 = B_1 \frac{k_x}{jk_{x_3}} \sin(k_x \frac{a}{2} + \alpha)\, e^{jk_{x_3}\frac{a}{2}} \tag{18}$$

and the characteristic equations are:

$$\tan(k_y \frac{b}{2} + \beta) = \frac{k_{y_2}}{k_z} \tag{19}$$

and
$$\tan(k_x \frac{a}{2} + \alpha) = \frac{K_1}{K_3} \frac{jk_x}{k_x} \qquad , \qquad (20)$$

As expected, in the case of a square waveguide surrounded on all sides by the same homogeneous medium, the E^y_{pq} - and the E^x_{pq} -modes are degenerate. For the E^x_{pq} -modes, the parameter ρ is

$$\rho[E^x_{pq}] = \frac{k_x}{k_y} K_1 \qquad , \qquad (21)$$

2.3. Characteristic Equations: Closed-form Solutions

For well-guided modes, most of the power propagates in region 1 and therefore

$$k_x, k_y \ll k_z \qquad .$$

The characteristic equation can then be solved in closed-form [3]. For the E^y_{pq} -modes, we have

$$A = \frac{\pi}{k_o \sqrt{K_1 - K_2}} \qquad (22)$$

$$k_x = \frac{p\pi}{a}(1 + \frac{2A}{\pi a})^{-1} \qquad (23)$$

$$k_y = \frac{q\pi}{b}(1 + \frac{1 + K_2/K_1}{\pi b} A)^{-1} \qquad (24)$$

$$k_z = (k_1^2 - k_x^2 - k_y^2)^{\frac{1}{2}} \tag{25}$$

$$jk_{x_3} = \left[k_x^2 - \left(\frac{\pi}{A}\right)^2\right]^{\frac{1}{2}} \tag{26}$$

$$jk_{y_2} = \left[k_y^2 - \left(\frac{\pi}{A}\right)^2\right]^{\frac{1}{2}} \tag{27}$$

For the E_{pq}^x-modes, we have, together with Eqs. (22) and (25-27):

$$k_x = \frac{p\pi}{a}\left[1 + \frac{1 + K_2/K_1}{\pi\ a}A\right]^{-1} \tag{28}$$

$$k_y = \frac{q\pi}{b}\left[1 + \frac{2A}{\pi b}\right]^{-1} \quad . \tag{29}$$

The exact solutions to the characteristic equations and these closed-form expressions differ noticeably only in the cutoff region of a given mode: The approximate solution predicts a sharper drop in the phase parameter as the frequency is lowered.

These modes exhibit a finite cutoff frequency while we know that the lowest order mode should have a zero cutoff frequency. At low frequency, the wavelength is larger than the physical dimensions of the guiding structure. By analogy with the round fiber, we expect that the fundamental mode remains guided no matter how small the (normalized) frequency becomes.

As mentioned in Section 1, several authors have used the closed-form expressions to study high-permittivity guides. We have plotted

MODES OF A RECTANGULAR GUIDE (MARCATILI'S APPROXIMATION)
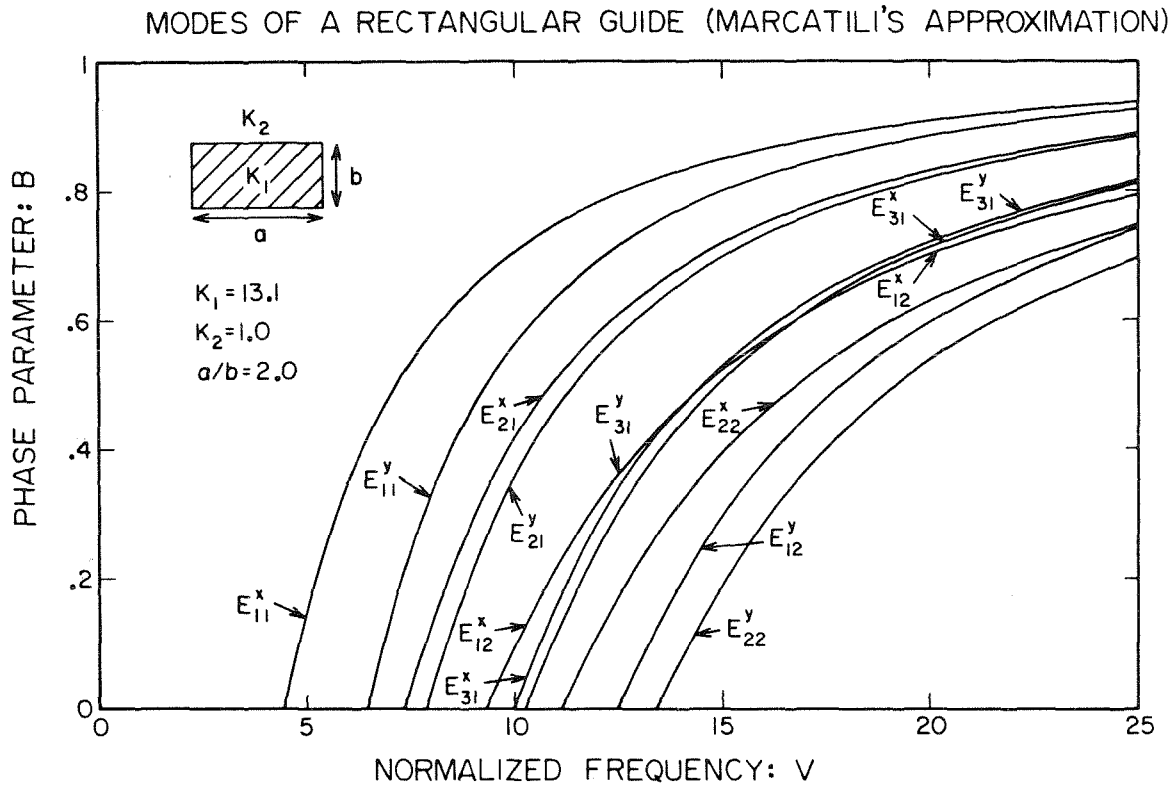
Figure 3. Dispersion characteristics of a rectangular dielectric wave-guide of high permittivity (K_1 = 13.1) computed by using Marcatili's closed-form solutions. These equations predict erroneously that the dominant E_{11}^y-mode has a non-zero cutoff frequency.

in Fig. 3 the dispersion characteristics, as computed by Eqs. 22-29,

for a rectangular guide made of GaAs (K_1=13.1). Later on, we will com-

pare these curves with our FD calculations.

3. Review of Solutions

We will describe here briefly some alternative methods that have

been proposed for the solution of rectangular dielectric waveguides.

3.1. Effective Index

As we remarked in 2.2 the characteristic equations obtained by

Marcatili correspond to two independent slab problems. Knox et al [1]

have proposed to improve on this solution by coupling the two slab

configurations. First, the slab depicted in Fig. 4.a is solved which

results in a value for the separation constant k_y. The permittivity of

the second slab (Fig. 4.b) is then modified from K_1 to

$$K_e = K_1 - (k_y/k_o)^2 \quad , \tag{30}$$

and the second separation constant k_x is obtained. The propagation

constant k_z is finally computed by using Eq. 25 that relates the various

constants to the free-space wavenumber k_o.

This approach does not overcome the limitations encountered with

Marcatili's: In practice, even for higher dielectric constants, the

dispersion curves obtained by these two methods differ very little.
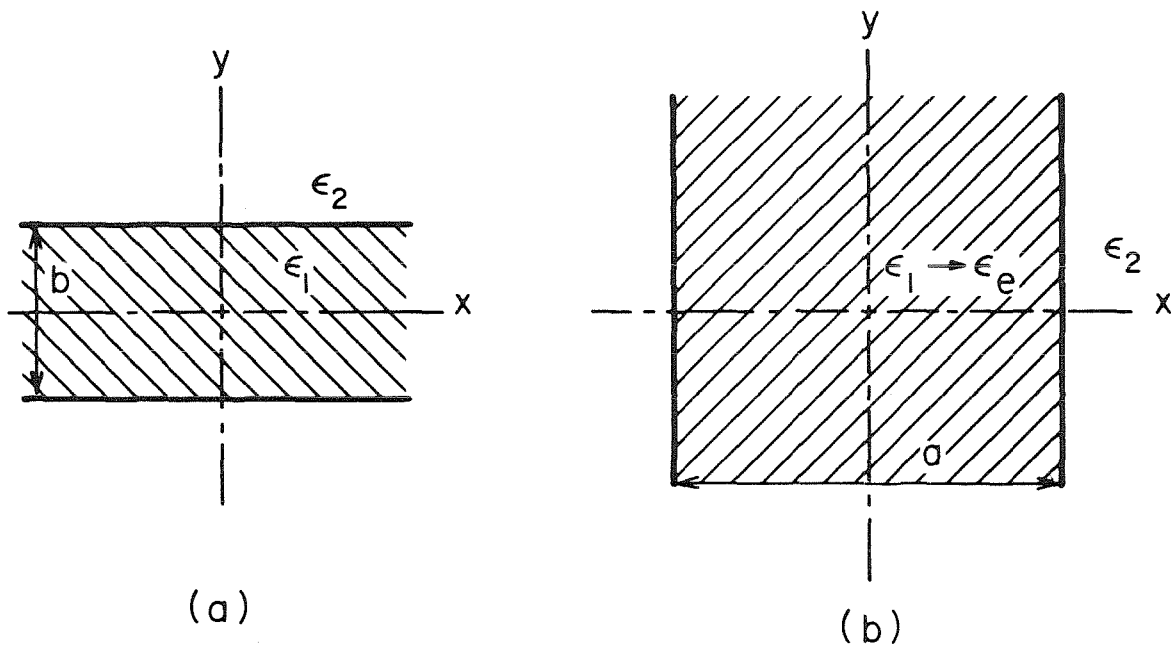
Figure 4. Effective index method: The two independent slab problems are coupled by solving one slab for the separation constant k_y and then modifying the dielectric constant of the other slab in order to determine the other transverse separation constant k_x.

3.2. Mode-matching

This technique was introduced by Schlosser [10] for the study of metallic waveguides partially filled with dielectric and applied to image lines by Solbach [11].

If we consider the problem illustrated by Fig. 5, the method proceeds as follows:

- a finite eigenvalue problem is defined by placing electric walls at a finite distance from the guide;

- in each region, I to IV, the fields are expanded in a complete set of waveguide modes that must satisfy only the boundary conditions on the electric and magnetic walls: The interfaces are not considered;

- the coefficients of the expansions (up to a certain order) are then obtained by matching the fields at the various interfaces: This results in a characteristic determinant that must be solved numerically. The approximate solution proposed by Marcatili [3] is in fact the lowest order approximation by mode-matching, i.e., the expansions are limited to their first time.

The search for the roots of this equation must be made in the complex β plane because some of the expansion terms correspond to modes beyond cutoff.

This method does not appear to be flexible enough for our purposes. For example, it is limited to simple rectangular geometries.

$$\theta = \begin{bmatrix} \phi_p \\ \psi_p \end{bmatrix}$$

and

$$k_A^2 = \left(\frac{\omega}{c}\right)^2 (\bar{\beta}^2 - 1) \quad . \tag{48}$$

is the eigenvalue.

It has been shown that the operators L_p and M_p are self-adjoint [19] and thus the eigenvalues k_A^2 are the stationary values of the expression:

$$k_A^2 = - \frac{\sum\limits_{p} \int\limits_{S_p} \theta^T L_p \theta \, dS}{\sum\limits_{p} \int\limits_{S_p} \theta^T M_p \theta \, dS} \quad . \tag{49}$$

By expanding this relation, we obtain the following variational principle for k_A^2

$$\delta J = \delta \sum\limits_{p} \left[\tau_p \int\limits_{S_p} \nabla_t^2 \phi_p \, dS + \bar{\beta}^2 \tau_p K_p \int\limits_{S_p} \psi_p \nabla_t^2 \psi_p \, dS \right]$$

$$\tag{50}$$

$$+ k_A^2 \left[\sum\limits_{p} \int\limits_{S_p} \phi_p^2 \, dS + \bar{\beta}^2 K_p \int\limits_{S_p} \psi_p^2 \, dS \right] = 0$$

which can be further simplified (by use of the divergence theorem) so that it involves only first-order derivatives [18,20]:

$$J = \sum_p \tau_p \int_{S_p} |\nabla_t \phi|^2 \, dS + \bar{\beta}^2 \tau_p K_p \int |\nabla_t \psi|^2 \, dS$$

(51)

$$+ 2\tau_p \bar{\beta}^2 \int_{S_p} (\nabla_t \psi \times \nabla_t \phi)_z \, dS - k_A^2 \left[\int_{S_p} |\phi_t|^2 \, dS + \bar{\beta}^2 \int_{S_p} |\psi_p|^2 \, dS \right]$$

This last relation will be the basis of our FD procedure.

4.4. FD: Variational Approach

For treating the problem of a rectangular dielectric guide, we need first to define a finite cross section by enclosing the guide in a "box" (electric walls) sufficiently large so that it will not perturb the modes. Again, because of symmetry, we need to treat only one quadrant. The longitudinal electric field, E_z, must be either symmetric (magnetic b.c.) or antisymmetric (electric b.c.) with respect to the x- and y-axes while the longitudinal magnetic field, H_z, has the opposite symmetry. We then superpose a mesh that covers the region of interest with rectangular elements (Fig. 6): These elements are chosen so that the permittivity is constant inside each element and the electric and magnetic walls each divide a row of
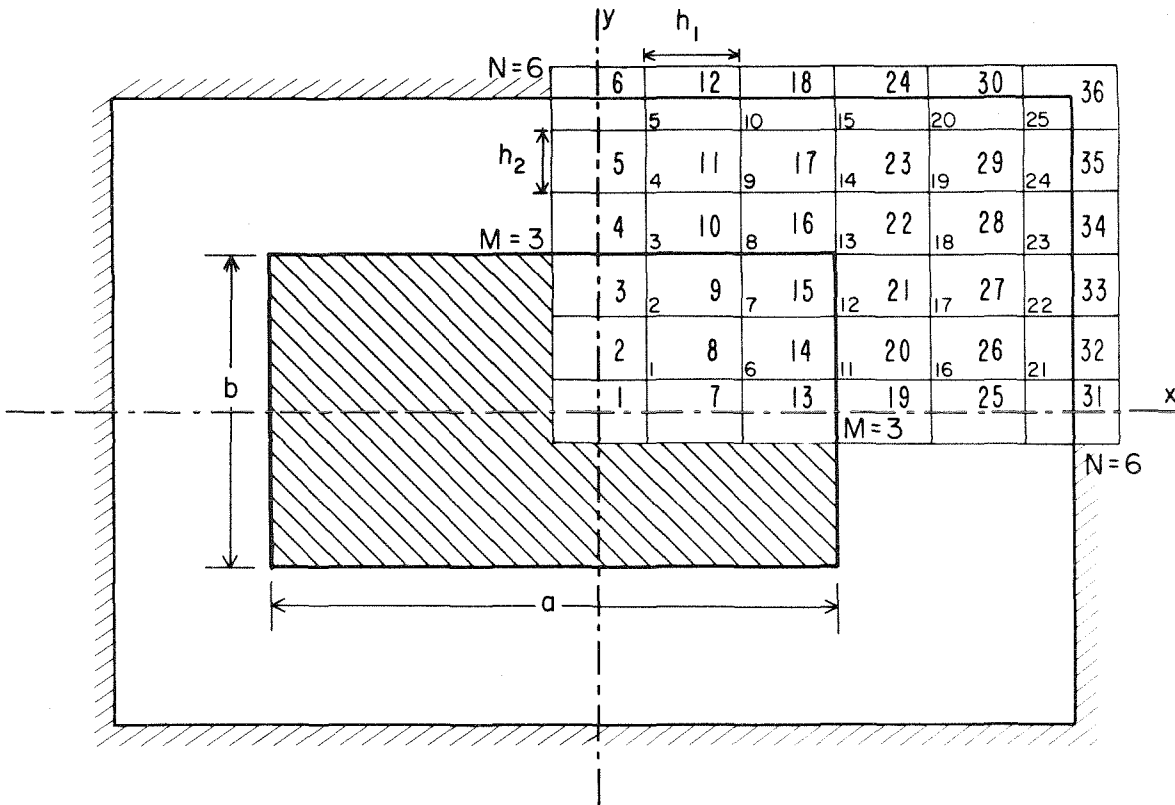
Figure 6. Before applying the FD-approximations, the dielectric guide is enclosed in a box (metallic wall boundary conditions) and the area of interest is covered by a rectangular grid. The permittivity inside each element must be uniform.

elements in two equal halves,

Consider one such element S_p (Fig. 7). The contribution of this element of the variational expression J can be evaluated by using FD approximations [16,20].* Using ϕ_i and ψ_i to denote the field values at point i, we have

$$\int_{S_p} \phi^2 \, dS \simeq \frac{h_1 h_2}{4} (\phi_1^2 + \phi_2^2 + \phi_3^2 + \phi_4^2)$$

(52)

$$\int_{S_p} \psi^2 \, dS \simeq \frac{h_1 h_2}{4} (\psi_1^2 + \psi_2^2 + \psi_3^2 + \psi_4^2)$$

$$\int_{J_p} |\nabla_t \phi|^2 \, dS = \int_0^{h_2} dy \int_0^{h_1} \left(\frac{\partial \phi}{\partial x}\right)^2 dx + \int_0^{h_1} dx \int_0^{h_2} \left(\frac{\partial \phi}{\partial y}\right)^2 dy$$

For the first term, we assume that $\frac{\partial \phi}{\partial x}$ has the constant value $\frac{\phi_3 - \phi_1}{h_1}$ on the segment 1-3 and the constant value $\frac{\phi_4 - \phi_2}{h_1}$ on the segment 1-2. We then integrate with respect to y and apply the trapezoidal rule:

---

* The grid lines are aligned parallel to the x-,y-axes. For convenience we assume that the coordinates of point 1 are (0,0).
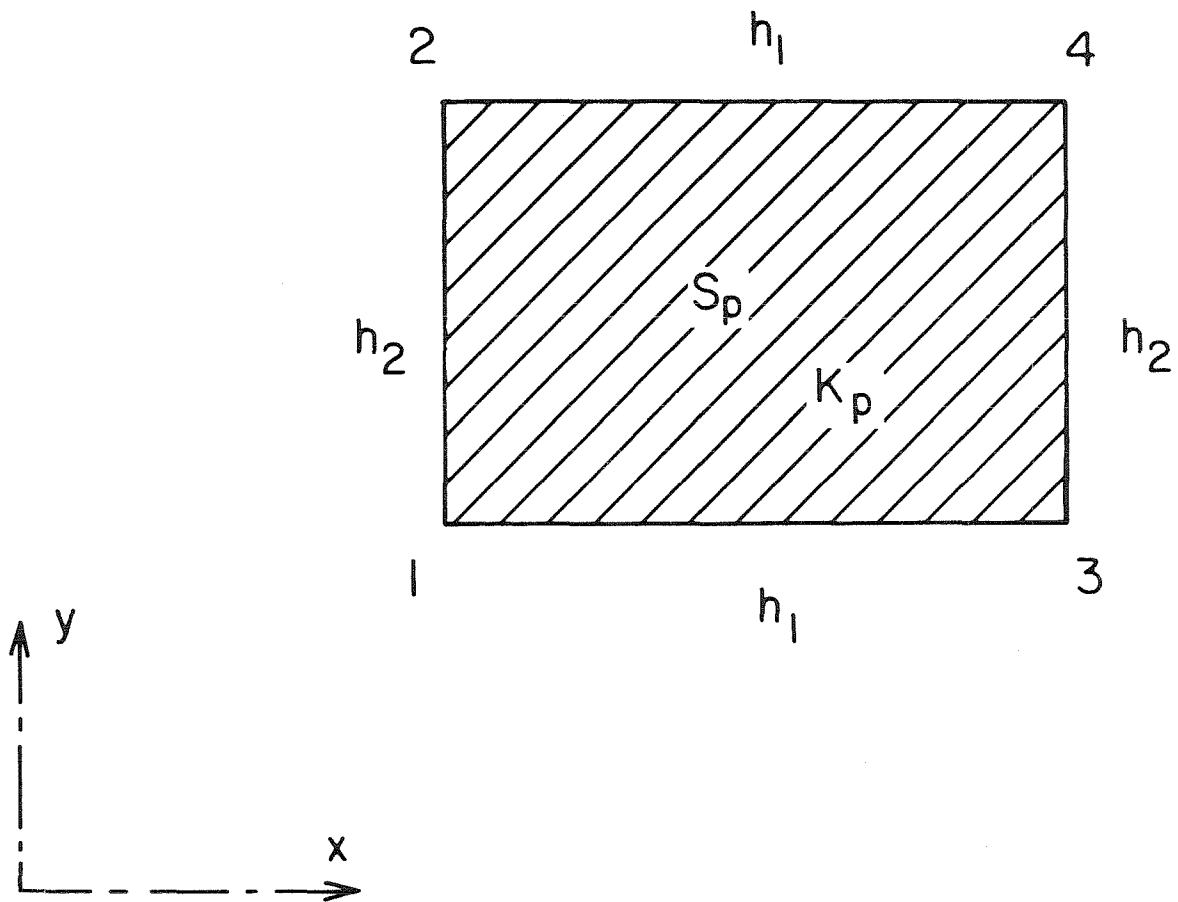
Figure 7. Typical rectangular element used for FD-approximations.

$$\int_{o}^{h_2} dy \int_{o}^{h_1} (\frac{\partial\phi}{\partial x})^2 \, dx \simeq h_1 \int_{o}^{h_2} dy \; (\frac{\partial\phi}{\partial x})^2$$

$$\simeq \frac{h_1 h_2}{2} \left[(\frac{\phi_4 - \phi_2}{h_1})^2 + (\frac{\phi_3 - \phi_1}{h_1})^2 \right]$$

Likewise, we obtain for the second term

$$\int_{o}^{h_1} dx \int_{o}^{h_2} (\frac{\partial\phi}{\partial y})^2 \, dy \simeq \frac{h_1 h_2}{2} \left[(\frac{\phi_2 - \phi_1}{h_2})^2 + (\frac{\phi_4 - \phi_3}{h_2})^2 \right]$$

so that,

$$\int_{S_p} |\nabla_t \phi|^2 \, dS \simeq \frac{h_1 h_2}{2} \left[(\frac{\phi_4 - \phi_2}{h_1})^2 + (\frac{\phi_3 - \phi_1}{h_1})^2 + (\frac{\phi_2 - \phi_1}{h_2})^2 + (\frac{\phi_4 - \phi_3}{h_2})^2 \right] . \quad (53)$$

A similar expression is obtained for $\displaystyle\int_{S_p} |\nabla \psi|^2 \, dS$.

Finally, each term of $\displaystyle\int_{S_p} (\nabla_t \psi \times \nabla_t \phi)_z \, dS$ is integrated as follows:

$$\int_{S_p} \frac{\partial \phi}{\partial y} \frac{\partial \psi}{\partial x} \, dS = \int_0^{h_2} dy \int_0^{h_1} \frac{\partial \phi}{\partial y} \frac{\partial \psi}{\partial x} \, dx$$

$$\simeq \int_0^{h_2} dy \, \frac{\partial \psi}{\partial x} \int_0^{h_1} \frac{\partial \phi}{\partial y} \, dx$$

$$\simeq \frac{1}{2} h_1 \int_0^{h_2} \frac{\partial \psi}{\partial x} \left[\frac{\partial \phi}{\partial y} \Big|_{x=h_1} + \frac{\partial \phi}{\partial y} \Big|_{x=0} \right] dy$$

$$\simeq \frac{1}{2} h_1 \left(\frac{\phi_2 - \phi_1}{h_2} + \frac{\phi_4 - \phi_3}{h_2} \right) \int_0^{h_2} \frac{\partial \psi}{\partial x} \, dy$$

$$\simeq \frac{h_1 h_2}{4} \left(\frac{\phi_4 - \phi_3}{h_2} + \frac{\phi_2 - \phi_1}{h_2} \right) \left(\frac{\psi_4 - \psi_2}{h_1} + \frac{\psi_3 - \psi_1}{h_1} \right) \tag{54}$$

and

$$\int_{S_p} \frac{\partial \phi}{\partial x} \frac{\partial \psi}{\partial y} \, dS \simeq \frac{h_1 h_2}{4} \left(\frac{\psi_4 - \psi_3}{h_2} + \frac{\psi_2 - \psi_1}{h_2} \right) \left(\frac{\phi_4 - \phi_2}{h_1} + \frac{\phi_3 - \phi_1}{h_1} \right)$$

The variational expression J is then obtained as the sum of the contribution of each element S_p : $J = \sum_p S_p$. J is a quadratic expression of the field values ϕ_j, ψ_j at each of the N mesh points. The stationary property of J is utilized by differentiating with respect to each of the 2N variables ϕ_j and ψ_j. In this way a set of 2N linear equations is derived, and they are of the form

$$A \, X = k_A^2 \, B \, X \quad , \tag{55}$$

where A is a symmetric band matrix, B is a diagonal positive definite

matrix and X is an ordered vector of the variables ϕ_j, ψ_j. Detailed

expressions for A and B are given in Appendix B.

By a transformation we can reduce Eq. 55 to a simple eigenvalue

problem

$$A' \ X = k_A^2 \ X \tag{56}$$

with

$$A' = B^{-\frac{1}{2}} \ A \ B^{-\frac{1}{2}} \quad . \tag{57}$$

It is important to note that the matrix A' is also symmetric and banded.

This structure allows us to use a compact storage scheme for the

numerical calculations and efficient algorithms for computing the

eigenvalues and eigenvectors. In the case of the FE-method [12,13], an

equation similar to Eq. 55 is obtained but the matrix B is banded and

therefore the eigenvalue problem is more complicated.

4.5 Properties of FD Approximations

A complete analysis of the truncation error of the method that we just outlined would be very lengthy and rather useless. We will proceed by comparison with other well known numerical solutions. Let's assume that we can consider, for the purpose of our error analysis, a simplified problem that requires only one longitudinal field. The problem is then described by one elliptic partial differential equation:

$$\nabla^2 u + \lambda u = 0 \tag{58}$$

valid at all points inside a domain R. The solution u of Eq. 58 corresponds to the stationary points of

$$J(u) = \int\int_R (u_x^2 + u_y^2 - \lambda u^2) \, dx \, dy \tag{59}$$

where the subscripts x and y denote a partial derivative. The domain R is divided into rectangular subregions S_i. Let $J_1(u)$ be the contribution to J(u) from the subregion S_1 (Fig. 8). Following the procedure outlined in Section 4.4, we use FD approximations to evaluate $J_1(u)$: *

---

*   Capital letters are used for the value of the function u at the nodes.
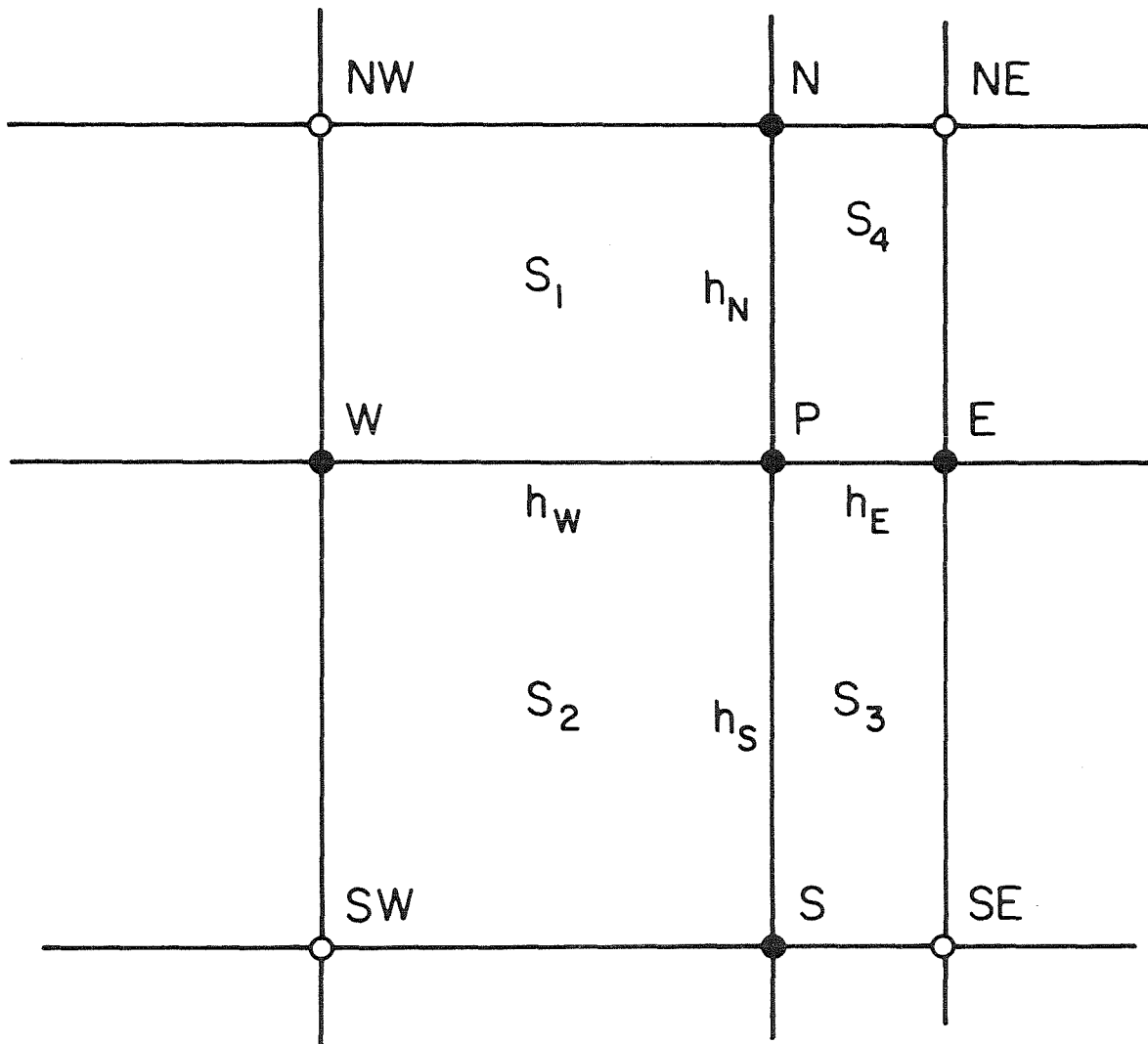
Figure 8. Rectangular mesh. By adding the contributions of the elements S_1, S_2, S_3 and S_4, we obtain that the FD-equations at the node P are equivalent to the equations resulting from the application of the five-point Laplace operator.

$$\iint_{S_1} u^2 \; dx \; dy \simeq \frac{h_N h_W}{4}(U_P^2 + U_N^2 + U_{NW}^2 + U_W^2)$$

(60)

$$\iint_{S_1} u_x^2 \; dx \; dy \simeq \frac{h_W h_N}{2}\left[\left(\frac{U_P - U_W}{h_W}\right)^2 + \left(\frac{U_N - U_{NW}}{h_W}\right)^2\right]$$

$$J_1(u) \simeq \frac{h_N}{4h_W}\left[(U_P - U_W)^2 + (U_N - U_{NW})^2\right] + \frac{h_W}{4h_N}\left[(U_{NW} - U_W)^2 + U_N - U_P)^2\right]$$

$$- \lambda_1 \frac{h_N h_W}{8}(U_P^2 + U_N^2 + U_{NW}^2 + U_W^2) \quad .$$

(61)

To find the difference equation at P we take the partial derivative of $J_1(u)$ with respect to U_P, *

$$\frac{\partial J_1(u)}{\partial U_P} = \frac{h_N}{2h_W}(U_P - U_W) + \frac{h_W}{2h_N}(U_P - U_N) - \lambda_1 \frac{h_N h_W}{4} U_P$$

(62)

and sum the equivalent expressions for subregions S_2, S_3 and S_4. We find that

---

* The subscript "1" indicates that λ can be a function of (x,y).

$$\frac{\partial J(u)}{\partial U_P} = \frac{h_W + h_E}{2h_N} U_N + \frac{h_N + h_S}{2h_W} U_W + \frac{h_W + h_E}{2h_S} U_S + \frac{h_S + h_N}{2h_E} U_E$$

$$- \left[\left(\frac{h_W + h_E}{2h_N} + \frac{h_N + h_S}{2h_W} + \frac{h_W + h_E}{2h_S} + \frac{h_S + h_N}{2h_E} \right) \right.$$

$$\left. - \frac{1}{4}(\lambda_1 h_N h_W + \lambda_2 h_W h_S + \lambda_3 h_S h_E + \lambda_4 h_E h_N) \right] U_P = 0 \quad . \quad (63)$$

When all the h_i's are equal to h (square mesh), Eq. 63 reduces to
the FD equation obtained by application of the usual five-point
Laplace difference operator Δ_h [17,21]:

$$\Delta_h U = \frac{1}{h^2} [U_E + U_N + U_W + U_S - 4 U_P] \quad . \quad (64)$$

The properties of this operator are well known. Following the example
outlined in Ref. 17, we consider the eigenproblem defined by Eq.
58 on the unit square R with u=0 on the boundary. The eigenfunctions
of Eq. 58 are:

$$u_{pq} = \sin(p\pi x) \sin(q\pi y) \qquad p,q=1,2\ldots$$

with the corresponding eigenvalues

$$(65)$$

$$\lambda_{pq} = (p^2 + q^2) \pi^2 \qquad p,q=1,2\ldots$$

On a square grid of size h=1/M, the five-point difference operator gives

$$U_{1-1,m} + U_{1+1,m} + U_{1,m+1} - (U - \Lambda h^2) U_{1m} = 0 \qquad (66)$$

for l,m = 1,...,M-1.

By direct substitution it can be verified that the eigenfunctions are

$$U_{1,m}^{pq} = \sin \frac{p\pi 1}{M} \sin \frac{q\pi m}{M}$$

leading to eigenvalues,

$$\Lambda_{pq} = \frac{2}{h^2}(2-\cos \frac{p\pi}{M} - \cos \frac{q\pi}{M}) \qquad (67)$$

for p,q = 1,...,M-1.

Therefore, whereas the differential equation has an infinite number of eigenvalues, the FD equations provide only $(M-1)^2$. By expanding in a Taylor series the right-hand side of Eq. 67, we obtain

$$\Lambda_{pq} = \lambda_{pq} + O(h^2) \qquad . \qquad (68)$$

In general, the dominant (smallest) eigenvalue is much better approximated than the higher ones.

From this analysis we expect that the error on the eigenvalues

will be of $O(h^2)$ where h would be the largest dimension of a rectangular

element in the case of a graded mesh *. The accuracy of the approximate

eigenfunctions is much more difficult to assess, but it is usually

assumed to be one order of magnitude smaller than the accuracy of

the corresponding eigenvalue, i.e., $O(h)$.

4.6. Solution of the Matrix Eigenvalue Equations

The solution of the matrix eigenvalue equation is sought in the

standard form $A'X = \lambda X$, where A' is a symmetric band matrix. If we

use a mesh of NxN rectangular elements (Fig. 6), then the order of A

is $2(N-1)^2$ and the bandwidth (the number of subdiagonals including

the main diagonal) is 2N. For a typical calculation, N=15 and thus

the order equals 392 and the bandwidth equals 30.

The numerical algorithms chosen were specifically designed for

a symmetric band-matrix: The storage requirements are minimized by

storing only the non-trivial elements. The routines are part of the

well known EISPACK package [22]; they proceed as follows:

---

* This property was verified in the course of our numerical calculations
  by comparing the eigenvalues corresponding to successively refined
  grids, all other parameters remaining unchanged.

a) A' is reduced to tridiagonal by a series of Givens rotations that eliminate successively each subdiagonal while maintaining the band form (routine BANDR) [22,23].

b) The eigenvalues in an interval of interest, that is the negative eigenvalues that are closest to zero, are determined by the routine BISECT [22,24]. The number of eigenvalues in the given interval is computed from Sturm sequences. Next, the eigenvalues are evaluated by refining the input interval by a bisection process.

c) The eigenvectors are computed by inverse iteration (routine BANDV) [22,25]. The system (A' - I) X = b is solved by Gaussian elimination: The right-hand side vector b is chosen so as to obtain a proper eigenvector.

It is important to note that by these methods it is impossible to omit any eigenvalue: This is a very desirable feature in comparison with iterative methods.

If the finite-elements formulation had been used, the resulting eigenproblem, A' X = λBX, would involve two banded matrices. The minimum storage requirements are doubled and the numerical methods available are all iterative. [12,13,26]

4.7. Mode Designation

All the possible modes of the rectangular guide may be divided

into four classes depending on the symmetry of the longitudinal

fields, since a longitudinal field H_z of even symmetry with respect to

one particular axis is always associated with a longitudinal field

E_z of odd symmetry with respect to the same coordinate. These four

classes are designated in this work: HE_n^{oe}, HE_n^{eo}, HE_n^{oo}, HE_n^{ee}. The

first superscript, o or e, indicates the symmetry of H_z with respect

to the x-axis, while the second superscript denotes the symmetry of

H_z with respect to the y-axis. The subscript n indicates the order

of the given mode in its class.

4.8. Numerical Results and Comparison with Other Work

Using the FD method described above we wrote a computer program

that builds the matrices A and B for a guiding structure of given

geometry and permittivity and a given mesh (see Appendix B). In

addition to these parameters, we need to provide a value of β/k_o

(in the range $\sqrt{K_2}$, $\sqrt{K_1}$ for a guided mode), which in turn determines

$\tau = k_2^2/k_1^2$. Then the program computes the dominant eigenvalues, k_2^2,

that is, the negative eigenvalues closest to zero. For each of these

eigenvalues, the corresponding value of the free-space wave number, k_o,

is determined. If a mode characteristic is desired, this computation

is repeated for a set of values of τ. To obtain field plots, the

program computes the eigenvectors corresponding to the first few eigenvalues.

The dispersion curves are presented in the B,V description commonly used for optical waveguides (see Part I):

V is the normalized frequency defined by

$$V = k_o a \sqrt{K_1 - K_2} \tag{69}$$

for a waveguide, of dimensions axb, and B is the normalized phase parameter

$$B = \frac{(\beta/k_o)^2 - K_2}{K_1 - K_2} \quad . \tag{70}$$

To verify numerically the accuracy of our FD approach, we shall compare our results with those obtained according to other methods. Specifically we shall consider the comparison with:

1) the exact solution of a circular guide;

2) the approximate solution proposed by Marcatili, in the case of a square guide;

3) the mode matching solution.

We will then present a complete set of dispersion curves for square dielectric guide of permittivity 2.1 (Teflon) and 13.1 (GaAs) and also some field plots.

4.8.1 Round Guide

A comparison with the round guide is particularly indicated because
the exact solution is known. We defined the permittivity of the elements
of a square mesh in such a way that they approximate one quadrant of a
circular fiber. In Fig. 9, the hatched squares are assigned a permittivity
K_1 while the other elements correspond to K_2. The exact dispersion
curve for the dominant HE_{11}-mode is presented in Fig. 10 along with
the FD approximations: The total number of elements is N^2 while
the parameter M defines the number of elements in the circular section
(see Fig. 9). If M is chosen too small, the round guide is poorly
approximated. For N = 15 and M = 10, the FD calculations are in very
close agreement with the theoretical curve, far above cutoff, where
the mode is well confined. For smaller values of V, the fields
extend further out and the mode is influenced by the outer box
(metallic walls): To obtain the dispersion curve in this frequency
region we need to increase the ratio N/M. It is important to note
that for N = 15, the CPU time required on an IBM 3032 to compute the
first five eigenvalues corresponding to one value of τ, or
equivalently, one value of B, is about 1.4 minutes. For N = 20, this
time increases to approximately 4 minutes.
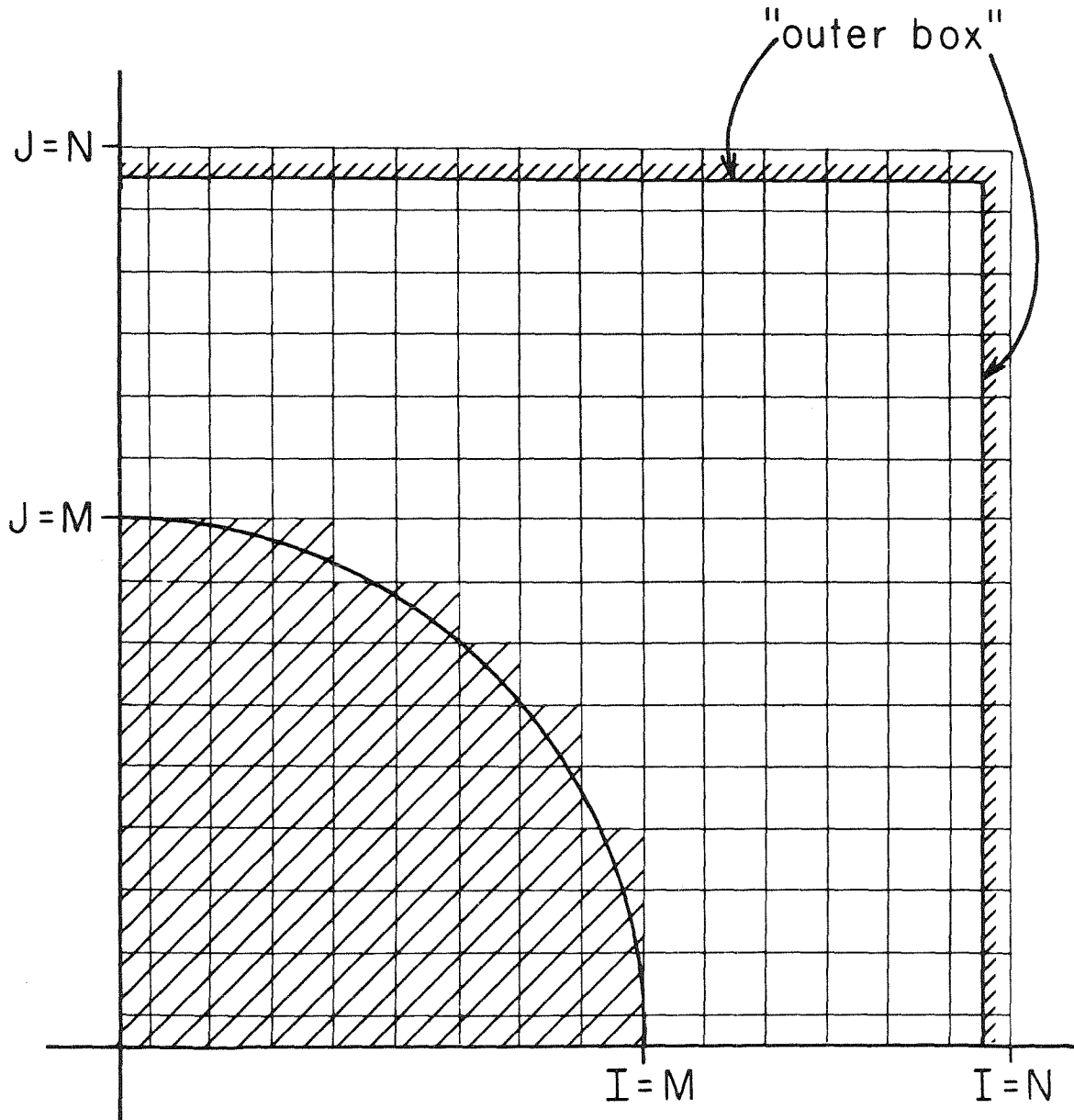
Figure 9. Approximations of a round guide by use of a square mesh. The hatched elements are assigned a dielectric constant K_1, while the remaining ones correspond to K_2 ($<K_1$).
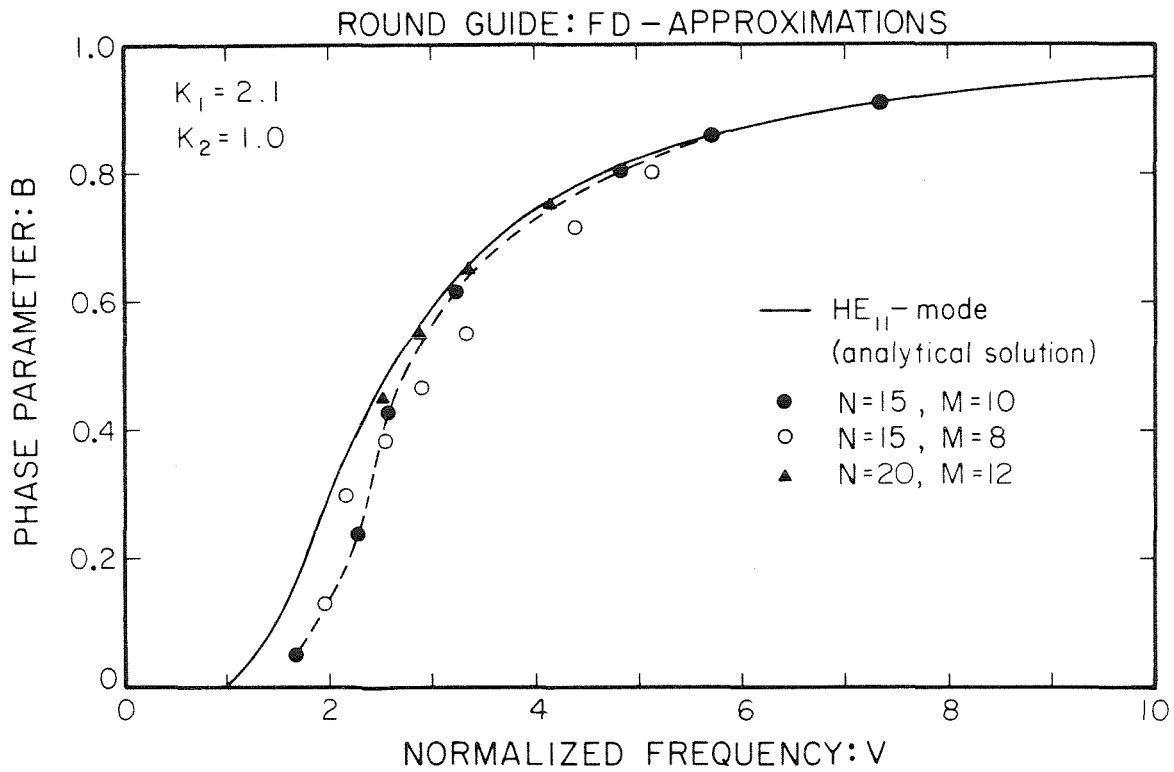
Figure 10. Dispersion characteristics for the dominant mode of a round waveguide: The continuous line corresponds to the exact theoretical solution for the HE_{11}-mode while the dashed line is obtained from the FD-approximations.

4.8.2. <u>Marcatili's Approximation of a Square Guide: Discussion</u>

In Figs. 11 and 12 we have plotted the dispersion curves,
respectively, for a square guide of permittivity $K_1 = 2.1$ and for a
square guide of $K_1 = 13.1$, the dispersion curves obtained by using:

(i)   Marcatili's closed-form solution (Eqs. 22-29);

(ii)   the exact solution of the HE_{11}-mode of a round fiber

       that has the same area as the square guide:

(iii) the FD method: N^2 is the total number of elements and M^2

       is the number of elements defining the dielectric guide.

At high frequency, $V \gg 1$, most of the field energy lies inside
the guide and the dispersion curves computed by (i) and (ii) cannot
be distinguished. This gives use a very good check on the accuracy
of our FD calculations: They agree very well. Because the fields
are well confined, the metallic walls can be relatively close to the
guide. For small values of V, we know that Marcatili's solution is
not correct: it predicts erroneously a cutoff frequency. In this
region, the fields are loosely confined, and we expect that the dis-
persion curve of the square guide will be very similar to the curve of
the round guide. This is confirmed by our FD calculations. In
this frequency range, we needed to remove the metallic walls
further from the guide, i.e., increase the ration N/M. However, as for
the dominant mode the fields are expected to vary slowly inside the
guide, we can achieve the increase in N/M by decreasing M. When the
ratio N/M is too small for the frequency range studied, the dispersion
curve appears to drop more rapidly than it actually does.
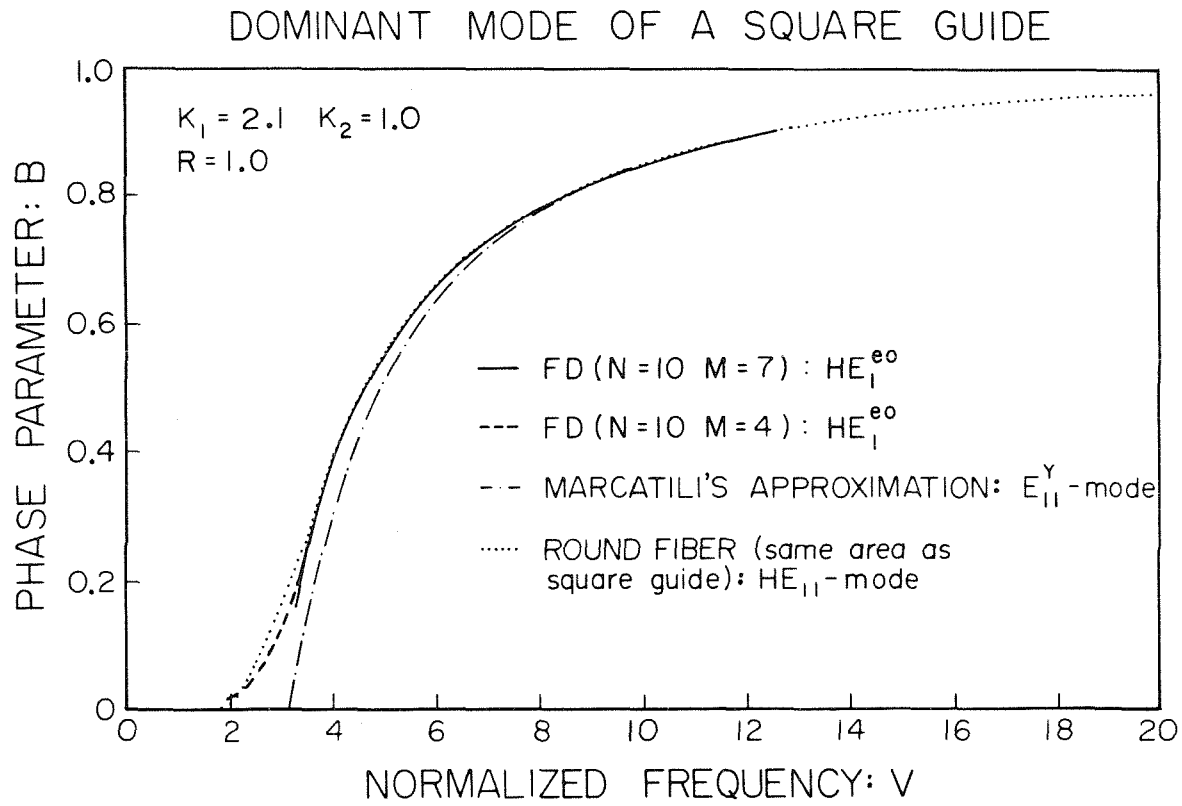
DOMINANT MODE OF A SQUARE GUIDE

Figure 11. Comparison between various solutions for the dominant mode
of a square dielectric guide. For obtaining an accurate FD-solution at
low frequencies, it is necessary to use a higher ratio N/M. The
solution for a round fiber of equivalent cross-sectional area is shown
for comparison.
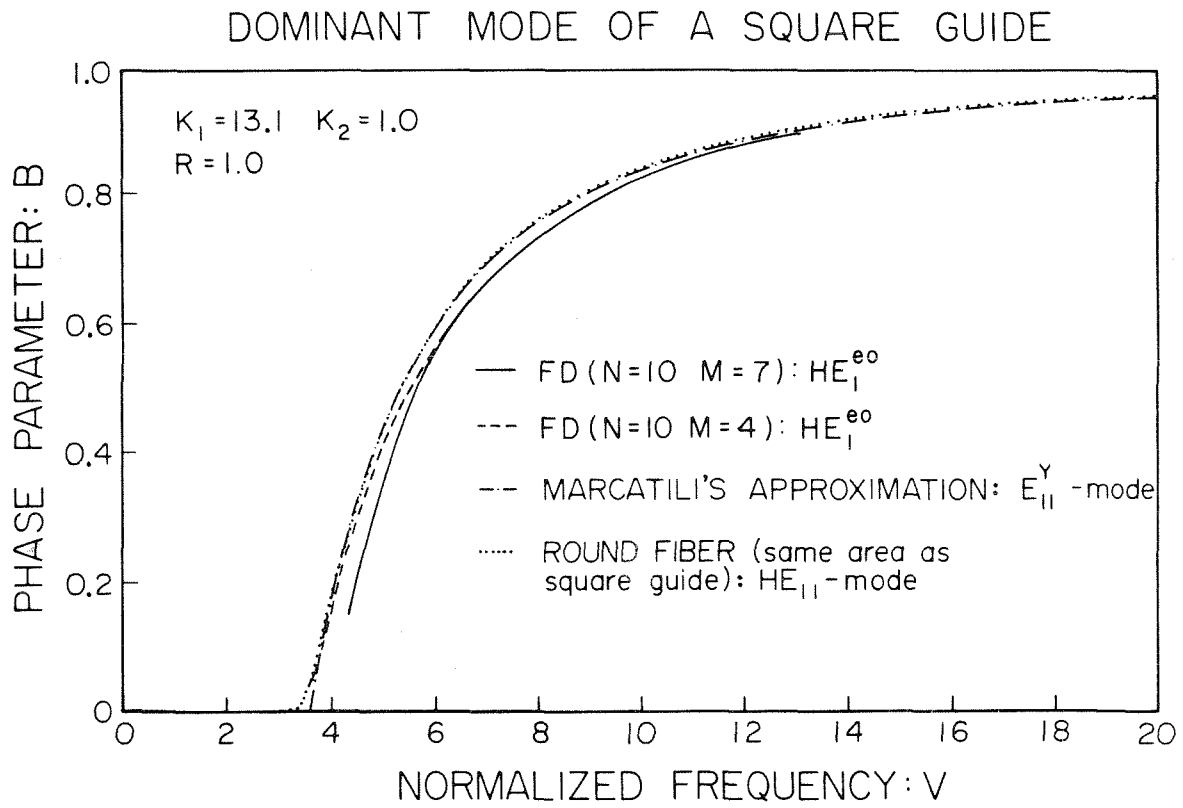
Figure 12. Comparison between various solutions for the dominant mode
of a high-permittivity square dielectric guide. The solution for a
round fiber of equivalent cross-sectional area is shown for comparison.

4.8.3. Mode-Matching

As described in Section 3.2, mode matching has been used to compute the modes of high-permittivity image lines [11]. We compared the dispersion characteristics obtained by this method to our FD calculations in Figs. 13 and 14. The mode designation used by Solbach [11] is identical to the one adopted by Marcatili. After determining the symmetry properties of these modes, we computed by FD the modes belonging to the same class of symmetry. For a permittivity of 2.22 (Fig. 13) the two techniques do not agree very well for the first mode but are in closer agreement, particularly at higher values of V, for the second mode. For $K_1=12.0$ the agreement between the two methods is excellent for the lowest mode.

4.8.4. Dispersion Curves for $K_1=2.1$ and $K_1=13.1$: Higher Order Modes

For each class of modes (see Section 4.7) we computed the dispersion characteristics for two values of the permittivity: $K_1 = 2.1$ (Fig. 15) and $K_1 = 13.1$ (Fig. 16). It was necessary to make plots of the corresponding eigenvectors in order to reject the spurious modes that we shall describe in Section 4.9.

The dispersion curves are presented in comparison with the curves corresponding to Marcatili's modes that have the same axis-symmetries. Because the waveguide that we are studying is square, the E^y_{pq} and E^x_{pq}-modes are degenerate. In the case of the FD modes, the He^{eo}_n-modes are degenerate with the HE^{oe}_n-modes.
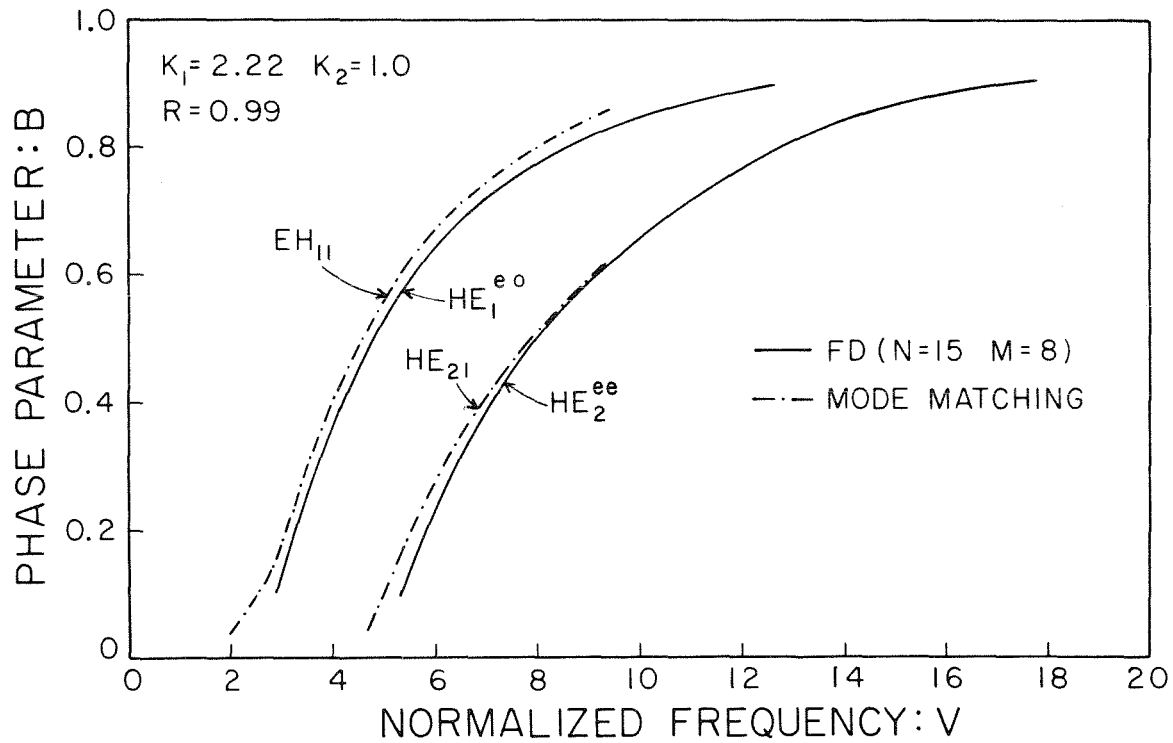
Figure 13. Comparison between the FD- and the mode-matching solutions.
The mode denomination for the mode matching solution is the same as
Marcatili's. The mode denomination for the FD-calculations is derived
from the symmetry properties of the longitudinal magnetic field with
respect to the x- and y-axes, as explained in Section 4-7.
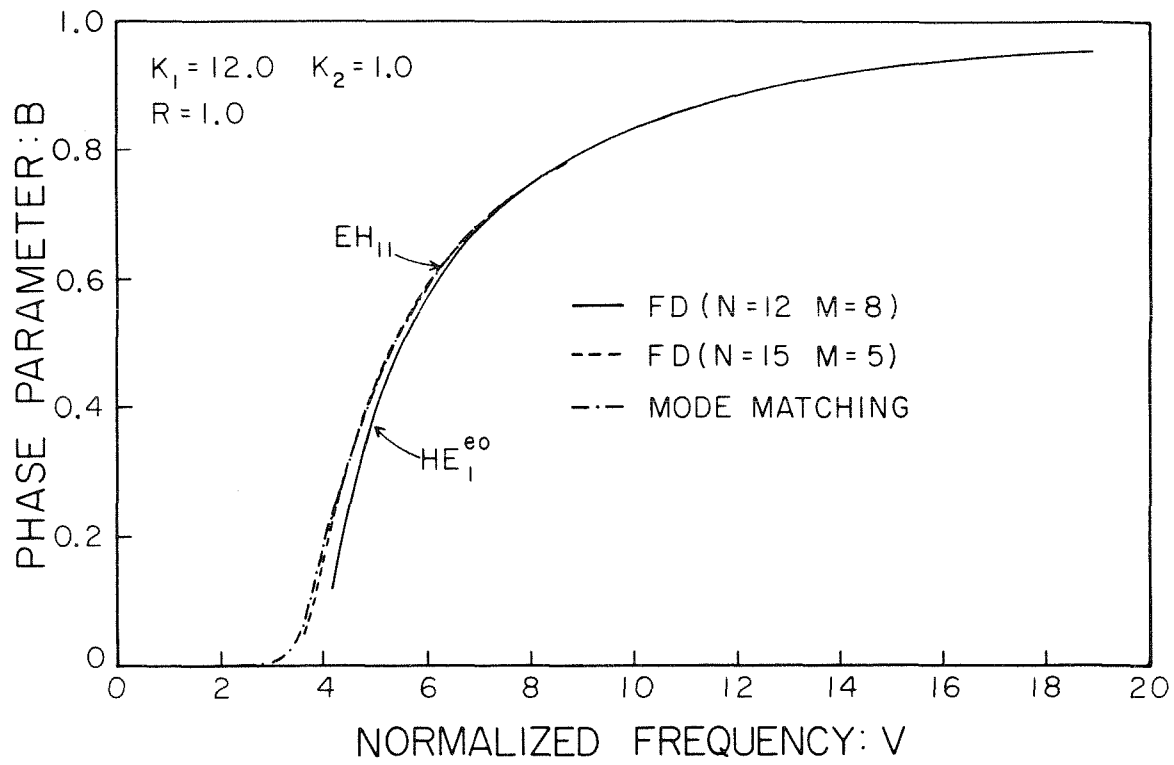
Figure 14. Comparison between the FD- and the mode-matching solutions.

In Figs. 15 and 16 we observe that only the dominant E_{11}^y-mode agrees with our FD computations: The disagreement is progressively worse as we consider the higher order modes. We recall that the propagation constants are the stationary values of a functional (Eq. 49). Therefore, for the dominant mode, the guess of the eigenfunctions that is inherent in Marcatili's assumptions still leads to very good values for the propagation parameter. We note that the degeneracy of the E_{21}^y and E_{12}^y-modes is not confirmed by our FD-calculations. Corresponding to each of these modes, we obtain two modes, HE_n^{ee} and HE_n^{ee} (with n equal to 1 and 2, respectively,) that become degenerate only for very large values of V. This is because, for a very tightly confined mode, the fields corresponding to these two modes are not much influenced by the outer dielectric interface and the fields can be superimposed by a 45° rotation.

Until now we have presented results mostly for the square guide. This is because we expect that Marcatili's solutions become a better approximation as the guide aspect ratio $R = a/b$ increases. This is confirmed by Fig. 17 that indicates that already for $R = 5$ we cannot distinguish the FD solution from Marcatili's.

4.8.5. Field Plots

We have now established that Marcatili's solutions are a relatively good approximation for computing the propagation constant of the dominant mode of rectangular dielectric guides, and they are attractive
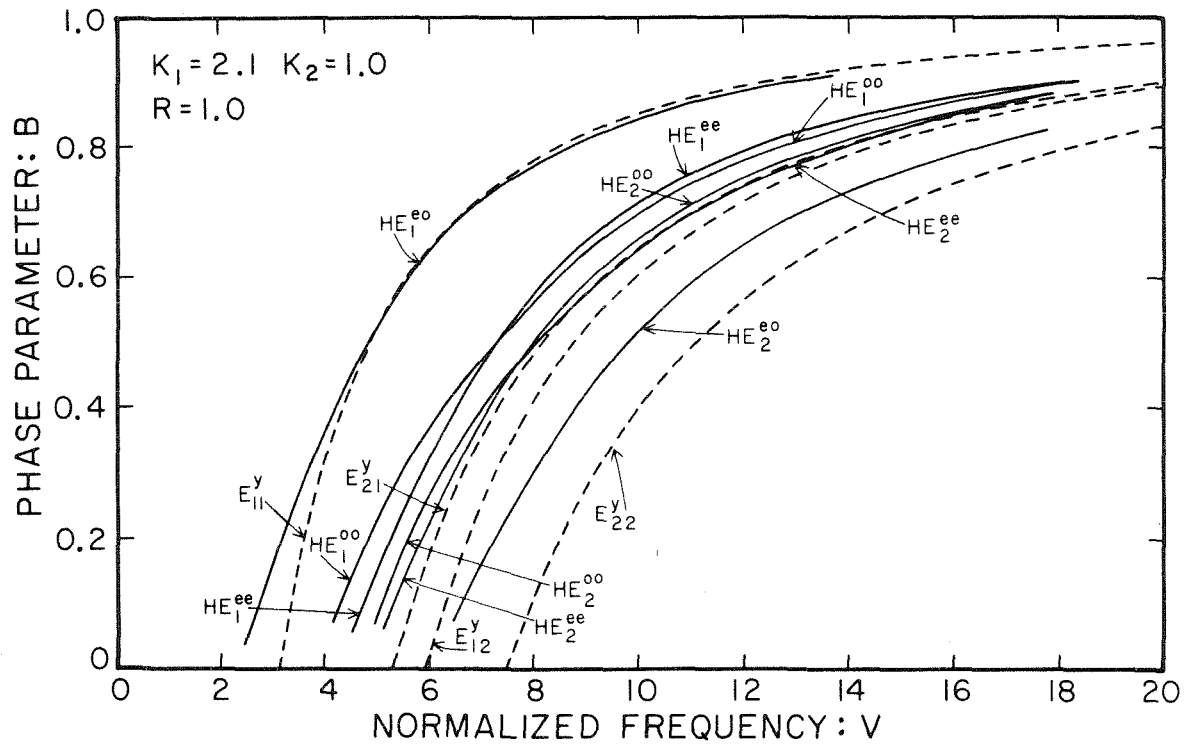
Figure 15. Dispersion curves for a square guide. The continuous lines correspond to the FD-solutions while the dashed lines are Marcatili's.
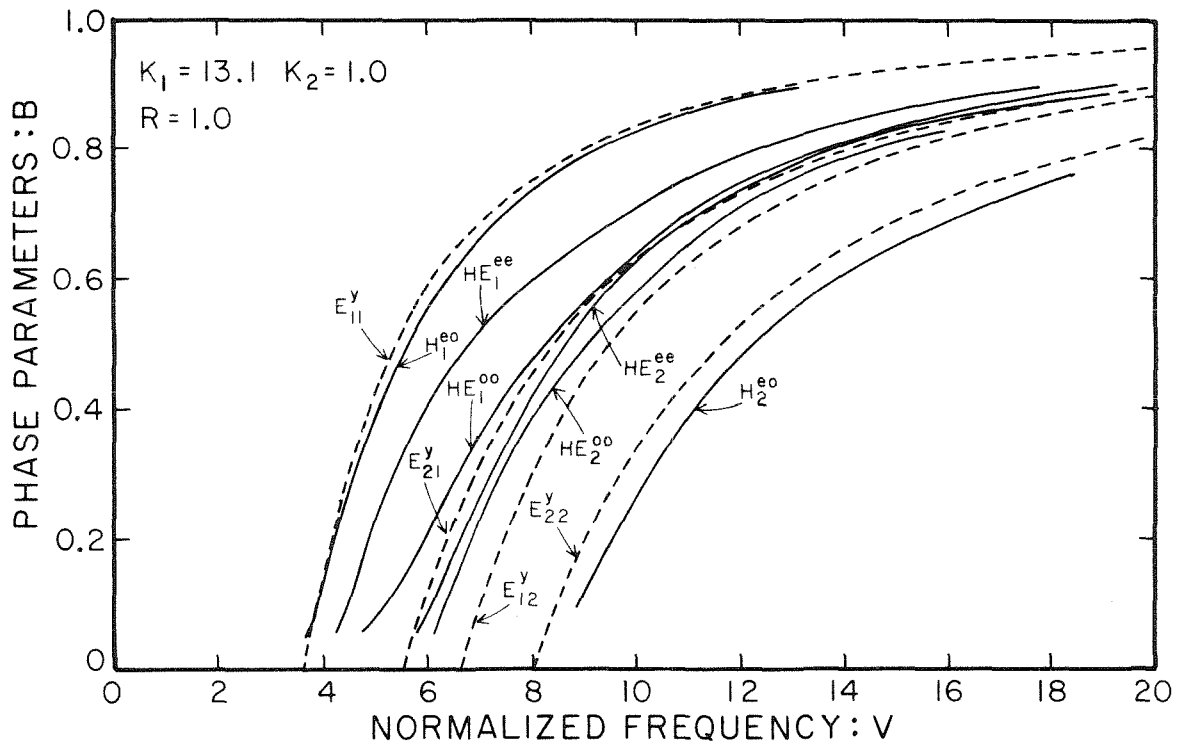
Figure 16. Dispersion curve for a square guide: The continuous lines are the FD-solutions and the dashed lines are Marcatili's.

Dominant Mode of a Rectangular Guide
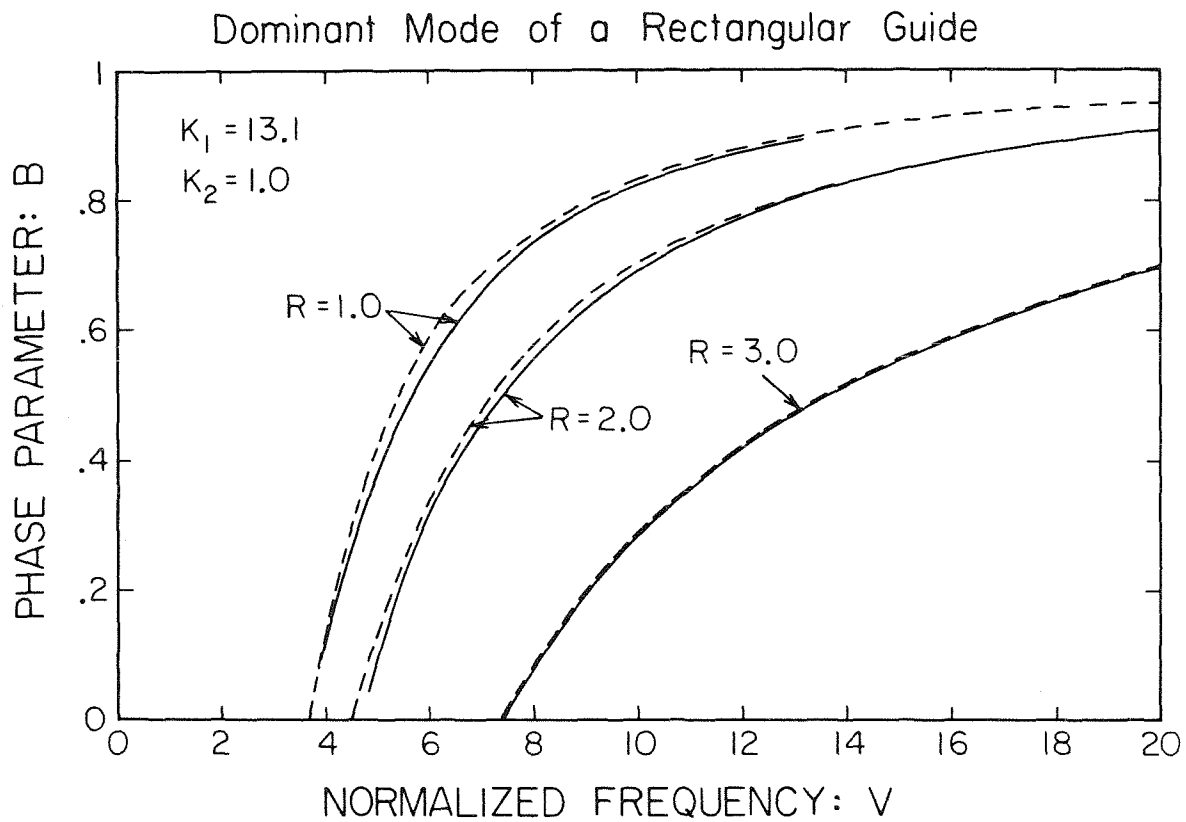
Figure 17. Dispersion curves for rectangular high-permittivity wave-guides. As the index ratio is increased, Marcatili's solution (dashed lines) becomes a better approximation, as verified by our FD-calculations (continuous lines).

because the solution can be written in a simple closed form.
We shall now compare the field behavior of the dominant mode as computed by both methods.

In Fig. 18 we plotted the longitudinal electric and magnetic fields of the E^x_{pq}-mode, as they vary in the x,y-plane, respectively, along a line x=1/h and y=1/h: The guide is a square guide of permittivity $K_1=2.1$. The discrete points are the field values at the node points for the corresponding HE^{oe}-mode. In Fig. 19 we compare the E^y_{pq}-mode with the FD equivalent, the HE^{eo}-mode, for a square guide of permittivity $K_1=13.1$. In each case the fields have been separately normalized so that $\left|H_z\right|_{max} = 1$ and $\left|E_z\right|_{max} = 1$. This allows us to compare only the spatial behavior. The relative importance of the fields is obtained by considering, for both methods, the value of the parameter ρ [defined in Section 2]. These quantities are listed in Table II. For both values of the permittivity, the qualitative behavior predicted by Marcatili's approximation is observed. The fields behave sinusoidally inside the waveguide and decay exponentially away from the surface. However, our FD calculations show that the fields are actually more tightly confined. In the case of the low permittivity guide $(K_1=2.1)$ the dominance of the E_z- over the H_z-field is underestimated by about 80%; for the higher index guide the parameter ρ is overestimated by 25%. There does not appear to be a clear trend in the comparison of the values of ρ, computed by the two method. This is further complicated by the fact that ρ, for a given mode, will vary as the mode goes from cutoff to far above
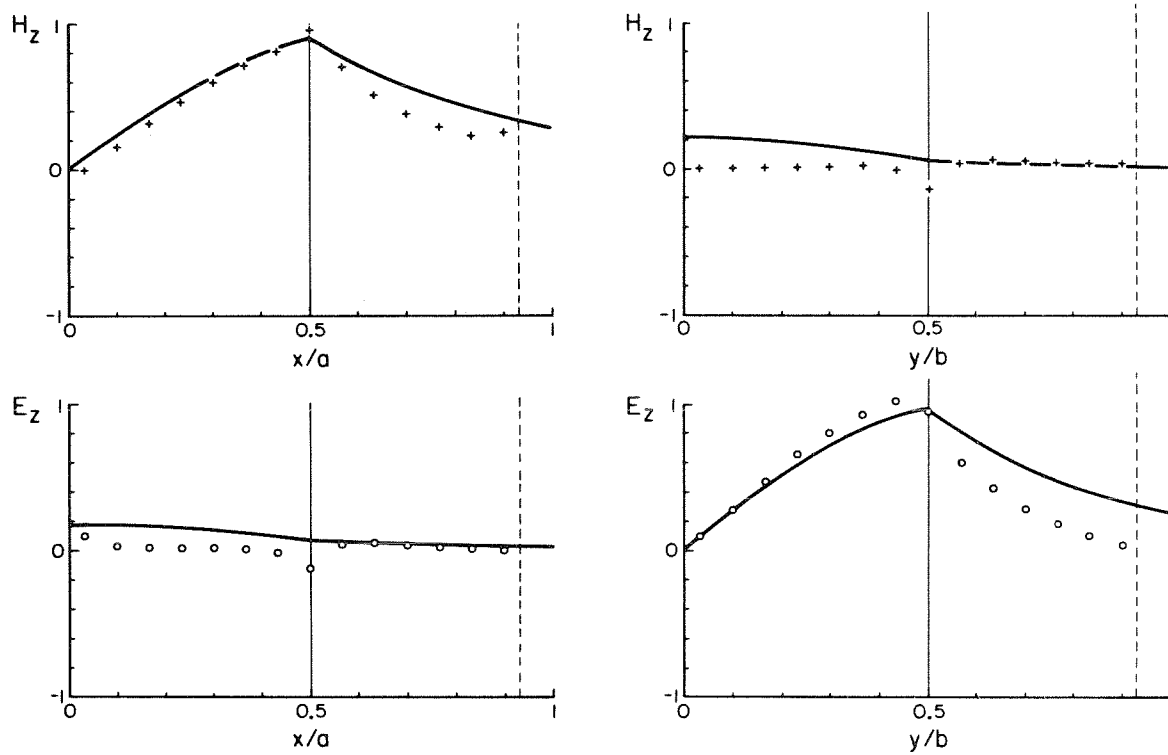
Figure 18. Plots of the longitudinal fields of the dominant mode of a square dielectric guide of permittivity K_1=2.1 (K_2=1.0). The continuous lines are the fields computed by using Marcatili's solution while the discrete points are obtained by the FD-calculations. The values of V and B are indicated in Table II. The fields are plotted respectively along lines y = 1/h and x = 1/h, where h is the size of the square elements used in the FD-calculations. The position of the guide corresponds to: $-0.5 \leqslant \frac{x}{a}$, $\frac{y}{b} \leqslant 0.5$. The thin dashed line indicates the position of the outer "box".
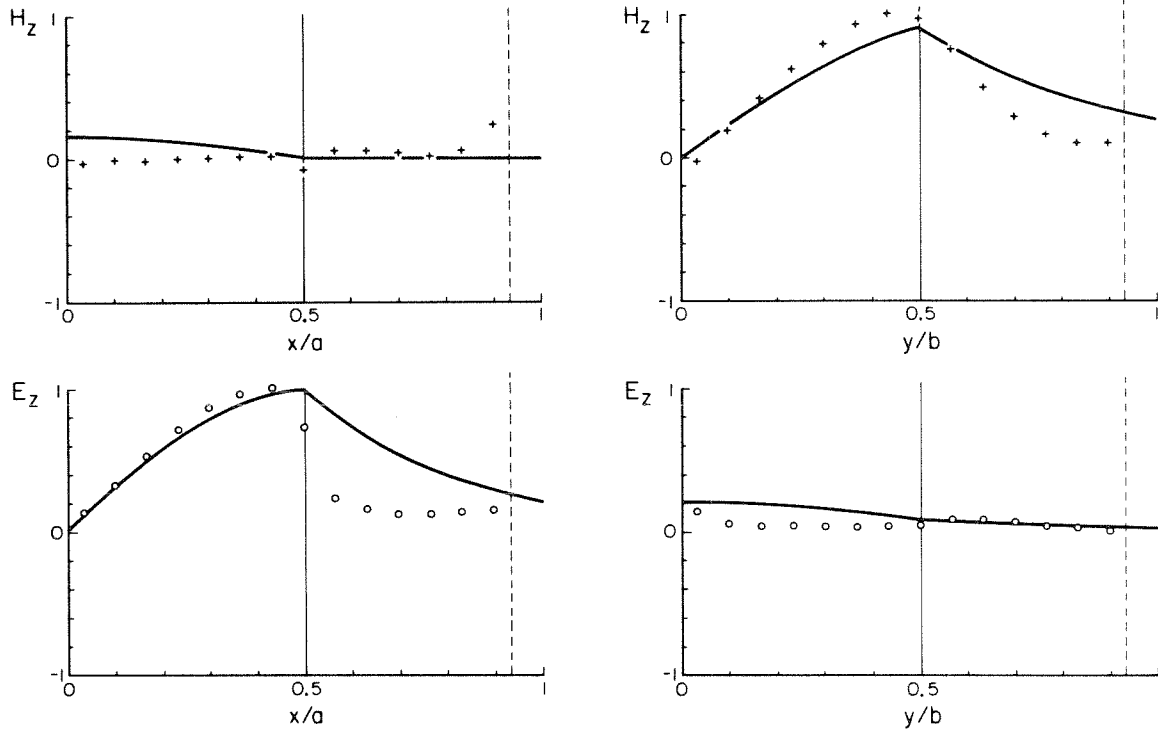
Figure 19. Plots of the longitudinal fields of the dominant mode of a square dielectric guide of permittivity K_1=13.1 (K_2=1.0). The continuous lines are the fields computed by using Marcatili's solution while the discrete points are obtained by the FD-calculations. The values of V and B are indicated in Table II. The fields are plotted respectively along lines y = 1/h and x = 1/h, where h is the size of the square elements used in the FD-calculations. The position of the guide corresponds to: $-0.5 \leqslant \frac{x}{a}$, $\frac{y}{b} \leqslant 0.5$. The thin dashed line indicates the position of the outer "box".

TABLE II

Comparison between Marcatili's and FD[*] solution for the dominant mode
of a square dielectric guide

	Mode	V	B	ρ
$K_1 = 2.1$ $K_2 = 1.0$	E_{11}^y	5.44	0.58	0.91
	HE_1^{eo}	5.44	0.60	1.65
$K_1 = 13.1$ $K_2 = 1.0$	E_{11}^x	6.26	0.62	16.9
	HE_1^{oe}	6.26	0.60	13.5

[*] N = 15   M = 8

cutoff. For the high-permittivity guide the closer correspondence in ρ may be explained by the fact that this guide is further above cutoff than the lower permittivity one.

4.9. Spurious Modes

As explained in Section 4.6, the dispersion characteristics are obtained by scanning a range of values for the normalized phase parameter B and computing the corresponding values of the normalized frequency V, for a given class of modes. The computer then generates a plot such as the one illustrated in Fig. 20. The open circles correspond each to an eigenvalue. By taking a sufficient number of values for B it is possible to connect the results by smooth curves. However, this cannot be done uniquely, as shown by the two sets of lines in Fig. 20. The continuous lines correspond to the dispersion characteristics we have shown, for example, in Figs. 11,15. The interrupted lines do not seem to correspond to physical modes. This is verified by plotting the fields for the various modes. The "non-physical" modes will not exhibit the simple sinusoidal/exponential behavior. Such spurious modes have also been reported by Corr and Davies[20] and Ikeuchi, et al[27]. These modes appear only for values of $(\beta/k_o)^2$ in the range

$$K_1/K_2 < (\beta/k_o)^2 < \frac{K_1 + K_2}{2K_2} \qquad .$$
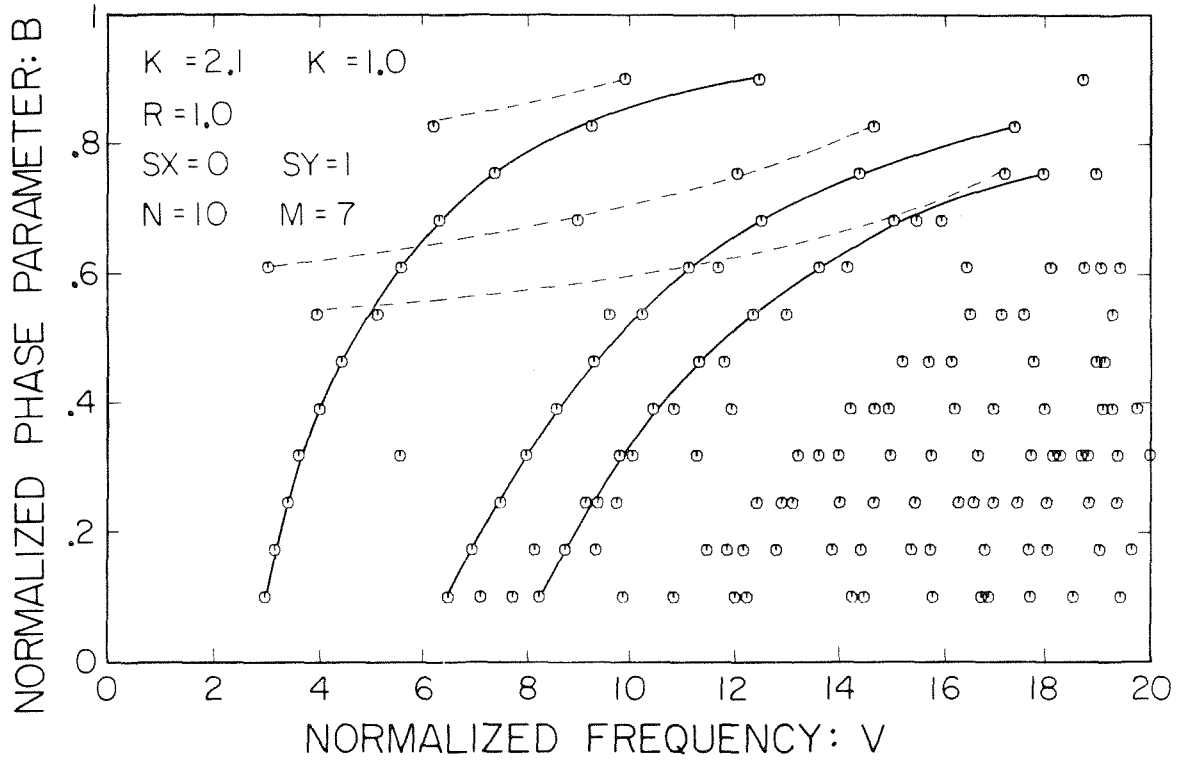
Figure 20. Typical plot of the eigenvalues obtained by FD-calculations.
The continuous lines correspond to propagating modes while the dashed
lines correspond to spurious solutions. They are found to exist only in
the range: 0.5 < B < 1.0 .

For $K_1 \gg 1$, this means that the spurious modes are restricted to the range

$$0.5 < B < 1$$

which we observe on Fig. 20. The cause of these solutions may be in the indefinite nature of the variational formulation of the problem. We recall that we are computing the eigenvalues k_2^2 corresponding to a given (negative) value of $\tau = \dfrac{k_2^2}{k_1^2}$. For propagating modes, both k_1 and k_2 are real quantities: $k_1 > 0$ and $k_2 < 0$. A negative value of τ can also be obtained if k_1^2 were negative and k_2^2 positive. This would be the case for transient modes, that is modes that have an imaginary value for both the propagation constant β and the free-space wavenumber k_o.

5. Conclusions

We have developed a numerical method based on finite-difference (FD) for computing the propagation constants and fields of a dielectric guiding structure.

The method was tested in the case of a round guide for which a rigorous analytical solution exists and also by comparison with other work. The FD method gives very good agreement, by using relatively small meshes. It also is more efficient than the finite-elements method (FE) in terms of computer storage (this would allow us to treat larger meshes, being limited only by CPU time) and also in terms of the numerical method available for computing the eigenvalues of the resulting linear eigenproblem.

We have compared our solutions to Marcatili's approximate one, in the case of square guides that have a permittivity much larger than the surrounding medium. We found that Marcatili's solution gives a very good estimate, but only for the dominant mode. However, because most dielectric waveguides are used in a single-mode configuration, this does not diminish the usefulness of Marcatili's closed-form solution which remains useful for design purposes.

Devices that depend critically on the details of the external field (such as directional couples) may require the FD-calculations.

Finally, our method can be applied to guiding structures of arbitrary shapes and dielectric profiles.

Part II. Bibliography

1. R. M. Knox and P. P. Toulios, "Integrated Circuits for the Milli-
meter through Optical Frequency Range", Proc. of the Symp. Sub-
millimeter Waves, New York, March 1970, pp. 497-516,

2. E. M. Knox, "Dielectric Waveguides Microwave Integrated Circuits -
An Overview, IEEE Trans. Microwave Th. Tech., Vol. MTT-24, Nov.
1976, pp. 806-814.

3. E. A. J. Marcatili, "Dielectric Rectangular Waveguides and
Directional Coupler for Integrated Optics", Bell Syst. Tech. J.,
Vol. 48, Sept. 1969, pp. 2079-2132,

4. J. E. Goell, "A Circular-Harmonic Computer Analysis of Rectangular
Dielectric Waveguides", Bell. Syst. Tech. J., Vol. 48, Sept. 1969,
pp. 2133-2160.

5. J. A. Paul and Y. W. Chang, "Millimeter-Wave Image-Guide Integrated
Passive Devices", IEEE Trans. Microwave Th. Tech., Vol. MTT-26,
Oct. 1978, pp. 751-754.

6. H. Jacobs and M. M. Chrepta, "Electronic Phase Shifter for Milli-
meter-Wave Propagation in Dielectric Waveguides", IEEE Trans. Micro-
wave Th. Tech., Vol. MIT-22, Apr. 1974, pp. 411-417.

7. C. H. Lee, P. S. Mak and A. P. DeFonzo, "Optical Control of Milli-
meter-wave Propagation in Dielectric Waveguides", IEEE J. Quant.
Electr., Vol. JQE-16, March 1980, pp. 277-288,

8. K. L. Klohn, R. E. Horn, H. Jacobs, and E. Freibergs, "Silicon

Waveguide Frequency Scanning Linear Array Antenna", IEEE Trans.
Microwave Th. Tech., Vol. MTT-26, Oct, 1978, pp. 764-773.

9. T. Itanami and S. Shindo, "Channel-Dropping Filter for Milli-
meter-wave Integrated Circuits, IEEE Trans, Microwave Th. Tech.,
Vol. MTT-26, Oct. 1978, pp. 759-764.

10. W. Schlosser and H.-G. Unger, "Partially-Filled Waveguides and
Surface Waveguides of Rectangular Cross Section", in "Advances
of Microwaves", Vol. 1, Academic Press, New York, 1966, pp.
319-387.

11. Klaus Solbach and Ingo Wolff, "The Electromagnetic Field and Phase
Constants of Dielectric Image Lines", IEEE Trans. Microwave Th.
Tech., Vol. MTT-26, April 1978, pp. 266-274.

12. C. Yeh, S. B. Dong and W. Oliver,"Arbitrarily Shaped Inhomogeneous
Optical Fiber or Integrated Optical Waveguides", J. Appl. Phys.
Vol. 46, May 1975, pp. 2125-2129.

13. C. Yeh, S. B. Dong and W. P. Brown, "Single-Mode Optical Waveguides",
Appl. Opt., Vol. 18, May 1979, pp. 1490-1504.

14. H.-G. Unger, Planar Optical Waveguides and Fibers , Clarendon
Press, Oxford 1977.

15. O. C. Zienkiewicz, The Finite Element Method , McGraw-Hill, London,
3rd Edition, 1977.

16. E. Butkov, "Mathematical Physics", Addison-Wesley, Reading, MA, 1968.

17. A. R. Mitchell and D. F. Griffiths, The Finite Difference Method
in Partial Differential Equations , Wiley, New York 1980.

18. S. Ahmed and P. Daly, "Finite-Elements Method for Inhomogeneous Waveguides", Proc. IEEE, Vol. 116, Oct. 1969, pp. 1661-1664.

19. A. D. Berk, "Variational Principle for Electromagnetic Resonators and Waveguides", IRE Trans. Ant. Prop., Vol. AP-4, April 1956, pp. 104-111.

20. Douglas G. Corr and J. Brian Davies, "Computer Analysis of the Fundamental and Coupled Microstrip", IEEE Trans. Microwave Th. Tech., Vol. MTT-20, Oct. 1972, pp. 669-678.

21. G. E. Forsythe and W. R. Wasow, "Finite-Difference Methods for Partial Difference Equations", Wiley, New York, 1960.

22. B. S. Garbow, J. M. Boyle, J. J. Dougarra, C. B.Moler, Matrix Eigen-system Routines - EISPACK Guide Extension , in Lecture Notes in Computer Science , Vol. 51, Springer-Verlag, Heidelberg, 1977.

23. H. R. Schwartz, "Tridiagonalization of a Symmetric Band Matrix", Numerische Mathematik, Vol. 12, 1968, pp. 231-241.

24. W. Barth, R. S. Martin and J. H. Wilkinson, "Calculation of the Eigenvalues of a Symmetric Tridiagonal Matrix by the Method of Bisection", Numerische Mathematik, Vol. 9, 1967, pp. 336-393.

25. J. H. Wilkinson, "Calculation of the Eigenvectors of a Symmetric Tridiagonal Matrix by Inverse Iteration", Numerische Mathematik, Vol. 4, 1962, pp. 368-376.

26. G. Peters and W. H. Wilkinson, "Eigenvalues of $Ax = \lambda Bx$ with Band Symmetric A and B", Comput. J., 1969, pp. 398-404.

27. Masatoshi Ikeuchi, Hideo Sawami and Hiroshi Niki, "Analyses of
Open-type Dielectric Waveguides by the Finite-Element Iterative
Method", IEEE Trans. Microwave Th. Tech., Vol. MIT-29, March 1981,
pp. 234-239.

Part III. Measurement of Complex Permittivity at Millimiter Wave
          Frequency

1. Introduction

This section describes a series of experiments made to determine the
complex permittivity of KRS-5 and KRS-6 at 94 GHz. The mixed crystal
thallium bromide-iodide (KRS-5) has been known as an infrared window
material for the wavelength range 0.6-40 µm. Nothing was known of its
properties in the millimeter wave range. Von Hippel[1] reports a low-
frequency dielectric constant of 32 and a loss tangent of 2×10^{-3} at 10
GHz. The low-frequency losses of thallium bromide-chloride (KRS-6),
as given by von Hippel[1], are also quite low. Therefore, we proceeded
to measure the dielectric properties of these materials at 94 GHz.

In selecting the experimental procedure, an important consideration
was the ability to use standard millimeter-wave test equipment. Past work
at these frequencies made use primarily of quasi-optical methods: open
resonator, interferometer, "free-space path". Our measurement
techniques utilize samples mounted in standard metal waveguides. They
are based on a novel sample mounting configuration[2] that eliminates gaps
between the sample and the waveguide walls. Waveguide methods offer the
advantage of simplicity and accurate positioning of the dielectric
material.

2. Survey of Available Experimental Methods

2.1 Quasi-Optical Techniques

These methods are based on the interaction of a plane-polarized wave with a dielectric slab positioned in free-space. They can be divided into two categories:

- free space path;

- open resonator.

2.1.1 Free-Space Path

These techniques involve a dielectric sample in the form of a relatively large dielectric slab positioned between two horns (see Fig. 1): a transmitting and a receiving horn. The rest of the apparatus is either a strictly free-space system or a microwave bridge.

When using a free-space system [3,4], the real part of the complex permittivity is determined from the measurement of the Brewster's angle, and the loss tangent is obtained by comparing the transmitting power before and after insertion of the sample in the path. When the thickness of the dielectric sample is equal to or greater than half a material wavelength, $\lambda_m/2^*$, it is necessary to take into account the effect of multiple reflections within the slab.

A microwave bridge can be used to determine the dielectric constant by measuring the phase shift resulting from the presence of the sample. The losses are then also obtained by a comparison of the transmitted power with the incident power. [3,5] The microwave bridge offers the

---

* Material wavelength: $\lambda_m = \dfrac{\lambda_o}{\sqrt{K}}$. For KRS-5 (K=32) at 94 GHz $\lambda_m = 0.56$ mm.
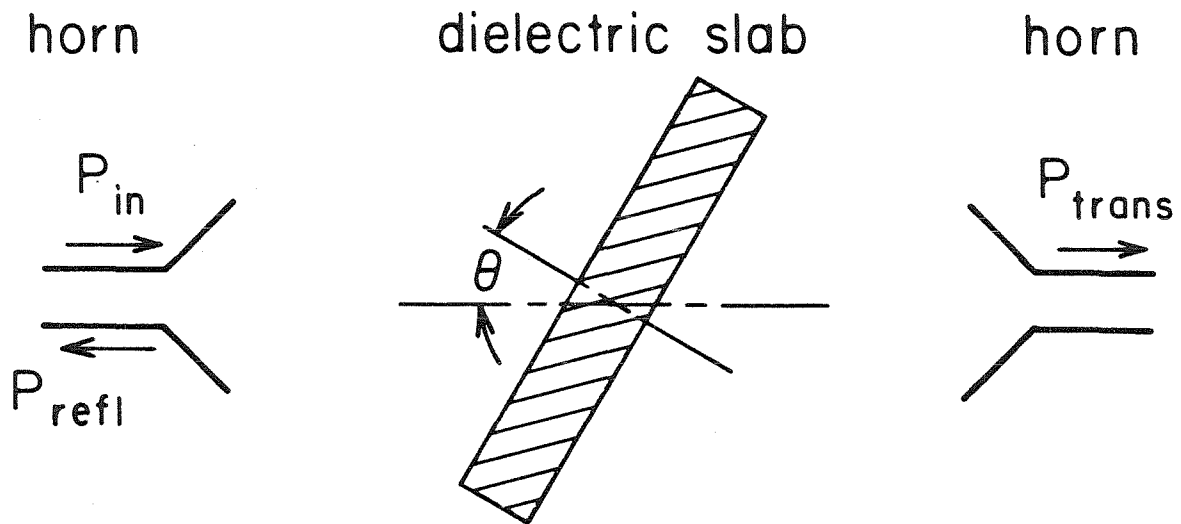
Figure 1. Free-space method for measuring the complex dielectric constant.
The measurement can be done by determining Brewster's angle and the trans-
mission losses through the sample. A microwave bridge can be used to
obtain the phase shift resulting from the presence of the sample.

advantage of a high measurement sensitivity but requires a careful error-analysis.[6]

A more elaborate form of this latter technique is the Michelson-type interference spectrometer.*[7] In this instrument, the radiation emitted from a broad band noise source is divided into two paths of variable length and recombined at a square law detector. The output of this detector is recorded as a function of the differential length in the two paths. The measurement of the dielectric constant is based on the determination of the phase shift due to the presence of the sample. The loss tangent is obtained by comparing wide resolution power spectra with and without the sample.

2.1.2   Open Resonator

Fabry-Perot confocal or semi-confocal resonators (Figs. 2 and 3) have been used for measuring complex dielectric permittivity in the millimeter wave range. The dielectric sample is a slab large enough to cover the region where the electric field is non-negligible. The change in length of the resonator required to bring it back into resonance after the sample is inserted determines the dielectric constant. The loss tangent is determined from the reduction in Q when the sample is in-verted. Great care must be exercised to distinguish the various modes of the resonator and to assure that the measurements correspond to identical modes.

* Also commonly referred to as a "Fourier transform spectrometer".
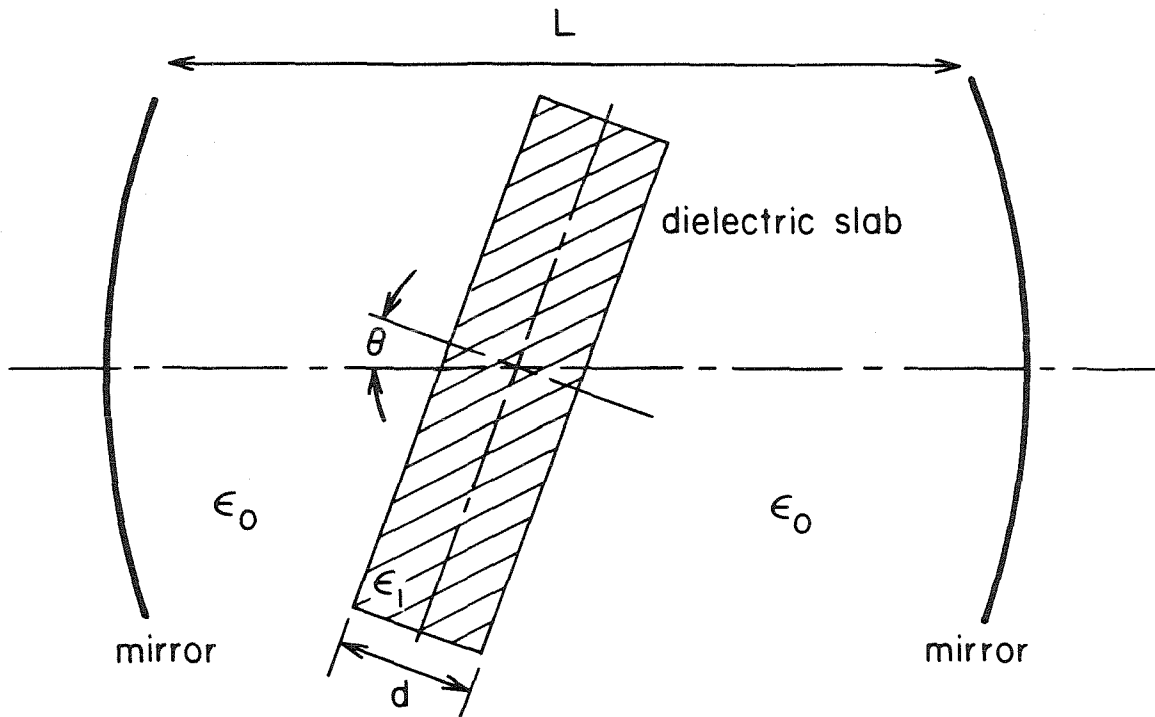
Figure 2. Fabry-Perot confocal resonator. The changes in resonant condition of the resonator determine the complex dielectric constant. The sample can be tilted to avoid multiple reflections and simplify the measurement of the permittivity.
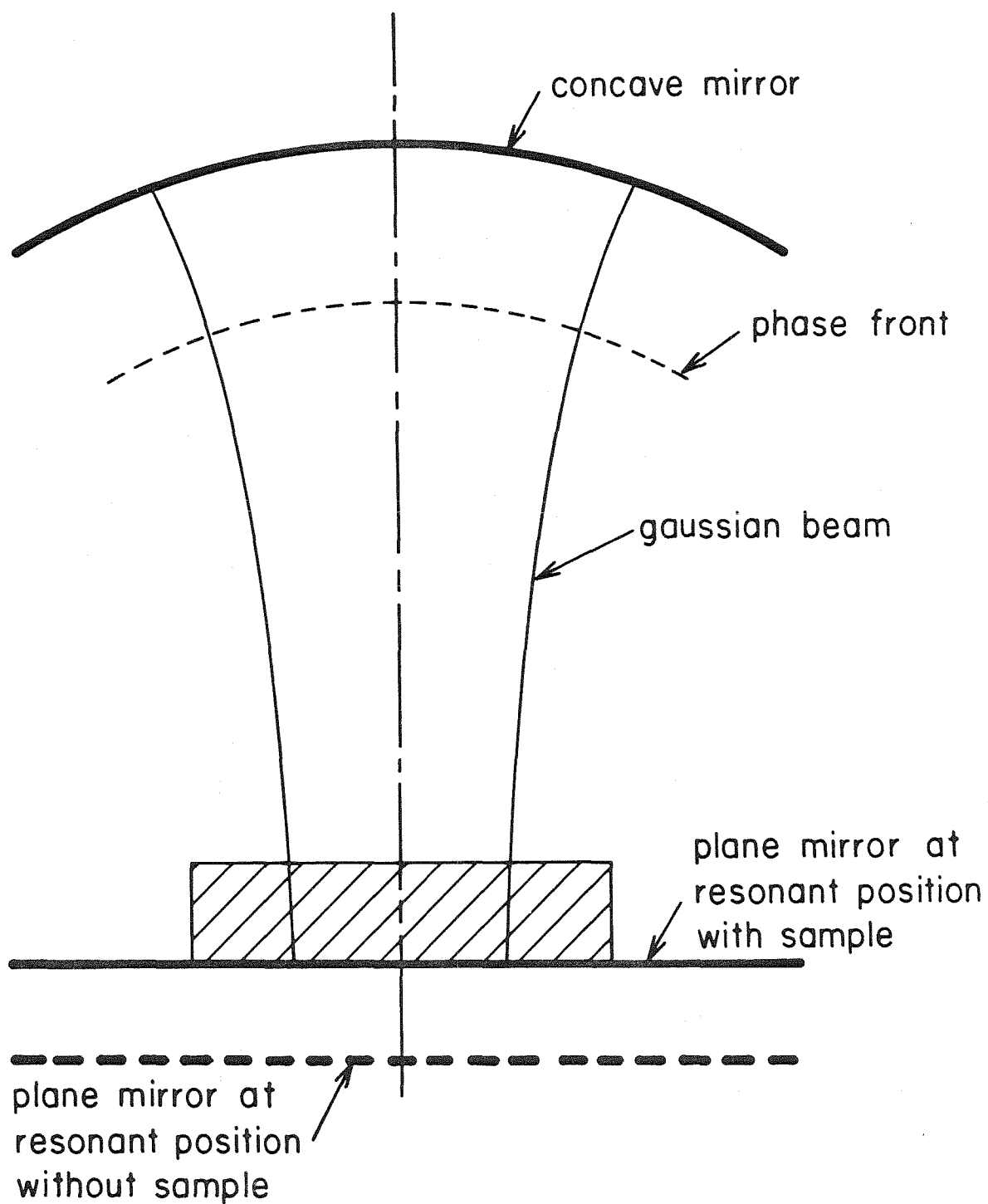
Figure 3. Semi-confocal resonator. The sample lies on the flat mirror.
The system is brought into resonance with and without the sample. The
changes in length and in Q-value determine the complex dielectric constant.

2.2 Cavity

This technique is based on the modification of the resonance condition of a closed metallic cavity due to the presence of a dielectric sample.[12] As the frequency of interest is increased to 100 GHz and above, the physical dimensions of the resonator become very small, in order to keep the wall losses low. Correct mode identification also becomes a problem and some authors recommend the use of several cavities to confirm a measurement without ambiguity.

3. Waveguide Techniques

The various methods described earlier have the disadvantage that they require a relatively large sample in the form of a slab with parallel faces that must be positioned accurately in free-space. The waveguide techniques that will be presented here require only a small sample and utilize standard test equipment. A new sample mounting technique[2] was developed at Hughes Research Laboratories and is applicable to a wide range of ductile materials. The dielectric samples are hot-pressed into copper wafers that have an aperture with dimensions corresponding to standard WR-10 waveguides. These wafers are then machined and polished to obtain flat, parallel faces (Fig. 4). We have used these wafers in two waveguide methods, the shorted waveguide and the waveguide Fabry-Perot. In both cases the properties of the dielectric are deduced from a standing-wave that is established within the dielectric.
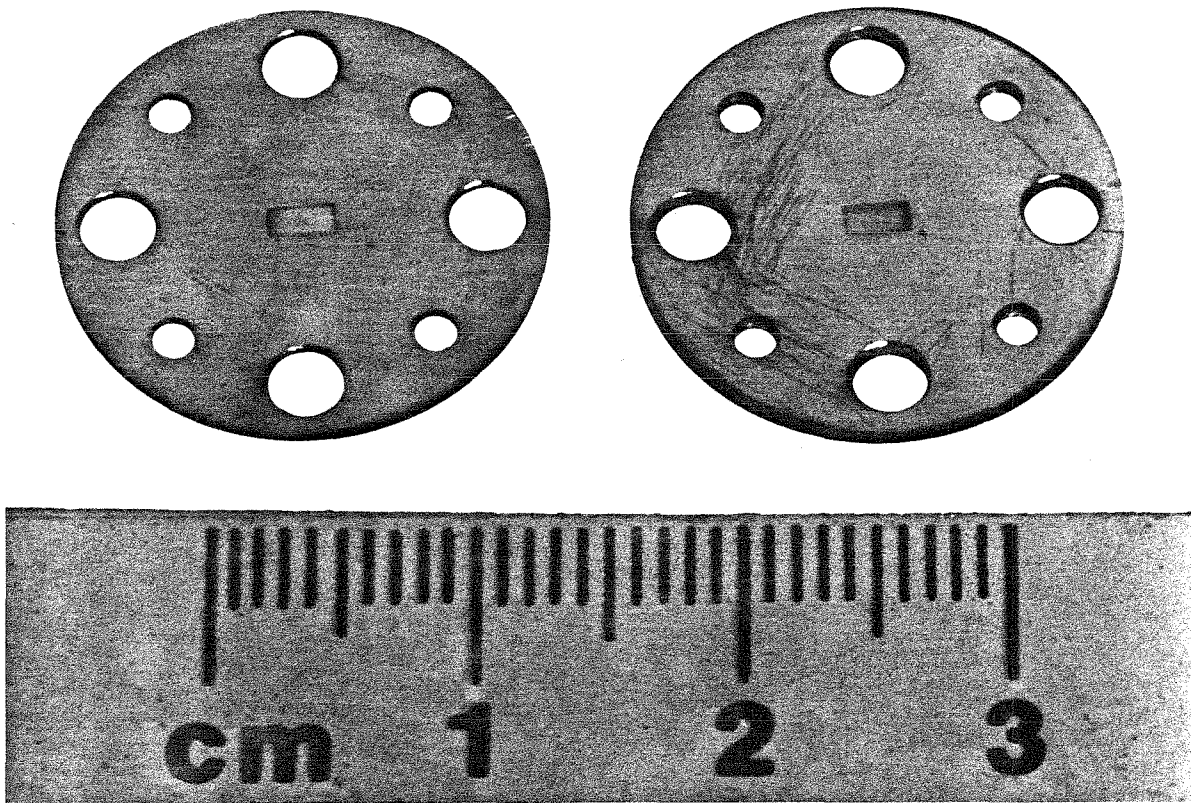
Figure 4. Waveguide wafers containing a sample of KRS-5. These wafers were made at the Hughes Research Laboratories and utilize a new sample mounting technique.

3.1 Shorted Waveguide

This method was first described by Roberts and von Hippel. [13]

A sample of the dielectric material is inserted at the shorted end of a waveguide. The voltage standing wave ratio (VSWR) is measured with the sample in place and with the sample removed (Figs. 5 and 6). The shift in position of a voltage minimum (node) due to the presence of the sample is also determined. With this information and also with the sample dimensions, the frequency and the guide wavelength, it is possible to deduce the complex permittivity of the sample. The method requires a slotted line or a similar device that allows measurement of a standing wave in amplitude and phase.

3.1.1 Mathematical Formulation

A standing wave in the waveguide can be represented as the sum of two traveling waves propagating in opposite directions. In the empty waveguide (medium 1) the transverse field components, $E_1(z)$ and $H_1(z)$. are given by:

$$E_1(z) = A_{1i} e^{-\gamma_1 z} + A_{1r} e^{\gamma_1 z} = A_{1i}(e^{-\gamma_1 z} + r_o e^{\gamma_1 z}) \tag{1a}$$

$$H_1(z) = \frac{A_{1i}}{Z_1} e^{-\gamma_1 z} - \frac{A_{1r}}{Z_1} e^{\gamma_1 z} = \frac{A_{1i}}{Z_1}(e^{-\gamma_1 z} - r_o e^{\gamma_1 z}) \quad , \tag{1b}$$

where A_{1i} and A_{1r} are the amplitudes (assumed real) of the incident and reflected waves at the dielectric interface. We have introduced in Equations 1 the complex reflection coefficient
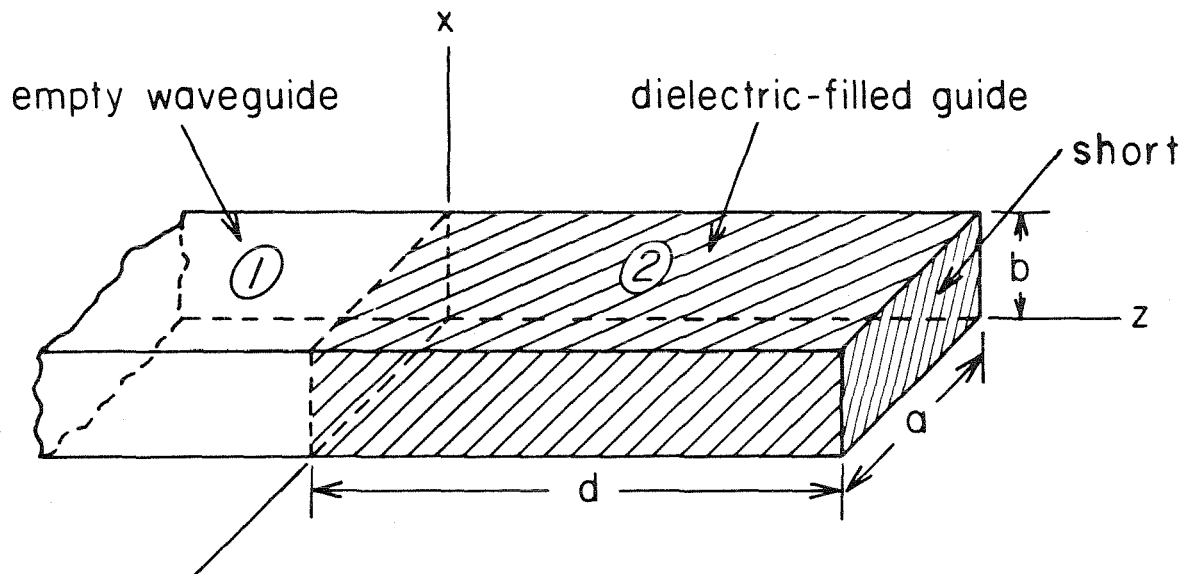
Figure 5. Shorted waveguide method for the measurement of dielectric constant. A sample of the dielectric material is inserted at the shorted end of the waveguide.
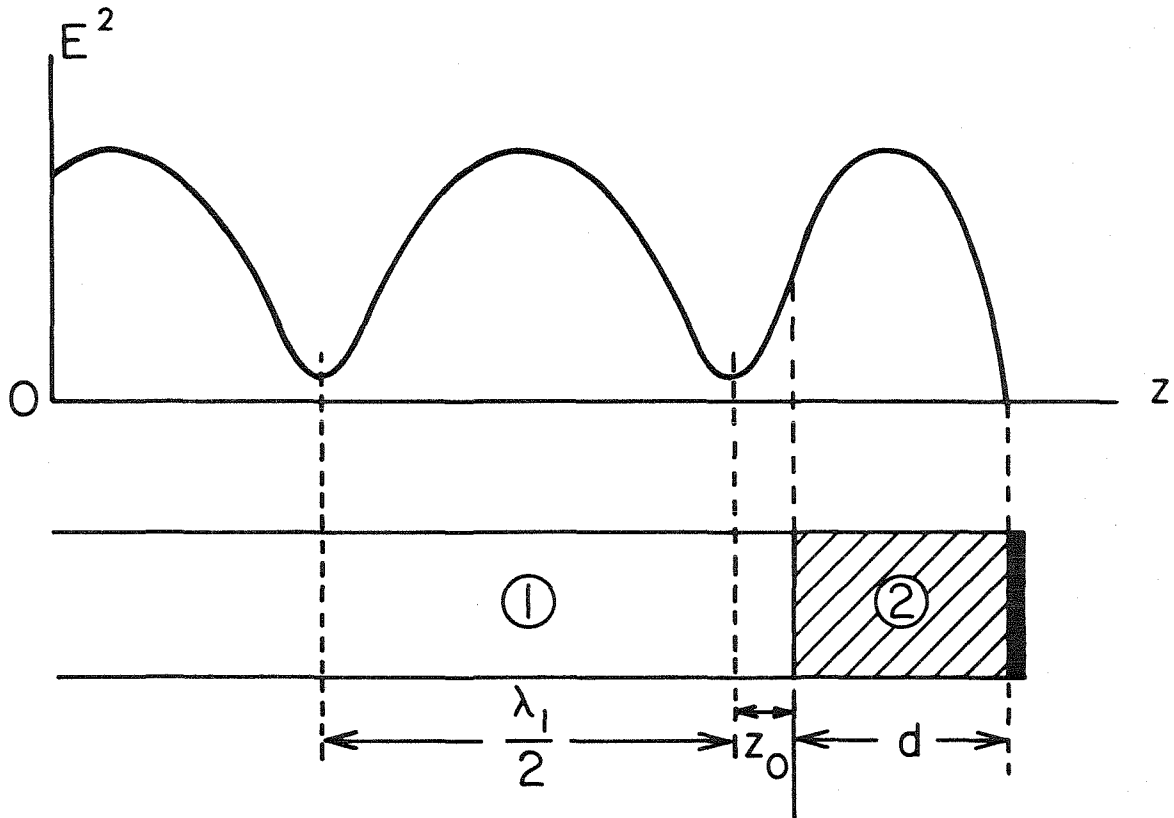
Figure 6. The shift in position of a node and the VSWR with the sample inserted at the shorted end of a waveguide determine the complex dielectric constant.

$$r_o = \frac{A_{1r}}{A_{1i}} \equiv e^{-2\phi} \tag{2}$$

where

$$\phi = \rho + j\psi \tag{3}$$

defines a reflection coefficient which characterizes the loaded guide. At the dielectric interface, $z = 0$, the wave impedance $Z = E/H$ is given by

$$Z(0) = \frac{E(0)}{H(0)} = Z_1 \frac{1 + r_o}{1 - r_o} = Z_1 \coth \phi \quad . \tag{4}$$

The attenuation in the air-filled waveguide can be neglected in most cases and the propagation constant γ_1 is

$$\gamma_1 = j\beta_1 = j \frac{2\pi}{\lambda_1} \quad , \tag{5}$$

where λ_1 is the wavelength inside the guide. The maximum and minimum amplitudes of the fields are:

$$E_{max} = |A_{1i}| \, (1 + |r_o|) = |A_{1i}| \, (1 + e^{-2\rho}) \tag{6a}$$

$$E_{min} = |A_{1i}| \, (1 - |r_o|) = |A_{1i}| \, (1 - e^{-2\rho}) \quad . \tag{6b}$$

Therefore:

$$\frac{E_{min}}{E_{max}} = \frac{1 - e^{-2\rho}}{1 + e^{-2\rho}} = \tanh \rho \ . \tag{7}$$

The first minimum above the dielectric boundary occurs at a point $z = -z_o$ where the reflected wave has a phase shift of π radians with respect to the incident wave, that is,

$$\frac{2\pi z_o}{\lambda_1} = -2\psi - \frac{2\pi z_o}{\lambda_1} - \pi \ . \tag{8}$$

If we expand $\coth \phi$ in Equation (4), we obtain

$$Z(0) = Z_1 \frac{\dfrac{E_{min}}{E_{max}} - j \tan \dfrac{2\pi z_o}{\lambda_1}}{1 - j \dfrac{E_{min}}{E_{max}} \tan \dfrac{2\pi z_o}{\lambda_1}} \ . \tag{9}$$

The impedance $Z(0)$ is determined by analyzing the standing wave in the dielectric-filled guide (Region 2). We assume that the power remains in the TE_{10} mode, even though higher order modes can propagate in this section. This assumption is supported by the fact that the planar normal air-dielectric interfaces and the constant metallic guide cross section do not encourage mode conversion. Thus, in Region 2:

$$E_2(z) = A_{2i} \, e^{-\gamma_2 z} + A_{2r} \, e^{\gamma_2 z} \qquad (10a)$$

$$H_2(z) = \frac{A_{2i}}{Z_2} \, e^{-\gamma_2 z} - \frac{A_{2r}}{Z_2} \, e^{\gamma_2 z} \qquad . \qquad (10b)$$

At $z = d$, the waveguide is terminated by a short that is assumed to be perfect. This introduces the boundary condition

$$E_2(d) = A_{2i} \, e^{-\gamma_2 d} + A_{2r} \, e^{\gamma_2 d} = 0 \qquad . \qquad (11)$$

Hence,

$$Z(0) = \frac{E_2(0)}{H_2(0)} = Z_2 \tanh \gamma_2 d \qquad . \qquad (12)$$

For a TE wave in Region 2, the following relation exists between the wave impedance and the propagation constant:

$$Z_2 = \frac{j\omega \, \mu_2}{\gamma_2} \qquad . \qquad (13a)$$

The permeability of the dielectric material, μ_2, is, in general, equal to the permeability of free space μ_o; therefore,

$$\gamma_2 Z_2 = j\omega\mu_o = \gamma_1 Z_1 \qquad (13b)$$

and

$$Z(0) = Z_1 \frac{\gamma_1}{\gamma_2} \tanh \gamma_2 d \quad . \tag{14}$$

Equating (9) and (14) yields

$$\frac{\tanh \gamma_2 d}{\gamma_2 d} = j \frac{\lambda_1}{2\pi d} \frac{\frac{E_{min}}{E_{max}} - j \tan \frac{2\pi z_o}{\lambda_1}}{1 - j \frac{E_{min}}{E_{max}} \tan \frac{2\pi z_o}{\lambda_1}} \quad . \tag{15}$$

The experimental measurement method then consists of the following steps:

- Measure the thickness of the sample d, the wavelength λ_1 in the air-filled guide, the standing-wave ration E_{min}/E_{max}* and the distance of the first minimum z_o from the dielectric boundary**.
- Compute the right-hand side of Equation (15) which determines the complex quantity

$$Ce^{j\zeta} \tag{16a}$$

- Solve numerically the transcendental equation for the complex variable $\gamma_2 d$

$$\frac{\tanh \gamma_2 d}{\gamma_2 d} = Ce^{j\zeta} \quad . \tag{16b}$$

---

* Note that the voltage standing wave ratio is defined by $VSWR = (E_{min}/E_{max})^{-1}$.
** This distance is in fact equal to the shift in the position of the voltage nodes due to the presence of the sample.

Compute the dielectric constant and the loss factor from

$$\varepsilon_2^* = \varepsilon_2' - j\varepsilon_2'' = \varepsilon_o \left[1 - \left(\frac{\lambda_o}{\lambda_1}\right)^2 - \left(\frac{\gamma_2 \lambda_o}{2}\right)^2 \right] \quad , \tag{17}$$

where λ_o is the free-space wavelength.

3.1.2 Optimum Sample Length

Roberts and von Hippel [13] point out that for low-loss materials it is desirable to use a thickness nearly equal to an odd multiple of λ. When attempting to measure [2] the loss tangent of low-loss, low-dielectric constant materials such as Teflon and Rexolite, we observed that it was necessary to use significantly longer samples: This is because the losses introduced by the sample must be larger than the losses due to the metallic walls.

To first approximation, the shift z_o in the position of the voltage nodes determines the dielectric constant of the sample, while the loss tangent is given by the VSWR of the loaded guide. In practice, VSWR's can be measured only in a limited range:

- The minimum value is determined by the mismatch of standard waveguide components: $VSWR_{min} = 1.2 \ (= 1.6 \text{ dB})$;
- The maximum value results from the finite conductivity of the waveguide walls and the short: $VSWR_{max} \simeq 30 \text{ dB}^{(*)}$.

This in turn determines a range of sample length for an accurate measurement of the loss tangent:

(*) measured about 50 mm from a copper short terminating a standard WR-10 waveguide.

- If the length is too small, the sample will introduce losses that are negligible compared to the waveguide losses;

- If the length is too large, the resulting VSWR will be masked by the residual VSWR of the components.

To determine the range of optimum length, we consider the VSWR created by a sample of length d, dielectric constant ε_2 and loss tangent $\tan \delta$ For small values of $\tan \delta$ (<0.1), Eq. (15) can be rewritten as: [14,15]

$$\frac{\tan \beta_2 d}{\beta_2 d} = - \frac{\lambda_g}{2\pi d} \tan \frac{2\pi z_o}{d} \tag{18}$$

$$\tan \delta = \frac{\lambda_g}{\pi d} \frac{E_{min}}{E_{max}} \left[1 - \frac{\lambda_o^2}{\varepsilon_2 \lambda_c^2} \frac{1 + \tan^2 \frac{2\pi z_o}{\lambda_g}}{1 + \tan^2 \beta_2 d - \frac{\tan \beta_2 d}{\beta_2 d}} \right] , \tag{19}$$

where $\beta_2 = \frac{2\pi}{\lambda_2}$ is the imaginary part of the propagation constant γ_2, λ_c is the guide cutoff wavelength and λ_2 is the wavelength in the dielectric-filled waveguide. We have:

$$\frac{1}{\lambda_g^2} = \frac{1}{\lambda_o^2} - \frac{1}{\lambda_c^2} \tag{20}$$

and

$$\lambda_2 = \frac{\lambda_o}{\sqrt{\varepsilon_2 - \left(\frac{\lambda_o}{\lambda_c}\right)^2}} \tag{21}$$

Denoting $\beta_2 d = x$, we can deduce from Eq. (18) and (19) that

$$\frac{E_{min}}{E_{max}} = \frac{\varepsilon_2 \pi d}{\lambda_g} \frac{1}{\left[\varepsilon_2 - (\frac{\lambda_o}{\lambda_c})^2\right]} \frac{x^2 \tan^2 x - x \tan x + x^2}{(\frac{2\pi d}{\lambda_g})^2 \tan^2 x + x^2} \quad . \quad (22)$$

At resonance,

$$d = (2n+1) \frac{\lambda_2}{4}$$

and   (23)

$$x = (2n+1) \frac{\pi}{2} \quad .$$

Eq. (22) becomes

$$\frac{E_{min}}{E_{max}}\bigg|_{res} = \varepsilon_2 \ \pi d \ \tan\delta \ \lambda_g (\frac{x}{2\pi d}) \frac{1}{\left[\varepsilon_2 - (\frac{\lambda_o}{\lambda_c})^2\right]}$$

Simplifying this expression, we obtain

$$\frac{E_{min}}{E_{max}}\bigg|_{res} = (2n+1) \frac{\pi}{4} \frac{\varepsilon_2 \tan\delta}{\sqrt{\varepsilon_2 - (\frac{\lambda_o}{\lambda_c})^2} \sqrt{1 - (\frac{\lambda_o}{\lambda_c})^2}} \quad . \quad (24)$$

At anti-resonance,

$$x = n\pi$$

and

$$d = n\frac{\lambda_2}{2} \quad .$$

Equation (22) becomes

$$\frac{E_{min}}{E_{max}} = n\frac{\pi}{2}\varepsilon_2 \tan\delta \frac{\lambda_2}{\lambda_g} \frac{1}{\left[\varepsilon_2 - (\frac{\lambda_o}{\lambda_c})^2\right]} \quad ,$$

which reduces to:

$$\frac{E_{min}}{E_{max}}\bigg|_{antires} = n\frac{\pi}{2}\varepsilon_2 \tan\delta \frac{\left[1 - (\frac{\lambda_o}{\lambda_c})^2\right]}{\left[\varepsilon_2 - (\frac{\lambda_o}{\lambda_c})^2\right]} \frac{1}{\left[\varepsilon_2 - (\frac{\lambda_o}{\lambda_c})^2\right]} \quad . \quad (25)$$

Comparing Eq. (24) and (25), we observe that for large n the ratio of

the peaks to the valleys of E_{min}/E_{max} is independent of sample length:

$$ratio = \frac{\varepsilon_2 - (\frac{\lambda_o}{\lambda_c})^2}{1 - (\frac{\lambda_o}{\lambda_c})^2} \quad (26)$$

This quantity depends primarily on the dielectric constant. At 94.75 GHz

in a WR-10 waveguide (λ_c = 5.080 mm),

ratio = 6.8 dB   for ε_2 = 2.1 (Teflon)

and

ratio = 32   dB   for ε_2 = 32   (KRS-5,6).

In Figs. 7 and 8, the inverse standing wave ratio, E_{min}/E_{max}, is plotted

versus normalized lengths d/λ_2, for two different sets of dielectric

constant and loss tangent, corresponding respectively to Teflon and

KRS-5.   Figures 9 and 10 represent only the maxima and minima of this

function that vary linearly with length, as indicated by Equations (24)

and (25).   As mentioned before, interrupted lines corresponding to the

limits of measurable VSWR also appear on these figures.   In the case of

low-index, low-loss materials, such as Teflon, it is necessary to consider

relatively long samples that introduce a VSWR below the upper limit of

30 dB.   On the contrary, for high-index, high-loss samples such as KRS-5,

the samples must be short enough so that the VSWR is kept above the lower

limit of 1.2.   It also appears from these figures that sample lengths

nearly equal to resonant lengths give the best accuracy in the determina-

tion of tan δ.   Similarly for these lengths, as it results from Eq.

(18) and its graphical representation in Fig. 11, the measurement of the

shift, z_o, will result in a more accurate value of λ_2, and hence a smaller

uncertainty in the dielectric constant ε_2.   Therefore, an accurate

measurement by the shorted waveguide technique of complex dielectric

constant requires resonant lengths.
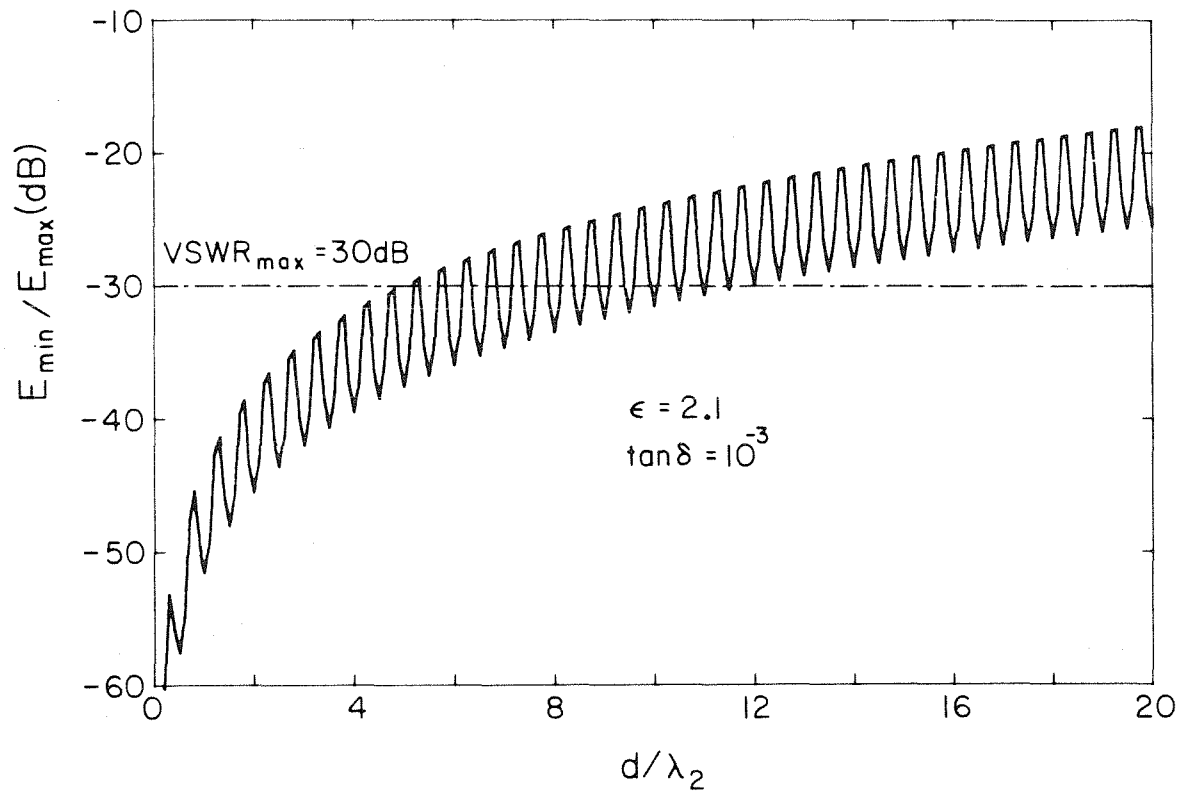
Figure 7. The field ratio (E_{min}/E_{max} = VSWR^{-1}) is plotted versus the normalized length of the sample. In case of a low-index and low-loss sample, the sample must be long enough to obtain a VSWR lower than the maximum measurable value.
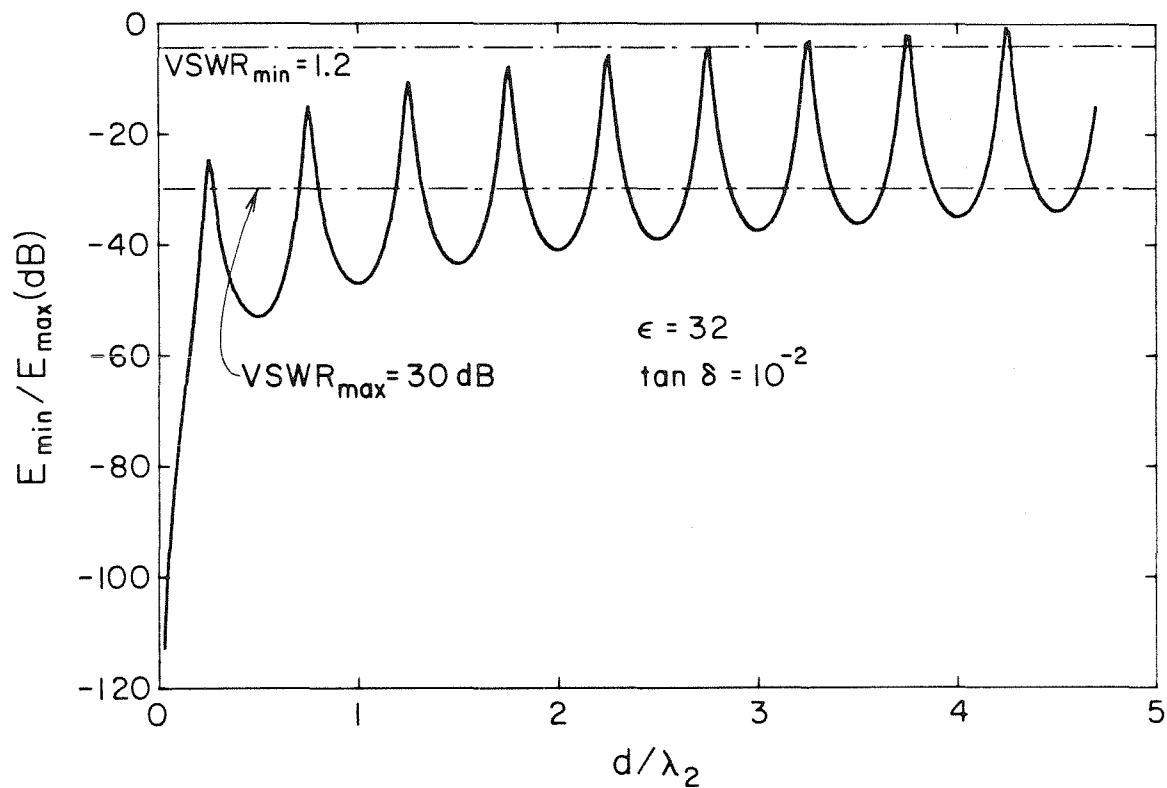
Figure 8. In case of a high-index, high-loss sample, the peaks are always located below the maximum VSWR value ($E_{min}/E_{max} = VSWR^{-1}$); if the sample is chosen too long, the resulting VSWR will be smaller than the minimum measurable value.
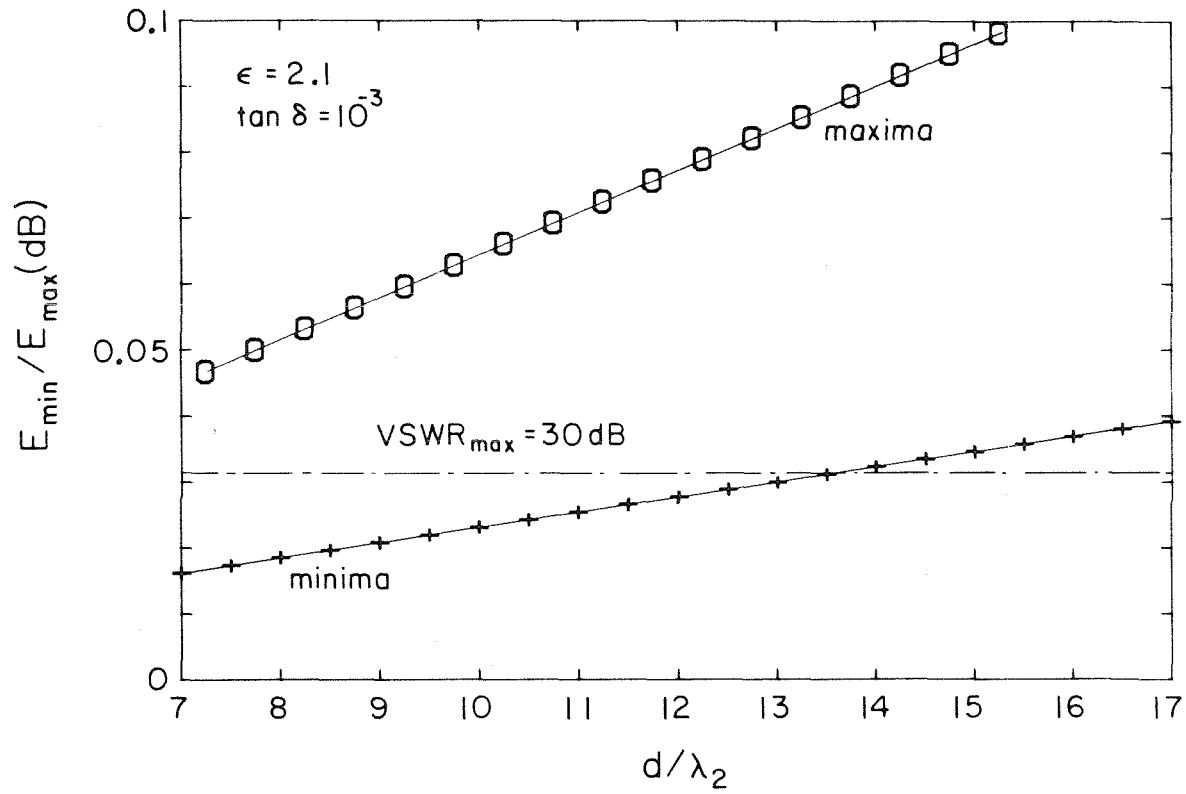
Figure 9. The maxima and minima of the field ratio (E_{min}/E_{max}) are plotted versus the normalized length of the sample. The maxima correspond to odd multiples of quarter wavelengths while the minima correspond to half wavelengths.
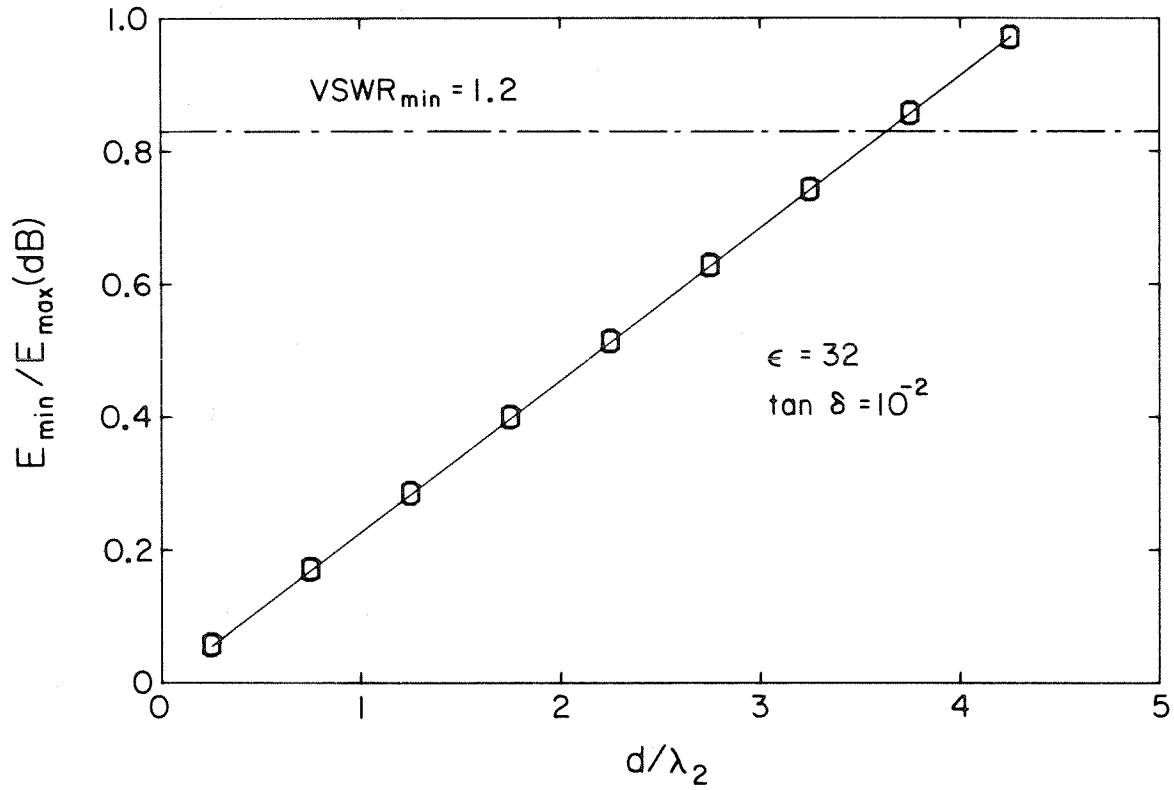
Figure 10. In the case of a high-index, high-loss sample, the peaks
only correspond to favorable lengths for determining the dielectric
loss tangent. If the sample is too long, the resulting VSWR cannot
be measured.
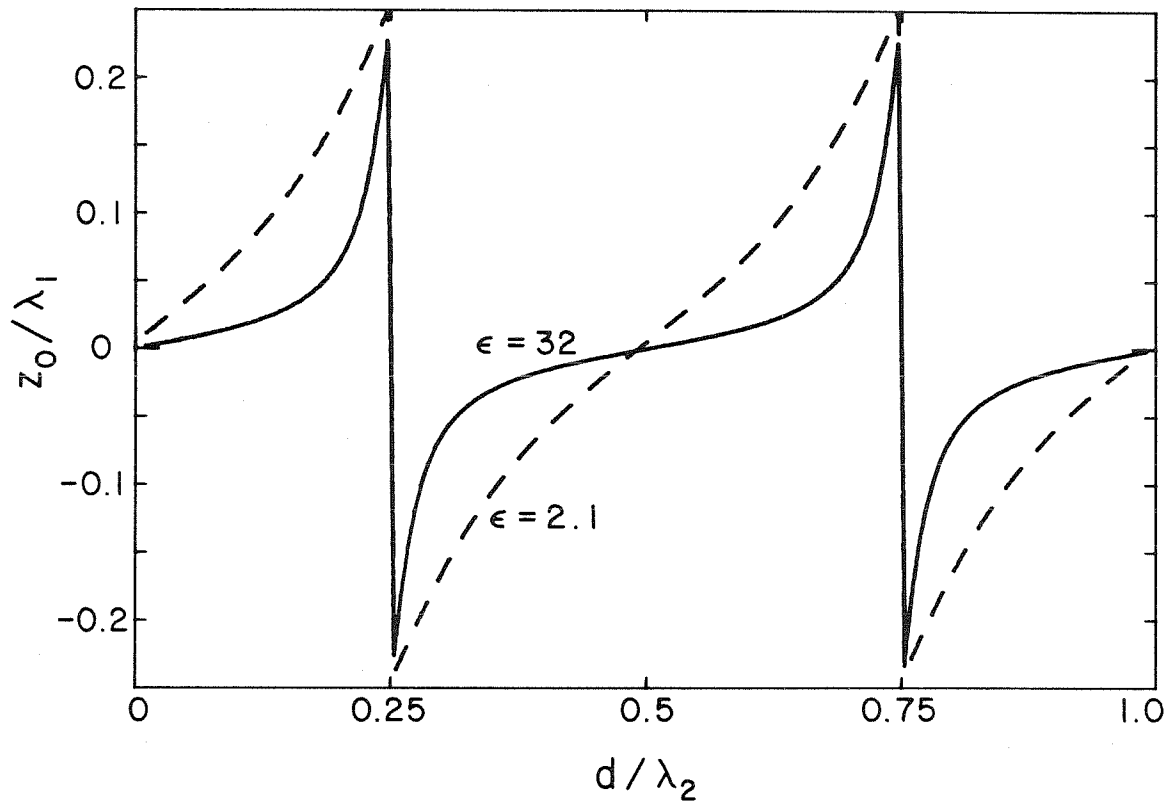
Figure 11. The shift in position of a voltage node is plotted versus the normalized sample length. The resonances occur for odd multiples of a quarter wavelength and correspond to favorable lengths for the measurement of the dielectric constant.

3.1.3 Air Gaps

The effect of an air gap can be roughly described by using a quasi-static approximation which leads us to consider two capacitors in series, one formed by the dielectric and the other by the air gap [16]. For a gap of thickness g, located along the broad wall of a waveguide of height b, the corrected values ε_c and $\tan \delta_c$ are obtained from the measured values, respectively, ε_m and $\tan \delta_m$,

$$\varepsilon_c = \varepsilon_m \frac{b - g}{b - g\varepsilon_m} \quad , \qquad (27)$$

$$\tan\delta_c = \tan\delta_m \frac{b - g}{b - g\varepsilon_m} \quad . \qquad (28)$$

These equations show that the errors introduced by an air gap increase rapidly with the dielectric constant of the sample. As it appears under a microscope (see Fig. 12), our new sample mounting technique completely eliminates air gaps and thus no correction was made to our results.

3.1.4 Waveguide Wall Losses

As suggested by Dakins and Works [14], the effect of wall losses can be estimated by applying Eq. (19) to the empty waveguide. It results that,

$$\tan \delta_w = \frac{\lambda_g}{\pi d_w} \frac{E_{min}}{E_{max}} \left[1 - \frac{\lambda_o^2}{\lambda_c^2} \right] \quad , \qquad (29)$$

137
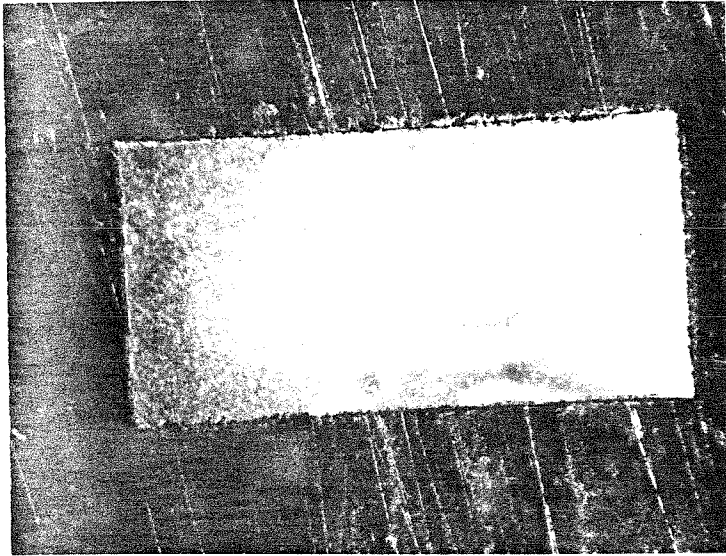
Figure 12. Enlarged view of the central portion of the waveguide wafers
containing a sample of KRS-5. No air gaps can be distinguished under
the microscope. The thin white line around the sample is the gold layer
that prevents the copper wafer from oxidizing when the material is
pressed.

where d_w is the length of empty waveguide from the short to the position

of the slotted line probe and $\tan \delta_w$ is the equivalent loss tangent of

the guide. This equation does not take into account the losses due to

the imperfect short, for which no model exists.

At 94.75 GHz, in a silver WR-10 waveguide, terminated by a copper

short, the standing wave was measured to be about 30 dB at 50 mm from

the short. Therefore the loss tangent is

$$\tan \delta_w = 5 \times 10^{-4} \quad ,$$

which corresponds to an attenuation

$$\alpha_w = 4 \text{ dB/m} \quad^{(*)} \quad .$$

The correction to the measured value of $\tan \delta_m$ is then [14]

$$\tan \delta_c = \tan \delta_m - \tan \delta_w \quad . \tag{30}$$

As our samples presented a loss tangent of at least one order of magnitude

larger than $\tan \delta_w$, we did not apply any correction.

(*) This is an estimate that compares very well with the value quoted
     by the technical literature: $\alpha_w = 5$ dB/m at 94 GHz.

3.2 Results of Measurements

The experimental arrangement is shown in Fig. 13b. The position
of a node was determined with a W-band slotted line (Alpha/TRG Model W740).
To obtain the complex dielectric constant from the measurements, a com-
puter program was written along the lines of the program used by Nelson,
et al. [15]

The values of complex dielectric constant obtained at 94.75 GHz
for the samples of KRS-5 and KRS-6 are given in Table I. The agreement
between the various samples is quite good. The larger dispersion in the
loss tangent of the KRS-6 samples is presumed to be due to sample im-
perfections: KRS-6 is less ductile than KRS-5 and the wafers presented
some cracks visible under a microscope.

In order to check further the accuracy of our experimental technique,
we measured the dielectric properties of Teflon and Rexolite at 95 GHz.
In this case it was necessary to use substantially longer samples,
Accordingly, we machined long samples of Teflon and Rexolite ($\sim$13 mm)
to slip fit in WR-10 waveguides. Our results for these samples were:

$$\varepsilon_r' = 2.4 \qquad \tan\delta = 3.3 \times 10^{-3} \text{ for Rexolite,}$$

$$\varepsilon_r' = 1.9 \qquad \tan\delta = 4 \times 10^{-3} \text{ for Teflon.}$$

The measured values of dielectric constant are in good agreement with
literature values [17,18,19] for Rexolite (2.47 - 2.58) and Teflon
(2.0 - 2.1), while the measured values of loss tangent are larger than

10558—1
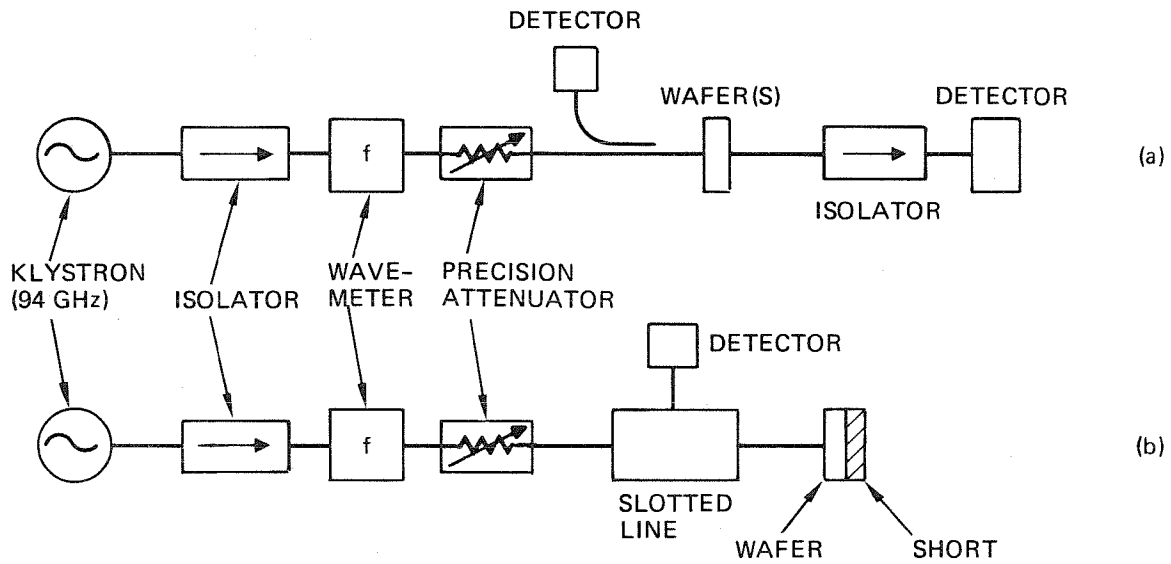
Figure 13. Experimental arrangements used for the waveguide measurement
of complex dielectric constant.

    (a)   Fabry-Perot resonances in reflection and transmission;

    (b)   Shorted-waveguide method.

the literature values [17,18,19] for Rexolite (1.2×10^{-3}) and Teflon (2×10^{-3} - 3×10^{-3}). We should, however, note that there is no "accepted" value for tanδ at millimeter wave frequencies, and that literature values often differ by as much as a factor of 2. In any case, since our measured value of tan KRS-5 and KRS-6 are one order of magnitude larger, we feel that our method is reasonably accurate for these materials.

As a check on the 10 GHz values of ε_r' and tanδ quoted vaguely by von Hippel [1], we also made a shorted waveguide measurement at 10 GHz, using an X-band setup similar to the one depicted on Fig. 13b. In this case the samples were machined to size and slipped into the end of a standard X-band waveguide. Our average results at 10 GHz for KRS-5 were:

$$\varepsilon_r' = 30.6 \quad \tan\delta = 4 \times 10^{-3} \quad .$$

As mentioned in Ref. 2, it is possible to model to first approximation the frequency behavior of the losses in KRS-5. The low-frequency behavior corresponds to ionic conductivity, whereas at microwave and millimeter wave frequencies the behavior is dominated by the tail of the lattice absorption centered at about 1400 GHz. Our measured values and these models are depicted in Fig. 14.

TABLE I

Experimental Values of ε_r' and tan δ at 94.75 GHz by the Shorted Waveguide
Method

Sample Thickness (mm)	Material	ε_r'	Tan δ
0.942	KRS-5	31.7	1.7×10^{-2}
0.940	KRS-5	31.9	1.7×10^{-2}
0.686	KRS-5	31.1	1.9×10^{-2}
0.414	KRS-5	31.5	1.6×10^{-2}
0.973	KRS-6	30.8	1.1×10^{-2}
0.777	KRS-6	31.0	3.3×10^{-2}
0.483	KRS-6	30.8	3.6×10^{-2}
0.358	KRS-6	30.8	1.0×10^{-2}
12.532	Rexolite	2.41	3.4×10^{-3}
12.517	Rexolite	2.41	3.2×10^{-3}
14.030	Teflon	1.94	4.1×10^{-3}
13.872	Teflon	1.98	4.7×10^{-3}
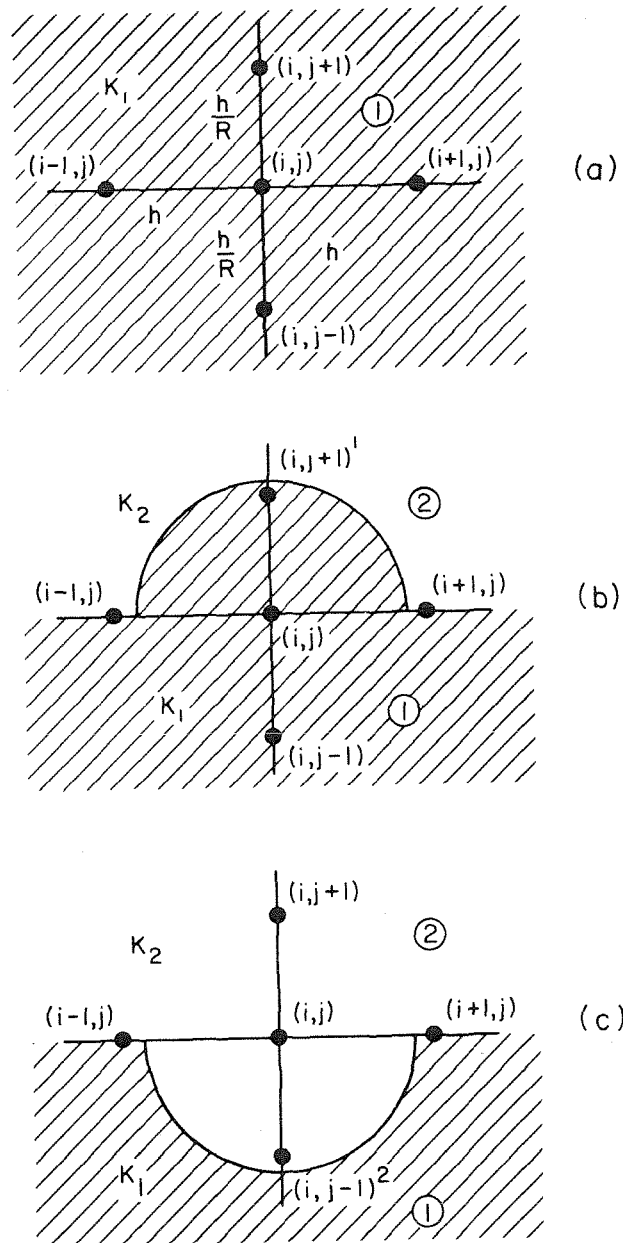
Figure 2. a) An interior point (i,j) and its four nearest neighbors in the mesh are represented in this graphical illustration of the five-point Laplace difference operator.

b) Image terms are obtained when the interface is approached from the dielectric and the point (i,j) is considered to be inside region 1.

c) The other set of image terms is obtained when the interface is approached from the outer medium and the point (i,j) is considered inside region 2.
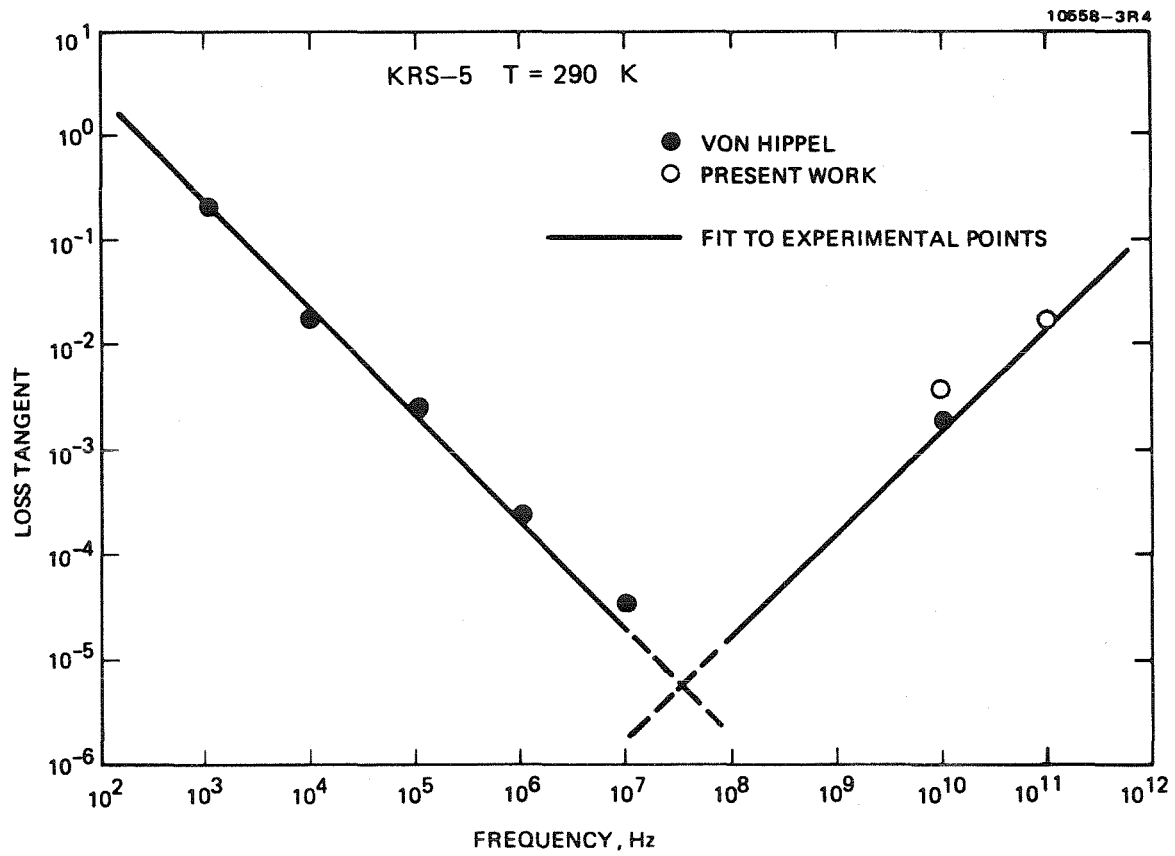
Figure 14. Measured values of the loss tangent of KRS-5 and theoretical behavior due to ionic conductivity (10^3 to 10^7 Hz) and lattice absorption (above 10^7 Hz).

3.3 Waveguide Fabry-Perot

Our sample mounting method allowed us to build a waveguide Fabry-Perot experiment, where multiple reflections are created between the parallel faces of our samples and the total transmission or reflection coefficient is measured as a function of sample length [2]. The experimental setup is illustrated in Fig. 13a. Results obtained by this method are comparable to the results from the shorted waveguide experiments. The theory of the Fabry-Perot measurements and the experimental results obtained are discussed in Ref. 2 and will not be repeated here.

PART III BIBLIOGRAPHY

1. A. von Hippel, Dielectric Materials and Applications, John Wiley & Sons, Inc., New York, 1954, p. 302, 374, 375.

2. W. B. Bridges, M. B. Klein and E. Schweig, "Measurement of the Dielectric Constant and Loss Tangent of Thallium Mixed Halide Crystals KRS-5 and KRS-6 at 95 GHz", IEEE Trans. Microwave Th. Tech., Vol. MTT-30, pp. 286-292, March 1982.

3. R. M. Redheffer, "The Measurement of Dielectric Constants", in Techniques of Microwave Measurements , C. G. Montgomery, Ed., McGraw-Hill, New York, 1947, pp. 561-676.

4. C. K. Campbell, "Free-space Permittivity Measurements on Dielectric Materials at Millimeter Wavelengths", IEEE Trans. Instrum. Meas., Vol. IM-27, pp. 54-58, March 1978.

5. A. C. Lynch, "Precise Measurements on Dielectric and Magnetic Materials", IEEE Trans. Instrum. Meas., Vol. IM-23, pp. 424-431, Dec. 1974 and references therein contained.

6. K. H. Breeden, "Error Analysis for Waveguide-Bridge Dielectric Constant Measurements at Millimeter Wavelengths", IEEE Trans. Instrum. Meas., Vol. IM-18, pp. 203-208, Sept. 1969.

7. K. H. Breeden and A. P. Sheppard, "Millimeter and Submillimeter Wave Dielectric Measurements", The Microwave J., pp. 59-62, Nov. 1967.

8. J. E. Degenford and P. D. Coleman, "A Quasi-Optic Perturbation Technique for Measuring Dielectric Constants", Proc. IEEE, Vol. 54, pp. 520-522, April 1966.

9. J. E. Degenford, "A Quasi-Optic Technique for Measuring Dielectric Loss Tangents", IEEE Trans. Instrum. Meas., Vol. IM-17, pp. 413-417, Dec. 1968.

10. R. G. James, "Precise Dielectric Measurements at 35 GHz Using an Open Microwave Resonator", Proc. IEE, Vol. 123, pp. 285-290, April 1976.

11. A. L. Cullen and P. K. Yu, "The Accurate Measurement of Permittivity by Means of an Open Resonator", Proc. R. Soc. Lond., Vol. A.325, pp. 493-509, 1971.

12. R. J. Cook, R. Jones, and C. B. Rosenberg, "Comparison of Cavity and Open-Resonator Measurements of Permittivity and Loss Angle at 35 GHz", IEEE Trans. Instrum. Meas., Vol. IM-23, pp. 438-442, Dec. 1974 and references therein contained.

13. S. Roberts and A. von Hippel, "A New Method for Measuring Dielectric Constant and Loss Tangent in the Range of Centimeter Waves", J. Appl. Phys., Vol. 17, pp. 610-616, July 1946.

14. T. W. Dakin and C. N. Works, "Microwave Dielectric Measurements", J. Appl. Phys., Vol. 18, pp. 789-796, Sept. 1946.

15. S. Nelson, C. Schlaphoff, L. Stetson, "Computer Program for Calculating Dielectric Properties of Low- and High-Loss Materials from Short-Circuited Waveguide Measurements", U.S. Dept. of Agr. Report #ARS-NC-4, Nov. 1972.

16. H. Altschuler, "Measurement of Dielectric Constant", in Handbook of Microwave Measurements , M. Sucher and J. Fox, Ed., Polytechnic Press, New York, 3rd. ed., p. 539.

17. K. H. Breeden and A. P. Sheppard, "A Note on the Millimeter and Submillimeter Wave Dielectric Constant and Loss Tangent Value of Some Common Materials", Radio Science, Vol. 3 (new series), p. 205, Feb. 1968.

18. F. Sobel, F. L. Wentworth, and J. C. Wiltse, "Quasi-Optical Surface Waveguide and Other Components for the 100 to 300 GHz Region", IRE Trans. Microwave Th. Tech., Vol. MTT-9, pp. 512-518, Nov. 1961.

19. D. Jablonski, "Attenuation Characteristics of Circular Dielectric Waveguide at Millimeter Wavelengths", IEEE Trans. Microwave Th. Tech., Vol. MTT-26, pp. 667-671, Sept. 1978.

APPENDIX A

Waveguide Modes: Longitudinal Field Formulation

The general mode of a waveguide of axis z is a combination of TE and TM modes[1]. A complete description of the $\vec{E}$- and $\vec{H}$-fields requires the knowledge of six components. However, because of Maxwell curl equations, only two components are independent. It is most common to formulate the problem of dielectric guides in terms of the longitudinal components E_z and H_z. The four remaining components, the transverse ones, can be derived from E_z and H_z. Assuming a z-dependence of the form $\exp(-j\beta z)$, the longitudinal components must satisfy the wave equation

$$\nabla_t^2 H_z + k_q^2 H_z = 0 \tag{1}$$

$$\nabla_t^2 H_z + k_q^2 H_z = 0 \quad , \tag{2}$$

where

$$k_q^2 = n_q^2 k_o^2 - \beta^2 \qquad \text{in region q.} \tag{3}$$

The transverse components are given by

$$E_x = -\frac{j\beta}{k_q^2} \frac{\partial E_z}{\partial x} - \frac{j\omega\mu}{k_q^2} \frac{\partial H_z}{\partial y}$$

$$E_y = -\frac{j\beta}{k_q^2} \frac{\partial E_z}{\partial y} + \frac{j\omega\mu}{k_q^2} \frac{\partial H_z}{\partial y}$$

$$H_x = \frac{j\omega n_q^2}{k_q^2} \frac{\partial E_z}{\partial y} - \frac{j\beta}{k_q^2} \frac{\partial H_z}{\partial x}$$

$$H_y = -\frac{j\omega n_q^2}{k_q^2}\frac{\partial E_z}{\partial x} - \frac{j\beta}{k_q^2}\frac{\partial H_z}{\partial y} \tag{4}$$

in rectangular coordinates [x,y,z] , and,

$$E_r = -\frac{j\beta}{k_q^2}\frac{\partial E_z}{\partial r} - \frac{j\omega\mu}{k_q^2}\frac{1}{r}\frac{\partial H_z}{\partial \phi}$$

$$E_\phi = -\frac{j\beta}{k_q^2}\frac{1}{r}\frac{\partial E_z}{\partial \phi} + \frac{j\omega\mu}{k_q^2}\frac{\partial H_z}{\partial r}$$

$$H_r = \frac{j\omega n_q^2}{k_q^2}\frac{1}{r}\frac{\partial E_z}{\partial \phi} - \frac{j\beta}{k_q^2}\frac{\partial H_z}{\partial r}$$

$$H_\phi = -\frac{j\omega n_q^2}{k_q^2}\frac{\partial E_z}{\partial r} - \frac{j\beta}{k_q^2}\frac{1}{r}\frac{H_z}{\partial \phi} \tag{5}$$

in cylindrical coordinates [r,ϕ,z].

Appendix A Bibliography

1. R. Collins, Field Theory of Guided Waves , McGraw-Hill, New York,

1960.

APPENDIX B:

FD-Matrices

As mentioned in Part II, the finite-differences (FD) method

utilizes a mesh that covers the region of interest with rectangular

elements in such a way that the boundaries and the two axes of symmetry

divide, each one respectively, a row of elements in two equal halves[*] (Part

II, Fig. 6) . Therefore, we have four types of rectangular elements:

a) the general rectangular element (Fig. 1.a);

b) the element divided in two by a line parallel to the x-axis

(Fig. 1.b);

c) the element divided in two by a line parallel to the y-axis

(Fig. 1.c);

d) the element divided by two orthogonal lines (Fig. 1.d).

On each of these lines, an electric or magnetic boundary condition must

be applied. Let us define the quantities s and s' that define the

symmetry of the longitudinal field $\phi = H_z$ with respect to one of these

axes: s and s' take the values ± 1. If, for example, for the element

illustrated in Fig. 1.b, s takes the value +1, this signifies that

ϕ is an even function about the axis and therefore $\psi = \frac{\omega \varepsilon_0}{\beta} E_z$ must

be an odd function: $\phi_2 = \phi_1$, $\phi_4 = \phi_3$, $\psi_2 = - \psi_1$, $\psi_4 = - \psi_3$. This

is equivalent to an electric boundary condition.

---

[*] The outer "box" corresponds to an electric wall boundary condition.
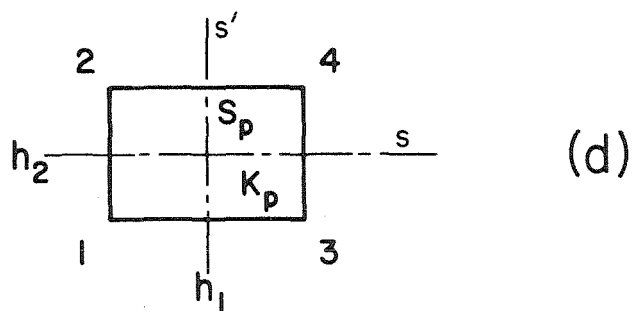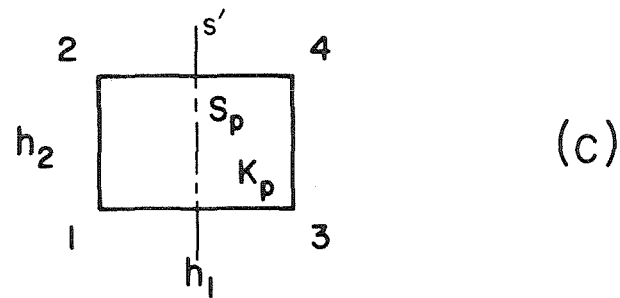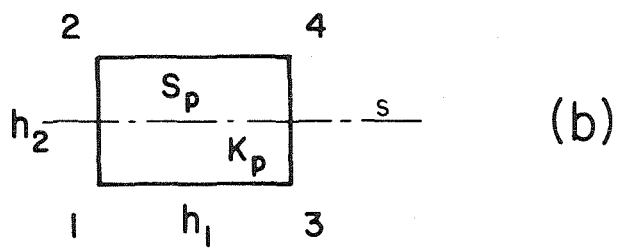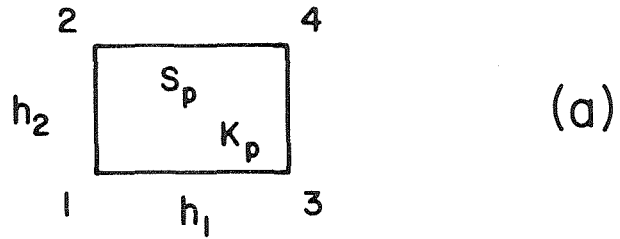
Figure 1. The element used for FD-calculations can either be the
general element (a) or an element divided by one (b,c) or two symmetry
axes (d). The parameters s and s' define the symmetry of the longitudinal
magnetic field with respect to the x- and y-axis: s and s' take the values
$\pm$ 1. For example, $H_z \big|_1 = s\ H_z \big|_2$, while $H_z \big|_1 = s'\ H_z \big|_3$.

We can now evaluate the contribution of these elements to the FD

matrices A and B (Eq. II-55) by using the FD approximations (Eqs.

II-52-54). For each element, S_p, we can write a relation of the

form

$$[\frac{\partial J_p}{\partial \phi_i}, \frac{\partial J_p}{\partial \psi_i}]^T = A_p [\phi_i, \psi_i]^T - k_A^2 B_p [\phi_i, \psi_i]^T \quad . \tag{1}$$

These relations are then summed to form $A X = k_A^2 B X$. For the general

element (Fig. 1.a), Eq. 1 becomes *

$$
\begin{bmatrix}
\frac{\partial J_p}{\partial \phi_1} \\[4pt]
\frac{\partial J_p}{\partial \psi_1} \\[4pt]
\frac{\partial J_p}{\partial \phi_2} \\[4pt]
\frac{\partial J_p}{\partial \psi_2} \\[4pt]
\frac{\partial J_p}{\partial \phi_3} \\[4pt]
\frac{\partial J_p}{\partial \psi_3} \\[4pt]
\frac{\partial J_p}{\partial \phi_4} \\[4pt]
\frac{\partial J_p}{\partial \psi_4}
\end{bmatrix}
=
\begin{bmatrix}
\tau(R+\frac{1}{R}) & 0 & -\tau R & W & -\frac{\tau}{R} & -W & 0 & 0 \\
 & P(R+\frac{1}{R}) & -W & -PR & W & \frac{-P}{R} & 0 & 0 \\
 & & \tau(R+\frac{1}{R}) & 0 & 0 & 0 & -\frac{\tau}{R} & W \\
 & & & P(R+\frac{1}{R}) & 0 & 0 & -W & \frac{-P}{R} \\
 & & & & \tau(R+\frac{1}{R}) & 0 & -\tau R & -W \\
 & & & & & P(R+\frac{1}{R}) & W & -PR \\
 & & & & & & \tau(R+\frac{1}{R}) & 0 \\
 & & & & & & & P(R+\frac{1}{R})
\end{bmatrix}
\begin{bmatrix}
\phi_1 \\ \psi_1 \\ \phi_2 \\ \psi_2 \\ \phi_3 \\ \psi_3 \\ \phi_4 \\ \psi_4
\end{bmatrix}
$$

$$
- \frac{h_1 h_2}{2} k_A^2 \; \text{diag} [1, P', 1, P', 1, P', 1, P']
\begin{bmatrix}
\phi_1 \\ \psi_1 \\ \phi_2 \\ \psi_2 \\ \phi_3 \\ \psi_3 \\ \phi_4 \\ \psi_4
\end{bmatrix}
, \tag{2}
$$

where

$$\tau = \frac{\overline{\beta}^2 - 1}{\overline{\beta}^2 - K_p} \tag{3}$$

$$P' = \overline{\beta}^2 K_p \tag{4}$$

$$P = \overline{\beta}^2 K_p \tau \tag{5}$$

$$W = \overline{\beta}^2 \tau \tag{6}$$

Using the symmetry parameters s and s' we can compute the contribution

of the element illustrated:

in Fig. 1.b.:

$$
\begin{bmatrix} \dfrac{\partial J_p}{\partial \phi_2} \\[6pt] \dfrac{\partial J_p}{\partial \psi_2} \\[6pt] \dfrac{\partial J_p}{\partial \phi_4} \\[6pt] \dfrac{\partial J_p}{\partial \psi_4} \end{bmatrix}
=
\begin{bmatrix}
\tau[(1-s)^2 R + \tfrac{2}{R}] & 2Ws & \tfrac{-2\tau}{R} & 2W \\[6pt]
& P[(1+s)^2 R + \tfrac{2}{R}] & -2W & \tfrac{-2P}{R} \\[6pt]
& & [(1-s)^2 R + \tfrac{2}{R}] & -2Ws \\[6pt]
& & & P[(1-s^2 R + \tfrac{2}{R}]
\end{bmatrix}
\begin{bmatrix} \phi_2 \\[6pt] \psi_2 \\[6pt] \phi_4 \\[6pt] \psi_4 \end{bmatrix}
$$

$$
- k_A^2 h_1 h_2 \ \text{diag} \ [1, P', 1, P'] \begin{bmatrix} \phi_2 \\ \psi_2 \\ \phi_4 \\ \psi_4 \end{bmatrix} \quad ; \tag{7}
$$

156

in Fig. 1.c.:

$$
\begin{bmatrix} \dfrac{\partial J_p}{\partial \phi_3} \\[2mm] \dfrac{\partial J_p}{\partial \psi_3} \\[2mm] \dfrac{\partial J_p}{\partial \phi_4} \\[2mm] \dfrac{\partial J_p}{\partial \psi_4} \end{bmatrix} = \begin{bmatrix} [2R + (1-s')^2 \frac{1}{R}] & -2Ws' & -2\tau R & -2W \\ & P[2R + (1+s')^2 \frac{1}{R}] & 2W & -2PR \\ & & \tau[2R + (1-s')^2 \frac{1}{R}] & 2Ws' \\ & & & P(2R + (1+s')^2 \frac{1}{R}) \end{bmatrix} \begin{bmatrix} \phi_3 \\ \psi_3 \\ \phi_4 \\ \psi_4 \end{bmatrix}
$$

$$
- k_A^2 h_1 h_2 \ \text{diag} \ [1,P',1,P'] \begin{bmatrix} \phi_3 \\ \psi_3 \\ \phi_4 \\ \psi_4 \end{bmatrix} \qquad ; \qquad (8)
$$

in Fig. 1.d.:

$$
\begin{bmatrix} \dfrac{\partial J_p}{\partial \phi_1} \\[2mm] \dfrac{\partial J_p}{\partial \psi_1} \end{bmatrix} = \begin{bmatrix} 2\tau[(1 - s')^2 \frac{1}{R} + (1 - \Delta)^2 R] & -4W(s'-s) \\ -4W(s'-s) & 2P[(1 + s')^2 \frac{1}{R} + (1 + s)^2 R] \end{bmatrix} \begin{bmatrix} \phi_1 \\ \psi_1 \end{bmatrix}
$$

$$
- k_A^2 h_1 h_1 \ \text{diag} \ [1,P'] \begin{bmatrix} \phi_1 \\ \psi_1 \end{bmatrix} \qquad . \qquad (9)
$$

These relations are then used by a program to build systematically the matrices A and B by adding numerically the contribution of each element. The necessary inputs to the routine are:

- the total number of mesh elements;

- the local*mesh size h_1, h_2;

- the normalized propagation constant $\overline{\beta} = \beta/k_o$;

- the permittivity K_p at the location of the element S_p;

- the symmetry parameters s and s' that define the various modes.

---

* When a graded mesh is used, the dimensions h_1 and h_2 of each element S_p become a function of the position of the element.

Appendix C. Wave Equation Approach to Finite-Differences

1. Introduction

In Part II we presented a finite-difference (FD) method for computing the modes of dielectric guiding structures that is based on a variational expression for the longitudinal fields H_z and E_z. However, previously we had attempted to use a wave-equation approach: This consists in discretizing the differential equations that define the problem. We tested successfully the method in a simple one-dimensional case but found that it was totally inaccurate when applied to the rectangular dielectric guide.

We will briefly describe here the wave equation approach because it shows, in comparison, the advantages of the variational formulation that we used for our calculations.

2. Wave Equation Approach

As mentioned earlier, the fields propagating along a cylindrical guiding structure of axis z can be derived from the longitudinal fields

$$\phi = H_z \tag{1}$$

and

$$\psi = \frac{\omega \, \varepsilon_o}{\beta} \, E_z$$

The wave equations for these fields are (see Part II, Eqs. 38-39):
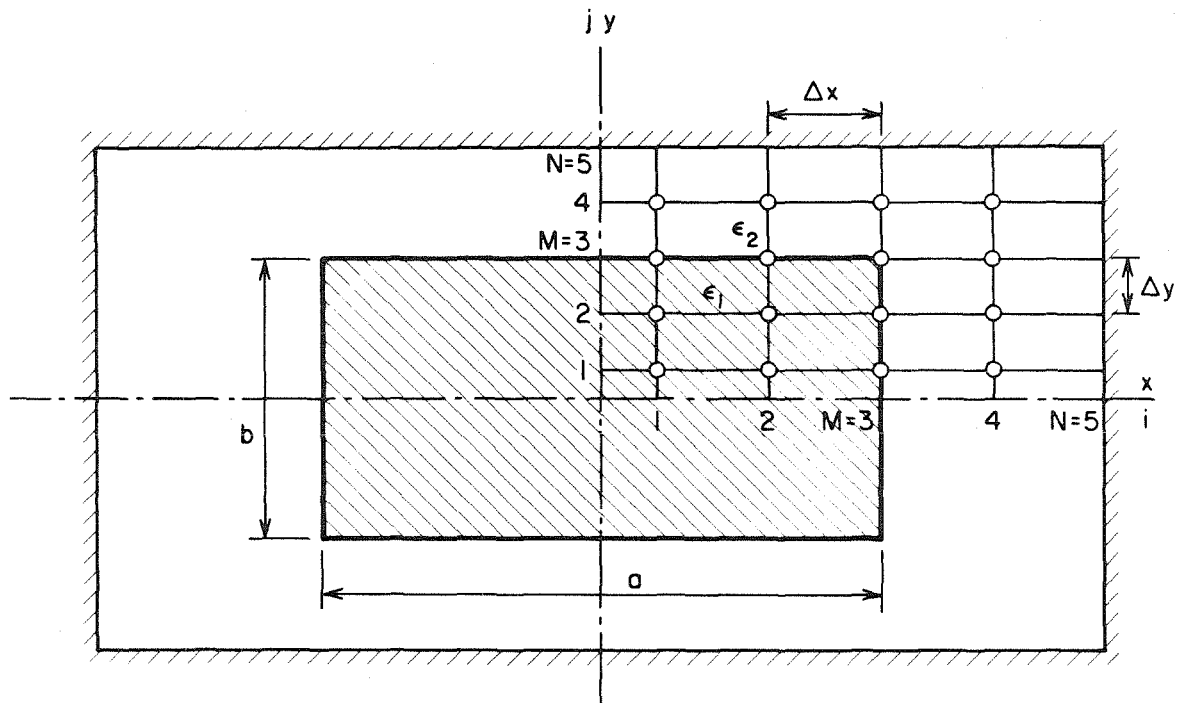
Figure 1. Mesh used for the wave-equation approach to FD. The
rectangular dielectric guide is enclosed in a "box" (electric wall
boundary conditions).

$$(\nabla_\tau^2 + h_p^2) \left\{ \begin{matrix} \phi \\ \psi \end{matrix} \right\} = 0 \tag{3}$$

in region p, where

$$k_p^2 = K_p k_o^2 - \beta^2 \quad . \tag{4}$$

The boundary conditions at the interface between two regions of dif-ferent dielectric permittivity, regions 1 and 2, can be written in the form [1,2]

$$-\frac{\partial \phi_2}{\partial x} + \frac{\partial \psi_2}{\partial y} = \tau \left(-\frac{\partial \phi_1}{\partial x} + \frac{\partial \psi_1}{\partial y} \right) \tag{5}$$

$$-\frac{\partial \phi_2}{\partial y} - \frac{\partial \psi_2}{\partial x} = \tau \left(-\frac{\partial \phi_1}{\partial y} - \frac{\partial \psi_1}{\partial x} \right) \tag{6}$$

where the parameter τ quantizes the difference in permittivity between the two regions:

$$\tau = \frac{k_2^2}{k_1^2} = \frac{K_2 k_o^2 - \beta^2}{K_1 k_o^2 - \beta^2} \quad . \tag{7}$$

If we consider the rectangular dielectric guide, we define a problem of finite extent by enclosing the waveguide in a "box" (electric walls) large enough so that it perturbs only minimally the modes of interest (Fig. 1). Because of symmetry we need to examine only one quadrant

which will be covered by a discrete mesh. At each mesh point, the wave equations are replaced by their FD-equivalents [2,3]. With the notation

$$\phi_{ij} = \phi(i\Delta x, j\Delta y)$$

we have approximately,

$$\left(\frac{\partial^2 \phi}{\partial x^2}\right)_{ij} = \frac{\phi_{i+1,j} - 2\phi_{ij} + \phi_{i-1,j}}{\Delta x^2} + 0(\Delta x^2) \qquad (8)$$

$$\left(\frac{\partial \phi}{\partial x}\right)_{ij} = \frac{\phi_{i+1,j} - \phi_{i-1,j}}{2\Delta x} + 0(\Delta x^2) \qquad (9)$$

with similar expressions for $\frac{\partial \phi}{\partial y}$ and $\frac{\partial^2 \phi}{\partial y^2}$. Substituting these expressions into the wave equation for region 2 (the outer medium of permittivity K_2) we obtain

$$\lambda \phi_{ij} = 2(1+R^2) \phi_{ij} - \phi_{i+1,j} - \phi_{i-1,j} - R^2 \phi_{i,j+1} - R^2 \phi_{i,j-1} \qquad (10)$$

where $\lambda = k_2^2 \Delta x^2$ and $R = \Delta x / \Delta y$; a similar expression can be written for ψ.

At interior points in the rectangular dielectric (region 1 of permittivity K_1), the corresponding equation for ϕ is

$$\lambda \phi_{ij} = 2\tau(1 + R^2) \, \phi_{ij} - \tau\phi_{i+1,j} - \tau\phi_{i-1,j}$$

$$- \tau R^2 \, \phi_{i,j+1} - \tau R^2\phi_{i,j-1} \qquad\qquad (11)$$

and a similar equation for ψ.

Eqs. 10 and 11 are valid at all points interior to regions 1 and 2, respectively. To treat the points located on the interface, we will introduce "image terms" [2,3] in the FD equations. Consider a point (i,j) located on the interface. We can write the limiting form of Eq. 11 when the interface is approached from the dielectric while the point (i,j) remains inside the dielectric (Fig. 2.b): The resulting equations contain terms involving $\phi^1_{i,j+1}$ and $\psi^1_{i,j+1}$. Similarly, when the interface is approached from the air, we obtain another limiting form of Eq. 10 containing $\phi^2_{i,j-1}$ and $\psi^2_{i,j-1}$. These "image terms" are then eliminated by using the interface conditions written in FD-form [2,3].

By proceeding as outlined above, we obtained a set of equations for each point (i,j) of the mesh. These equations are written in matrix form as

$$A \, X = \lambda \, X \qquad\qquad (12)$$

where X is an ordered vector of the field values ϕ_{ij} and ψ_{ij}. Equation 12 constitute a set of linear eigenvalue equations that are solved by standard numerical techniques. It is important to note that
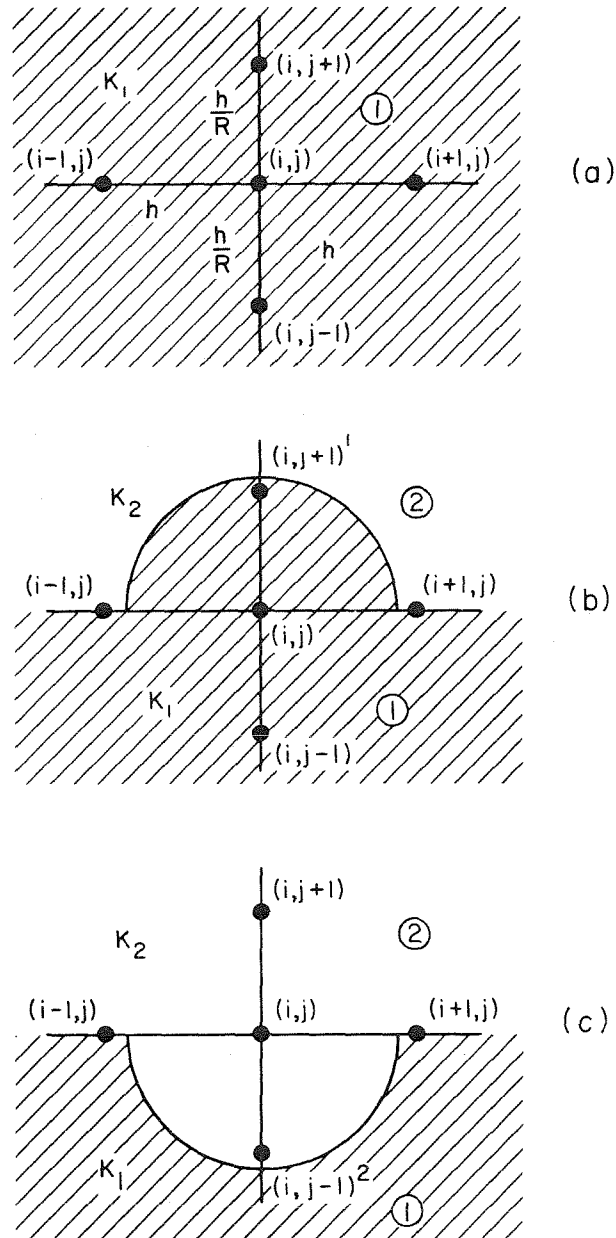
Figure 2. a) An interior point (i,j) and its four nearest neighbors in the mesh are represented in this graphical illustration of the five-point Laplace difference operator.

b) Image terms are obtained when the interface is approached from the dielectric and the point (i,j) is considered to be inside region 1.

c) The other set of image terms is obtained when the interface is approached from the outer medium and the point (i,j) is considered inside region 2.

in this case the matrix A presents a very unfavorable structure. It is nearly banded but for sparse off-band elements that introduce a coupling between the ϕ and ψ-fields at the interface points. The matrix A must be treated as a full matrix.

3. Numerical Results

We first applied this method on a semi-infinite slab because this problem has an analytical solution and permits us to test the treatment of the interface points and the influence of the outer "box". Figure 3 depicts the one-dimensional mesh used in this case and Figure 4 compares the field distribution computed by our numerical method and by the exact analytical solution. The agreement is excellent even for a very small number of points in the mexh (N=3).

We then tried to apply the method to the problem of a rectangular waveguide and by comparing it, in the large frequency region to Marcatili's or the round guide (see Part II), we found it very inaccurate for the maximum number of mesh points that we could practically use (N=9 in each linear direction). Because size of the matrix A increases with N^2, computer storage limitations prevent us from refining the mesh any further. In comparison the variational approach presents the advantage that the difference in permittivity between the region is taken globally into account instead of at a few discrete interface points. These results, as we have seen, in a banded matrix A can be handled numerically much more efficiently.
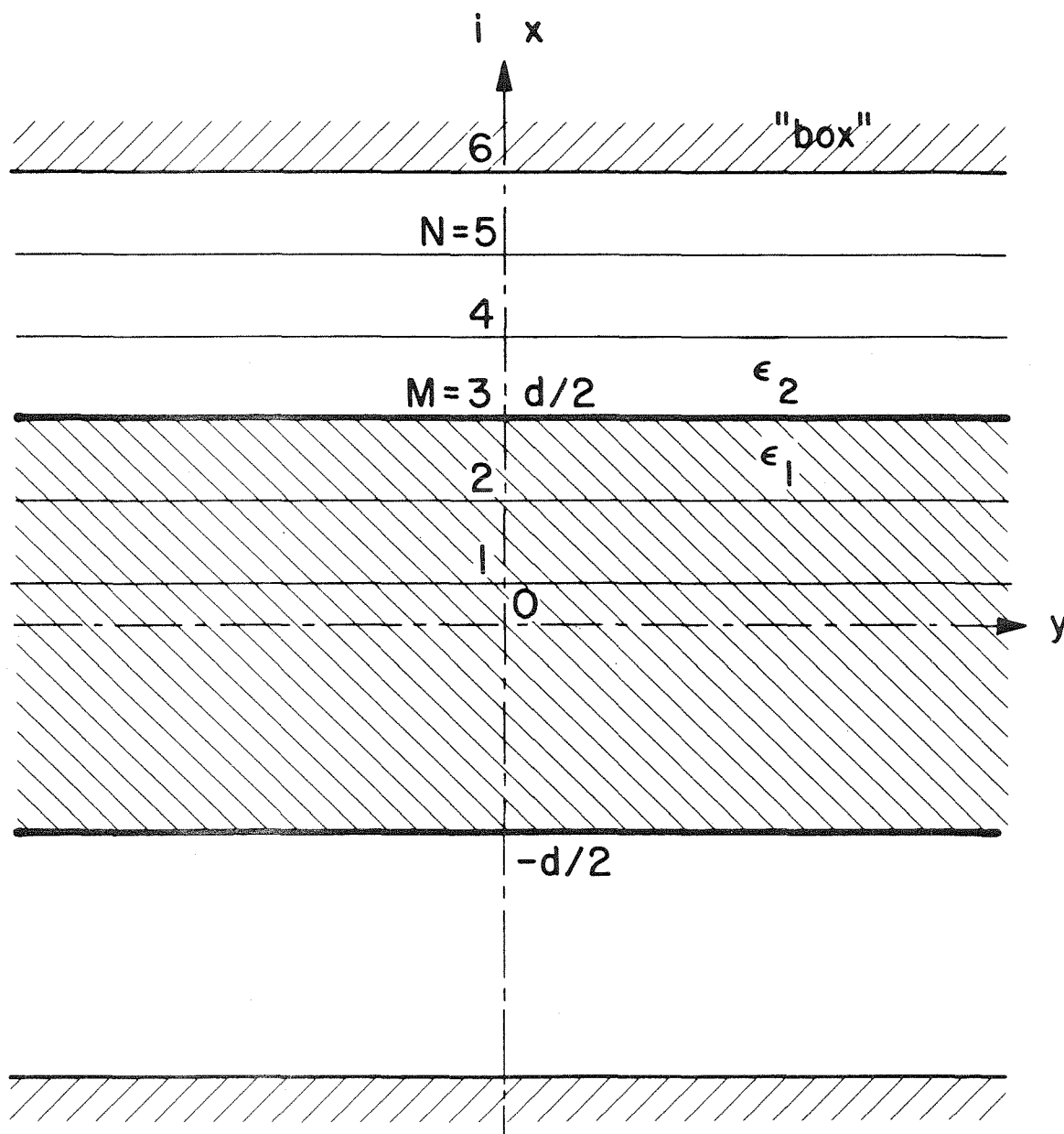
Figure 3.   One-dimensional mesh for the FD-solution of a semi-infinite
slab.
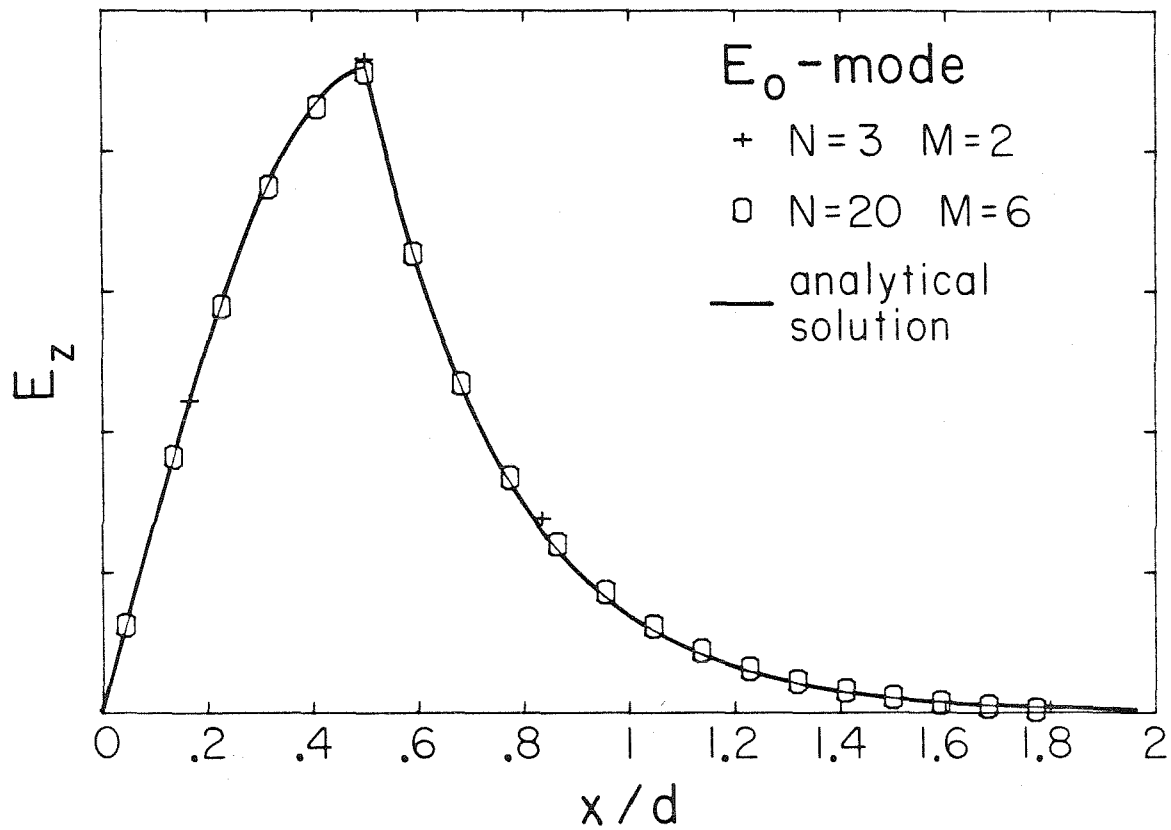
Figure 4. E_0-mode of a dielectric slab of high-permittivity: $K_1=13.1$ $K_2=1.0$. The normalized free-space wavenumber is: $k_o d=1.39$. The longitudinal electric field is plotted versus normalized distance (the location of the slab corresponds to: $-0.5 \leq \frac{x}{d} \leq 0.5$.

Moreover, the wave equation approach is limited simple geometries,

while the variational FD-method can test any geometry and permittivity

profile.

Appendix C Bibliography

1. R. Collins, <u>Field Theory of Guided Waves</u>', McGraw-Hill, New York,
    1960.

2. J.S. Hornsby and A. Gopinath, "Numerical Analysis of a Dielectric-
    Loaded Waveguide with a Microstrip Line - Finite-Difference
    Methods", IEEE Trans. Microwave Th. Tech., Vol. MTT-17, Sept.
    1969, pp. 684-690.

3. J.H. Collins and P. Daly, "Calculations for Guided Electromagnetic
    Waves using Finite-Difference Methods", J. Electronics Control,
    Vol.14, 1963, pp. 361-378.

4. H.-G. Unger, <u>Planar Optical Waveguides and Fibres</u> , Clarendon
    Press, Oxford, 1977.